

INFORMATION TO USERS

This manuscript has been reproduced from the microfilm master. UMI films the text directly from the original or copy submitted. Thus, some thesis and dissertation copies are in typewriter face, while others may be from any type of computer printer.

The quality of this reproduction is dependent upon the quality of the copy submitted. Broken or indistinct print, colored or poor quality illustrations and photographs, print bleedthrough, substandard margins, and improper alignment can adversely affect reproduction.

In the unlikely event that the author did not send UMI a complete manuscript and there are missing pages, these will be noted. Also, if unauthorized copyright material had to be removed, a note will indicate the deletion.

Oversize materials (e.g., maps, drawings, charts) are reproduced by sectioning the original, beginning at the upper left-hand corner and continuing from left to right in equal sections with small overlaps. Each original is also photographed in one exposure and is included in reduced form at the back of the book.

Photographs included in the original manuscript have been reproduced xerographically in this copy. Higher quality 6" x 9" black and white photographic prints are available for any photographs or illustrations appearing in this copy for an additional charge. Contact UMI directly to order.

UMI

A Bell & Howell Information Company
300 North Zeeb Road, Ann Arbor, MI 48106-1346 USA
313/761-4700 800/521-0600

FIRST PRINCIPLES LINEAR RESPONSE
CALCULATIONS OF LATTICE DYNAMICS

A Dissertation

Presented to The Faculty of the Department of Physics
The College of William and Mary

In Partial Fulfillment
Of the Requirements for the Degree of
Doctor of Philosophy

By
Cheng-Zhang Wang

June 1995

UMI Number: 9606705

UMI Microform 9606705
Copyright 1995, by UMI Company. All rights reserved.

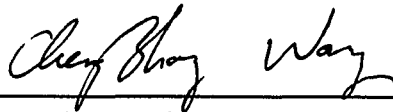
This microform edition is protected against unauthorized
copying under Title 17, United States Code.

UMI
300 North Zeeb Road
Ann Arbor, MI 48103

APPROVAL SHEET

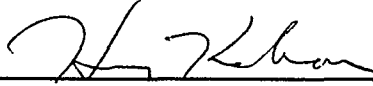
This dissertation is submitted in partial fulfillment
of the requirements for the degree of

Doctor of Philosophy.

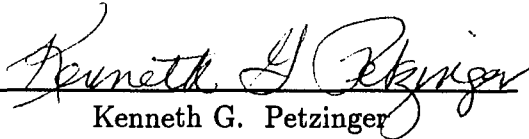


Cheng-Zhang Wang

Approved, June 1995



Henry Krakauer



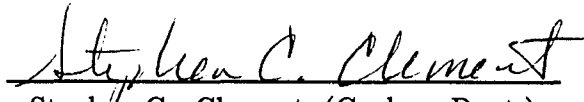
Kenneth G. Petzinger



Harlan E. Schone



Dennis M. Manos



Stephen C. Clement (Geology Dept.)

Contents

Acknowledgments	v
List of Tables	vi
List of Figures	viii
Abstract	viii
Chapter 1 Introduction	2
1.1 Background	2
1.2 Local Density Approximation	10
Chapter 2 Methodology	16
2.1 Linearized Augmented Plane Wave (LAPW) Method	16
2.1.1 Basis Functions	17
2.1.2 Potential	19
2.1.3 Charge Density	21
2.1.4 Total Energy	23
2.1.5 Pseudopotential	24
2.1.6 Force	28
2.2 Linear Response Theory in the LAPW Method	31
2.2.1 First-order Forces and Dynamical Matrix	34
2.2.2 Dielectric Tensor and Born Effective Charge Tensor	36
2.2.3 LO Phonons at Zone Center and Phonon Dispersions in BZ	38
Chapter 3 Lattice Dynamics of CuCl	40
3.1 Introduction	40
3.2 Computational Details	45

3.3	Frozen Phonon Calculations at Γ -point	47
3.4	Phonons at Γ -point, Z^* and ϵ_∞	49
3.5	Phonon Dispersions	53
Chapter 4 Lattice Dynamics of SiC Under Pressure		58
4.1	Introduction	58
4.2	Calculational Details	60
4.3	Ground State Properties	63
4.4	Z^* , ϵ_∞ , Phonon Dispersions and Elastic Constants	70
4.5	Properties Under Pressure	77
4.6	Summary	86
Chapter 5 Lattice Dynamics of KNbO₃		88
5.1	Introduction	88
5.2	Methods	92
5.3	Ground State Structure	94
5.4	Z^* and ϵ_∞ for Both Cubic and Rhombohedral Structures	102
5.5	Phonon Modes at Γ -point of Cubic Structure	109
5.6	Phonon Modes at Γ -point of Rhombohedral Structure	112
5.7	Summary	116
Chapter 6 Conclusion		118
Bibliography		120
Vita		135

Acknowledgments

I would like to express my deep appreciation to my advisor Professor Henry Krakauer for his precious guidance, constant support and encouragement throughout my graduate studies at the College of William and Mary.

I feel grateful to my committee members, Profs. K. Petzinger, H. Schone, D. Manos, and S. Clement, for carefully reading my manuscript and for their valuable comments.

Special thanks are directed to Dr. Rici Yu, whose excellent skills in the density functional calculations benefited me greatly. I highly appreciate his friendship and collaboration in these years.

I am very thankful to Chree Haas and Matt Coffey for their indispensable help on computer facilities and stimulating discussions in the research. I appreciate Paula, Dianne and Sylvia for helping me with administrative matters. I would also like to thank my friends for their friendship and companionship. They are Drs. Y. Kuang, X. Tang, X. Ou, T. Tse, A. Ananda, S. Zhang, Z. Li, Y. Wang, X. Liang and H. Yao.

Most importantly, I thank my parents and my wife for their support and love, without which I would not be able to achieve anything. I am pleased to dedicate this PhD thesis to them.

List of Tables

3.1	Results from frozen-phonon calculations at Γ -point in CuCl.	48
3.2	Phonon frequencies from frozen-phonon and linear response calculations at Γ -point in CuCl.	49
3.3	Calculated Born effective charges and dielectric constant of CuCl. . .	50
3.4	Calculated and experimental phonon frequencies for CuCl.	56
4.1	Test frozen-phonon calculations for the frequencies of TO(Γ) mode of 3C-SiC.	62
4.2	Equilibrium state properties of 3C-SiC.	66
4.3	Transitional parameters from zincblende structure to rocksalt structure for SiC.	69
4.4	Calculated Born effective charges Z^* and ϵ_∞ at the equilibrium state of 3C-SiC.	71
4.5	Theoretical and experimental phonon frequencies in 3C-SiC.	72
4.6	Elastic constants of 3C-SiC.	75
4.7	Grüneisen's parameters of phonon modes in 3C-SiC.	78
4.8	The calculated Z^* , ϵ_∞ , and LO-TO splitting in 3C-SiC under pressure.	79
4.9	Fitted equations of ω_{TO} and ω_{LO} for SiC under pressure.	81
4.10	Volume dependence of dielectric constant of Si and diamond C.	83
5.1	Correspondence of uniform k -point meshes to the number of special k -points in irreducible Brillouin zone (IBZ).	93
5.2	Total energy and forces for various configurations of KNbO ₃ in determining its ground state structure using (4 4 4) k -point mesh.	96
5.3	Total energy and forces for various configurations of KNbO ₃ in determining its ground state structure using (6 6 6) k -point mesh.	97

5.4	Total energy and forces for various configurations of KNbO_3 in determining its ground state structure using (8 8 8) k-point mesh.	98
5.5	Ground state structures determined by calculations and experiment for KNbO_3	99
5.6	Comparison of eigenvalues of Born effective charge tensors for KNbO_3	105
5.7	Comparison of calculated Γ -point phonon frequencies in cubic KNbO_3 with experiment.	110
5.8	Eigenvectors of calculated $\text{TO}(\Gamma)$ phonon modes in cubic KNbO_3	111
5.9	Rhombohedral KNbO_3 zone center phonon frequencies for optical modes.	113
5.10	Rhombohedral KNbO_3 zone center longitudinal optical phonon frequencies.	114
5.11	Eigenvectors of calculated transverse phonon modes at Γ -point in rhombohedral structure of KNbO_3	115

List of Figures

3.1	Raman spectrum of CuCl at 2 K.	44
3.2	Phonon dispersion curves of CuCl.	57
4.1	Calculated energy dependence on the volume for zincblende and rock-salt phases.	67
4.2	Gibbs free energy under pressure for zincblende and rocksalt phases. .	68
4.3	Phonon dispersion curves of 3C-SiC.	76
4.4	The volume dependence of Born effective charge calculated for 3C-SiC.	84
4.5	Calculated dielectric constant $\epsilon_{\infty}(V)$ for SiC	85
5.1	Structure of cubic perovskite compounds ABO_3	89

Abstract

First principles calculations, using the density-functional theory and particularly the local density approximation (LDA), have achieved remarkable success in studying the properties of solid state systems. Although the basic results of these calculations are the electronic structures (eigenvalues, eigenfunctions, etc.) and the total energy of ground state, many other related physical properties can be deduced from them by investigating their response under external perturbations. Using the linear response method with linearized-augmented-plane-wave (LAPW) basis, we have calculated lattice dynamical properties of important semiconductors CuCl, SiC and ferroelectric KNbO₃. CuCl is known to exhibit large anharmonic effects and possibly a complicated multi-well Born Oppenheimer surface reminiscent of the instabilities in perovskite ferroelectrics and the high-temperature cuprate superconductors. However, we have determined its phonon dispersion from first-principles calculations and find it to be in good agreement with the low temperature experimental results. For zincblende SiC, the calculated phonon dispersions, Grüneisen's parameters, dielectric constant, Born effective charge, elastic constants, and the equation of state agree very well with the available experimental data. Additionally, we find that its dielectric constant decreases with pressure and Born effective charge increases with pressure up to 80 GPa without any saturation, calling into question the recent interpretation of experimental results to the contrary. Our calculations for KNbO₃ find unusually large Born effective charges on Nb and O that originate from the strong covalent interactions between Nb 4d and O 2p orbitals. The Born effective charges and dielectric tensors are found to change up to 20% from the cubic structure to the rhombohedral structure, demonstrating that the polarizability of the perovskite ferroelectrics is very sensitive to the small atomic displacements involved in the transitions. The phonon modes for the cubic and rhombohedral structures are also calculated and their implications are discussed.

FIRST PRINCIPLES LINEAR RESPONSE
CALCULATIONS OF LATTICE DYNAMICS

Chapter 1

Introduction

1.1 Background

Density functional theory within the local density approximation (LDA) has been remarkably successful in investigating molecules, surfaces and solid state systems [1-3]. It has become a powerful theoretical tool for studying structural and vibrational properties of real materials, determining the lattice constants, bulk modulus, cohesive energy, elastic constants, phonon frequency, equilibrium atomic configurations, etc. The basic idea of density functional theory is that [4,5], the ground state total energy of a system of interacting electrons in an external potential is a minimum with respect to variations in the electron density $\rho(\mathbf{r})$. Expressing $\rho(\mathbf{r})$ in terms of wavefunctions of *fictitious non-interacting electrons* $\psi_i(\mathbf{r})$ and minimizing the total energy of a system with respect to them, we get the Kohn-Sham equations [5] (atomic units are assumed

in the whole dissertation unless otherwise stated):

$$\left(-\nabla^2 + V_{eff}[\rho] - \varepsilon_i\right)\psi_i(\mathbf{r}) = 0, \quad (1.1)$$

where the charge density is given by

$$\rho(\mathbf{r}) = \sum_i |\psi_i(\mathbf{r})|^2, \quad (1.2)$$

and where i goes over the occupied states. The effective potential consists of three contributions, an external potential term, a hartree term and an exchange-correlation term for which we use local density approximation [5] ,

$$V_{eff}(\mathbf{r}) = V_{ext}(\mathbf{r}) + \int d\mathbf{r}' \frac{\rho(\mathbf{r}')}{|\mathbf{r} - \mathbf{r}'|} + \mu_{xc}(\mathbf{r}). \quad (1.3)$$

Eq. (1.1) and Eq. (1.2) must be solved self-consistently. The variational method is usually used to solve Eq. (1.1). The variational trial function $\psi_i(\mathbf{r})$ is expanded with a basis set,

$$\psi_i(\mathbf{r}) = \sum_j C_{ij} \phi_j(\mathbf{r}) \quad (1.4)$$

where $\phi_j(\mathbf{r})$ are the basis functions and C_{ij} are the expansion coefficients, which are the only variables in the problem when the basis functions are chosen. Since the total energy in density functional theory is variational, the problem of solving the self-consistent Eq. (1.1) and Eq. (1.2) amounts to determining the expansion coefficients C_{ij} for the occupied states that minimize the total energy, which is accomplished by solving the matrix eigenvalue equations. With no free parameters that are fit to experimental data, such calculations are often referred to as first principles or *ab initio* calculations. Although the basic results obtained from this kind of calculation

are the electronic structures (eigenvalues, eigenfunctions, etc.) and the total energy of the ground state, many other related properties can be deduced from them by investigating their response under external perturbations. For example, within the Born-Oppenheimer approximation, we can determine the lattice dynamical properties of a system by superimposing a frozen-in phonon distortion on the periodic crystal and studying the electronic response. Basically, there are two methods currently in use to deal with external perturbations in periodic systems.

The first one, called the supercell or direct method [6], is computationally straightforward, and uses a larger cell to simulate the phonon-like perturbation. This method requires the perturbation wavevector to be commensurate with the reciprocal basis vectors of the crystal. Because the perturbed system is treated on the same footing as the unperturbed one, no modification is needed in the algorithm and hence the computer code. The response to the external perturbation is obtained by comparing the properties of the two systems. The advantage of this method is that both linear and nonlinear effects can be studied; the linear effects, which are not directly accessible, are usually extracted by some interpolation scheme. However, the use of a supercell increases the computational burden significantly. Using the conventional diagonalization techniques, the computational complexity scales as N_{basis}^3 , where N_{basis} is the number of basis functions in the variational wave-function expansion in the supercell. This unfavorable scaling restricts this method to the calculations of those perturbations of highest symmetry and wavevectors that are not too small. An interpolation method based on calculated interplanar force constants can be used to obtain the phonon dispersions. By displacing entire planes of atoms the interplanar

force constants and hence the dispersion relations for the corresponding directions in the phonon Brillouin zone (BZ) can be obtained [7]. Because the planar force constants are linear combinations of the elements of the force constant matrix, the latter ones may be obtained from a limited set of planar force constants. Wei and Chou [8,9] have fitted real space force constants to calculated interplanar results for Si and Ge using the supercell method, and have mapped out the phonon dispersions throughout the Brillouin zone with the real space force constants. Recently, Frank *et al.* [10] calculated the phonon dispersions of alkali metals (Li, Na, K) with the same idea. The number of nearest-neighbor force constants that can be determined is directly dependent on the size of the supercell, and the approach is useful for systems with force constants that decay rapidly with the distance. Long-wavelength perturbations such as longitudinal phonons and macroscopic electric fields have been treated in simple semiconductors [6, 11, 12] using large supercells with the direct method. A macroscopic electric field cannot be directly taken into account in traditional calculations because the Born-von Karman periodic boundary conditions forbid non-zero macroscopic fields. The effect of macroscopic electric field can only be determined by extrapolating from investigations in the limit of long wavelengths or small q . McKittrick [12] calculated the macroscopic dielectric tensor, Born effective charges and piezoelectric constant for GaAs at several finite wavevectors for GaAs and extrapolated the results to zero wavevector. However, the use of large supercells puts severe limitations on the applicability of this method to complex systems.

The second method is based on linear response theory, which describes the effects that are linearly dependent on the external perturbations. The fact that

only linear effects are accessible in this method is not inconvenient in many cases, such as lattice dynamics, where experimentally measured quantities can be exactly expressed in terms of linear response functions. There are two main schemes in practical calculations in this category. One is the dielectric matrix (DM) approach [13]. It calculates the dielectric screening in which atomic displacements are treated as perturbations. For the first-order perturbation, the computational effort is independent of the wavevector \mathbf{q} of the perturbations, unlike the supercell method. The real limitations for this approach are three-fold. First, the charge density and the potential are usually presented using a plane wave basis. Other representations greatly complicate the formalism. Planewaves, however, are inefficient for treating systems with localized orbitals. Even for the simplest semiconductors, several hundreds of plane waves are needed to get well converged results [14]. Secondly, it is rather difficult to take into account the effects of nonlocal pseudopotentials in this approach. But in modern planewave calculations, nonlocal pseudopotentials must be included to ensure accurate results. Thirdly, there are two time-consuming steps in this approach that makes it computationally unfavorable: the inversion of DM and the cumbersome summations over conduction bands at \vec{k} points in Brillouin zone.

Another scheme based on the Sternheimer linear response theory for atomic polarizabilities [15,16] was introduced by Baroni *et al.* [17] to solid state calculations. This method has some of the advantages of the dielectric-matrix and the supercell approaches yet avoids many of their drawbacks. The main features are as follows. The variational total energy can be expanded in terms of perturbation strength λ ,

$$E_{total} = E^{(0)}[\rho^{(0)}] + \lambda E^{(1)}[\rho^{(0)}] + \lambda^2 E^{(2)}[\rho^{(1)}] + \dots \quad (1.5)$$

Note that the second order change of total energy (or first order of force) is determined by the first order change of charge density and orbitals. The “2n+1” theorem of the perturbation theory [18] indicates that even the third-order total energy can be determined from the first order quantities. Minimizing the total energy with respect to the first order change of charge density yields a pair of equations analogous to Eq. (1.1) and Eq. (1.2) that should also be solved self-consistently:

$$(H^{(0)} - \epsilon_i^{(0)})\psi_i^{(1)} = -(V_{eff}^{(1)}[\rho^{(1)}])\psi_i^{(0)}, \quad (1.6)$$

$$\rho^{(1)} = \sum_i^N \psi_i^{(0)*} \psi_i^{(1)}, \quad (1.7)$$

where $H^{(0)}$ denotes the Hamiltonian in Eq. (1.1), and $\psi_i^{(0)}$ is an unperturbed wavefunction obtained in Eq. (1.1), and $\psi_i^{(1)}$ is the first order change in the wavefunction. The self-consistent response to the external perturbations is obtained by iteration, which is how the charge density and potential are calculated in the direct method. This also permits the straightforward inclusion of nonlocal potentials and use of basis functions other than planewaves. Furthermore, the linear matrix differential equation for the linear order wavefunction $\psi_i^{(1)}(\mathbf{r})$ is solved directly; no explicit conduction bands summation for the charge density is involved. Only the projection operator onto the conduction manifold is required, and this is easily constructed from a knowledge of only valence states. The computational complexity for the solution of the linear matrix equations is comparable to that for the eigenvalue equations of the perfect crystal $\sim N_{basis}^3$. As in the DM approach, the calculations can be performed for perturbations of any wavevectors and the computational effort is independent of wavevector \mathbf{q} , with only valence energy bands and wave functions of the unperturbed

crystal needed. Another advantage of the Sternheimer method linear response theory is that the long wavelength limit can be taken easily and the macroscopic electric field is treated [17, 19–21] as efficiently as other perturbations.

The success of Sternheimer method linear response theory is witnessed by an increasing number of such calculations and the renewed interest in lattice dynamics in recent years. The theory has been applied to semiconductors, metals, oxides, ferroelectrics, surfaces, alloys, superlattices, etc. Now, such calculations are feasible for solids up to ten atoms in the unit cell. Most of these calculations use pseudopotentials coupled with plane waves basis set, [17, 19, 20, 22–35] which simplifies the formalism and implementation. Unfortunately, plane wave basis is not efficient for the materials containing transition metal atoms and first row atoms such as oxygen, since very many plane wave basis functions have to be used for these atoms' localized valence states. In contrast, the linear muffin-tin orbital (LMTO) [36] and linearized augmented plane wave (LAPW) [36–38] basis sets do not have this problem, and both have been implemented for the linear response calculations [21, 39–48].

Physically, it is important to calculate phonon modes and interatomic force constants from first principles methods because such calculations aid us in understanding a wide range of interesting and fundamental phenomena. For instance, despite a great deal of experimental and theoretical effort to understand the origin of the high-temperature superconductivity in the layered cuprates, no consensus has ever been reached as to the underlying mechanism that is responsible for this surprising phenomenon. [49] Nine years have passed since the discovery of high T_c superconductors in 1986 [50], with the true understanding of its origin seemingly

even more elusive. However, it would be fruitful and persuasive to carry out the first principles calculations for the electron-phonon coupling, which is responsible for superconductivity in almost all previously known superconductors, and definitively assess if the electron-phonon coupling strength is large enough to support such high transition temperature (see Ref. [51] and references therein). For another instance, the first principles calculations of surface force constants can reveal their characteristics, providing insight for the understanding of many distinctive properties such as reconstructions of atoms at surface.

The first principles linear response calculations can be used to determine phonon dispersions in the entire Brillouin zone accurately, from which other properties may be obtained, such as heat capacities, thermal expansion coefficients, and temperature dependence of the band gap, etc. The calculated phonon frequencies typically agree with experiment within a few percent. It is worth noting that the eigenvectors of phonon modes can also be calculated with the same reliability. Recently, Kulda *et al.* [52] conducted a complete inelastic neutron scattering study on phonon eigenvectors and frequencies of Si, both of which are in good agreement with the predictions of *ab initio* calculations. On the other hand, the well established phenomenological models for lattice dynamics have limited predictive power, since different models may give very different predictions for the amplitudes of the atomic displacements, though the calculated eigenfrequencies agree equally with experiments. [53]. However, the parameters entering these models are fitted to experiments. In recent years, there have been efforts to combine reliable first principles calculations with efficient interpolation scheme provided by the empirical models. [54]

In this dissertation, the lattice dynamics are investigated with first principles linear response calculations using LAPW basis. In Chapter 2, the theoretical formalism and main points are provided. Chapter 3, 4, and 5 are focused on the applications to semiconductors CuCl, SiC, and ferroelectrics KNbO₃, respectively. Chapter 6 concludes the whole thesis.

1.2 Local Density Approximation

During the past three decades, density functional formalism has evolved as a conceptually and practically useful method for studying the ground state properties of many-electron system. It is based on two theorems [4, 5]: the complete many-body ground state wavefunction Ψ of an electronic system is a unique functional $\Psi[\rho(\mathbf{r})]$ of the electronic charge density $\rho(\mathbf{r})$; the total energy functional of the electronic system under the external potential is stationary with respect to variation in the charge density and assumes its minimum value at the true charge density. The total energy of the system can be written as

$$E[\rho] = T[\rho] + U[\rho] + \int V_{ext}(\mathbf{r})\rho(\mathbf{r})d\mathbf{r} + E_{xc}[\rho], \quad (1.8)$$

where $T[\rho]$ is the kinetic energy of the *non-interacting* electrons of density $\rho(\mathbf{r})$; $U[\rho]$ arises from the electron-electron Coulomb interaction or Hartree energy; V_{ext} is the external potential, which includes the electron-nuclei interaction; and $E_{xc}[\rho]$ is the exchange-correlation energy, which is a universal functional and contains all of the many-body interactions not incorporated by the other terms. However the exact functional form of $E_{xc}[\rho]$ is unknown.

For an electron gas of uniform charge density, the exchange-correlation energy of the ground state is

$$E_{xc} = \int \rho_0 \epsilon_{xc}(\rho_0) d\mathbf{r}, \quad (1.9)$$

where $\epsilon_{xc}(\rho_0)$ is the ground state energy for one electron from exchange and correlation in an electron gas of uniform density ρ_0 . For the inhomogeneous electron gas, Kohn and Sham [5] suggested that the above exchange-correlation energy be analogously represented by

$$E_{xc} = \int \rho(\mathbf{r}) \epsilon_{xc}(\rho(\mathbf{r})) d\mathbf{r}, \quad (1.10)$$

replacing the electron density constant ρ_0 with the actual electron density $\rho(\mathbf{r})$. This assumption is the well-known local density approximation (LDA) that has been used most widely in the density functional calculations. This approximation should be good for the systems with sufficiently slowly and weakly varying charge densities in space. However, in practice, it appears to be better than expected, reproducing many measurable quantities satisfactorily even in atoms, solids, and at surfaces where the charge densities vary rapidly. These quantities include the ground-state geometries, vibration and phonon frequencies, moments of the density, etc.

The concept of exchange-correlation hole sheds light on understanding the success of LDA. The central question is how well the LDA represents the exchange-correlation hole, i.e. the depletion of electron charge in the vicinity of a particular electron due to the Coulomb repulsion and the Pauli exclusion principle. Gunnarsson and Lundqvist [55] showed that the exchange-correlation energy, which is interpreted as interaction between an electron and its corresponding hole, is influenced by only

the spherical average of the hole, rather insensitive to the details of the hole shape. The fact that LDA involves a spherical hole does not incur any drawbacks. Additionally, LDA satisfies the sum rule, a requirement that the total charge of the hole be precisely $|e|$, resulting in a systematic cancellation of errors. Finally, the LDA hole is localized, and its size varies with the density in a physical way. These three features are responsible for the fruitful applications of LDA to systems with charge densities that vary rapidly and strongly where LDA has little formal justification.

There are quite a few prescriptions for $\epsilon_{xc}(\rho)$ in Equation (10) in the literature. For example, the Wigner interpolation formula [56] has the functional form:

$$\epsilon_{xc}(\rho) = \rho^{\frac{1}{3}} \left(-0.984745 - \frac{0.949 + 8.905\rho^{\frac{1}{3}}}{(1 + 12.557\rho^{\frac{1}{3}})^2} \right). \quad (1.11)$$

It aims to reproduce properly the high-density limit of electron gas data and the low-density Wigner crystal energy. Other widely used forms are proposed by: (a) Ceperley and Alder [57, 58], parametrized by Perdew and Zunger [59]; (b) Hedin and Lundqvist [60], generalized by von Barth and Hedin [61] for spin-polarized systems; (c) Vosko *et al.* [62, 63]; (d) Kohn *et al.* [5, 64], so-called X_α exchange-correlation potential, and so on .

Despite the apparent success in LDA calculations, one should bear in mind that density functional theory has been approximated. The exchange-correlation energy term should be a functional of charge density, instead of a functional of local charge density. Although we do not know its exact form, the exchange-correlation potential is undoubtedly nonlocal and extremely complicated. The use of a local function for exchange-correlation potential greatly simplifies the implementation of density functional theory and makes it tractable computationally. However, this

approximation is probably responsible for deficiencies in some cases. In fact there are still many open problems associated with LDA.

It is well known that LDA calculations fail in understanding the magnetic properties and in predicting the insulating behavior for the nonmetallic, undoped parent insulators of cuprate high transitional temperature superconductors [65]; LDA usually overestimates the dielectric constant for semiconductors and insulators by 10 ~ 30% and predicts a relatively smaller lattice constant compared to experiments, typically by 1-2%. However, it is not necessarily a failure of LDA to give too small band gaps for semiconductors and insulators compared directly with the photo-emission experiments. [1] The density functional theory is designed to describe the ground state properties. The difference of eigenvalues of the Kohn-Sham equation between the lowest unoccupied state and the highest occupied state cannot be interpreted as the minimum excitation energy observed in experiment. With strong motivation to understand its success and failure, people have been trying to refine and extend LDA ever since its introduction.

It is straightforward to extend the above treatment to spin-polarized systems. The density functional formalism shows that, at least in principle, one can determine the total energy using a functional that depends on the density alone and not the spin densities. However, expressing the functional of total energy in terms of spin densities is convenient,

$$E = E[\rho_{\uparrow}, \rho_{\downarrow}]. \quad (1.12)$$

The exchange-correlation energy is described by local spin-density approximation

(LSDA),

$$E_{xc}^{LSDA} = \int \rho(\mathbf{r}) \epsilon_{xc}[\rho_{\uparrow}(\mathbf{r}), \rho_{\downarrow}(\mathbf{r})] d\mathbf{r}. \quad (1.13)$$

where $\epsilon_{xc}[\rho_{\uparrow}(\mathbf{r}), \rho_{\downarrow}(\mathbf{r})]$ is the exchange-correlation energy for one particle in a homogeneous, spin-polarized electron gas with spin-up and spin-down densities $\rho_{\uparrow}(\mathbf{r})$ and $\rho_{\downarrow}(\mathbf{r})$, respectively; and where $\rho(\mathbf{r}) = \rho_{\uparrow}(\mathbf{r}) + \rho_{\downarrow}(\mathbf{r})$. One has to write the analogous Kohn-Sham equations for each spin component of the electrons. Lundqvist and March [66] presented a good discussion about these coupled equations, which contain spin-dependent exchange-correlation potentials. LSDA provides flexibility to build in more of the actual physics into the approximate functionals. [55] It can describe the bond breaking in molecules and simplify the description of open electron shells of atoms, thereby providing a basis for Hund's rules [67].

A natural attempt to improve LDA is the generalized gradient approximation (GGA). The basic idea of GGA is that incorporating the local gradient of density in exchange-correlation energy might improve the LDA. The $\epsilon_{xc}(\rho(\mathbf{r}))$ in Equation (9) is replaced by $\epsilon_{xc}(\rho(\mathbf{r}), |\nabla\rho(\mathbf{r})|)$. GGA obtains the correct magnetic ground state of Fe solid; also ground state properties of light atoms, molecules, and solids composed of them are improved substantially (see Ref. [2,68] and references therein). However the improvements should be taken with a grain of salt. For instance, the lattice constants are overestimated for some materials containing heavy elements; the agreement with experiment is even worse than the LDA.

Another attempt to improve LDA is the weighted density approximation (WDA) (see Ref. [69] and references therein) which includes the nonlocal effects through Coulomb integral of the density with model exchange-correlation holes. It restores

such desirable features of exchange-correlation potential as an asymptotical r^{-1} behavior far away from atoms and a z^{-1} behavior of the potential outside solid surface [69]. But there exist few WDA reports for solids because it increases the computational labor considerably compared with LDA or GGA. Other attempts going beyond LDA include self-interaction corrected approximations (see Ref. [70,71] and references therein) and those developed from wave-vector analysis of the exchange-correlation energy (see Ref [72,73] and references therein), etc.

Chapter 2

Methodology

2.1 Linearized Augmented Plane Wave (LAPW) Method

The linearized augmented planewave (LAPW) method, which evolved from the augmented plane wave (APW) method of Slater [74, 75], has proven to be a highly accurate tool for electronic structure calculations for real materials. The main feature of LAPW method is the use of dual representations for two physically different areas. Near the nucleus the basis functions are numerical solutions to the radial Schrödinger equation and its energy derivative. In the interstitial area between the atoms, where the wavefunctions and potentials are much smoother, the basis functions are represented by plane waves. In this important region where chemical bonds form, plane waves provide an unbiased representations of the wavefunctions. In contrast to the conventional plane wave method, the LAPW basis has no difficulty in treating

materials containing localized orbitals, like transition metals with d electrons and rare earth elements with f electrons. In the full potential LAPW calculations, no shape approximations are made for the potential or charge density, and relativistic effects are easily included. The basis functions, potential, charge density, and total energy in LAPW method have been excellently reviewed by Wei [76], Lu [77], and Singh [2]. The pseudopotential and force formalism in LAPW method were reviewed by Yu, Singh and Krakauer [78]. Here only the main points in each part are mentioned, referring the details to the above reviews. When necessary, the background for a specific topic is introduced briefly.

2.1.1 Basis Functions

The variational Bloch wavefunction of the independent particle is expanded as

$$\psi_{n,\mathbf{k}}(\mathbf{r}) = \sum_{\mathbf{G}} C_{n\mathbf{k}}(\mathbf{G}) \phi_{\mathbf{k}+\mathbf{G}}(\mathbf{r}), \quad (2.1)$$

where n is the energy band index, \mathbf{k} is the wavevector in Brillouin zone, \mathbf{G} refers to a reciprocal lattice vector, $C_{n\mathbf{k}}(\mathbf{G})$ is the expansion coefficient, and $\phi_{\mathbf{k}+\mathbf{G}}$ is a LAPW basis function.

The LDA total energy, Eq. (1.8), is minimized with respect to the expansion coefficients $C_{\mathbf{G}}^n(\mathbf{k})$ by solutions of secular equations:

$$\sum_{\mathbf{G}'} \left[H_{\mathbf{G}\mathbf{G}'}(\mathbf{k}) - \varepsilon_n(\mathbf{k}) O_{\mathbf{G}\mathbf{G}'}(\mathbf{k}) \right] C_{\mathbf{G}'}^n(\mathbf{k}) = 0, \quad (2.2)$$

where $H_{\mathbf{G}\mathbf{G}'}(\mathbf{k})$ and $O_{\mathbf{G}\mathbf{G}'}(\mathbf{k})$ are the Hamiltonian and overlap matrix elements, respectively,

$$H_{\mathbf{G}\mathbf{G}'}(\mathbf{k}) = \left\langle \phi_{\mathbf{k}+\mathbf{G}}(\mathbf{r}) \left| H \right| \phi_{\mathbf{k}+\mathbf{G}'}(\mathbf{r}) \right\rangle, \quad (2.3)$$

$$O_{\mathbf{G}\mathbf{G}'}(\mathbf{k}) = \left\langle \phi_{\mathbf{k}+\mathbf{G}}(\mathbf{r}) \middle| \phi_{\mathbf{k}+\mathbf{G}'}(\mathbf{r}) \right\rangle, \quad (2.4)$$

where $H = -\nabla^2 + V_{eff}(\mathbf{r})$.

In the LAPW method, all space is divided into two regions: muffin-tin spheres which are centered at each nucleus position and the interstitial regions. The LAPW basis function is accordingly constructed as

$$\phi_{\mathbf{k}+\mathbf{G}}(\mathbf{r}) = \begin{cases} \frac{1}{\sqrt{\Omega}} e^{i(\mathbf{k}+\mathbf{G})\cdot\mathbf{r}}, & \mathbf{r} \in \text{Interstitial} \\ \sum_{l,m} \left[a_{lm}^i(\mathbf{k} + \mathbf{G}) u_l(E_l^i, r_i) + b_{lm}^i(\mathbf{k} + \mathbf{G}) \dot{u}_l(E_l^i, r_i) \right] Y_{lm}(\hat{r}_i), & r_i \leq R_i, \end{cases} \quad (2.5)$$

where Ω is the volume of a unit cell; $\mathbf{r}_i = \mathbf{r} - \mathbf{R} - \boldsymbol{\tau}_i$, in which $\boldsymbol{\tau}_i$ is the position of the atom in a unit cell, \mathbf{R} is a lattice vector, and R_i is the radius of the muffin-tin sphere of the i -th atom; l, m are the quantum numbers of angular momentum; the coefficients $a_{lm}^i(\mathbf{k} + \mathbf{G})$ and $b_{lm}^i(\mathbf{k} + \mathbf{G})$ are determined for each atom by imposing continuity on the basis functions and their first radial derivatives at the surface of the muffin-tin spheres; $u_l(E_l^i, r_i)$ and $\dot{u}_l(E_l^i, r_i)$ are radial solutions to the Schrödinger (or Dirac) equation at fixed energy parameter E_l^i and its energy derivative, respectively. Obviously, unlike in the conventional plane wave method, the LAPW basis functions depend on the position of atoms. In the nonrelativistic case, $u_l(r)$ is determined by the following differential equation at fixed E_l ,

$$\left[-\frac{d^2}{dr^2} - \frac{2d}{rdr} + \frac{l(l+1)}{r^2} + V_{eff}(r) - E_l \right] u_l(r) = 0, \quad (2.6)$$

and energy derivative $\dot{u}_l(r)$ is determined by

$$\left[-\frac{d^2}{dr^2} + \frac{l(l+1)}{r^2} + V_{eff}(r) - E_l \right] r\dot{u}_l(r) = ru_l(r). \quad (2.7)$$

In practical calculations, $u_l(r)$ is chosen to be normalized and orthogonal to $\dot{u}_l(r)$ in the muffin-tin. The norm of $\dot{u}_l(r)$, i.e. $\|\dot{u}_l\|$, together with the difference between energy parameter and the band energy, gives an indication of how well the energy linearization approximation works. It will be a good approximation for most purposes if $\|\dot{u}_l\| |E_l - \epsilon| \leq 1$ [2, 36]. When relativistic effects cannot be ignored, $u_l(r)$ and $\dot{u}_l(r)$ are the large component of the radial solutions of the j -weighted averaged Dirac equation [79]. Both large and small components are incorporated in constructing the charge density and evaluating the Hamiltonian matrix elements. But the matching requirements at the muffin-tin surface are enforced for only the large component and its derivative.

2.1.2 Potential

The potential in the Kohn-Sham equations is the combination of exchange-correlation term and Coulomb terms. The Coulomb terms, i.e. the sum of Hartree potential and the electron-ion potential, is determined by the charge density via Poisson's equation,

$$\nabla^2 V_c(\mathbf{r}) = -4\pi\rho(\mathbf{r}). \quad (2.8)$$

Two steps are followed: first obtain the potential in the interstitial region and then solve the boundary condition problem inside the muffin-tin spheres. An efficient scheme proposed by Weinert [80] is used to solve Poisson's equation. The Weinert scheme exploits the fact that the Coulomb potential at an interstitial point depends only on the interstitial charge and the multiple moments of the charge inside spheres. Since the multiple moments cannot define a unique charge density, we can construct a

well-behaved smooth pseudocharge density (having the same moments) to replace the rapidly varying real charge density inside the sphere, resulting in a rapidly convergent Fourier representation of the Coulomb potential in the interstitial region.

In the LAPW method, the real charge density is represented as

$$\rho(\mathbf{r}) = \begin{cases} \sum_{\mu} \rho_{\mu}(r_i) K_{\mu}(\mathbf{r}_i), & \mathbf{r}_i \in \text{sphere } i \\ \sum_s \rho_s \phi_s(\mathbf{r}_i), & \mathbf{r}_i \in \text{interstitial} \end{cases} \quad (2.9)$$

where $K_{\mu}(\mathbf{r}_i)$ are the lattice harmonics, which are the linear combinations of spherical harmonics symmetrized by the point group of the crystal, and \mathbf{r}_i is the position relative to the location of nucleus i (same as that defined in the previous section of Basis Functions); $\phi_s(\mathbf{r})$ are the 3-dimensional star functions, which are the plane waves symmetrized by the whole symmetry group of the crystal.

The pseudocharge density is defined as

$$\begin{aligned} \tilde{\rho}(\mathbf{r}) &= \sum_s \rho_s \phi_s(\mathbf{r}) + \sum_{i\mu} \Delta\tilde{\rho}_{\mu}^i(r_i) K_{\mu}(\mathbf{r}_i) \theta(\mathbf{r}_i) \\ &\equiv \sum_s \tilde{\rho}_s \phi_s(\mathbf{r}), \end{aligned} \quad (2.10)$$

where $\theta(\mathbf{r}_i)$ is the step function, which takes the value of one when the variable \mathbf{r}_i is within the sphere i and takes zero otherwise; $\Delta\tilde{\rho}_{\mu}^i(r_i)$ is chosen such that its multiple moments, $\Delta\tilde{q}_{lm}^i$, are the difference between the original charge density and the extended interstitial plane wave moments,

$$\Delta\tilde{q}_{lm}^i = q_{lm}^i - q_{lm}^{iPW}. \quad (2.11)$$

A polynomial form has been chosen to represent the difference charge density for convenience,

$$\Delta\tilde{\rho}_{lm}(r_i) = Q_{lm} \frac{r^l}{R_i^{2l+3}} \left[1 - \frac{r^2}{R_i^2} \right]^{N_i}, \quad (2.12)$$

where Q_{lm} is determined by Eq. (2.11); N_l is a convergence parameter and is chosen such that the truncated Fourier series for $\Delta\tilde{\rho}$ converges most rapidly for $R_i G_{max}$, where G_{max} is the maximum reciprocal lattice vector in the interstitial representation of the charge density and R_i is the muffin-tin radius.

Then the Coulomb potential in the interstitial region (including the spherical surfaces) is readily obtained in terms of the Fourier coefficients $\tilde{\rho}_s$ in Eq. (2.10),

$$V_c(\mathbf{r}) = \sum_s \frac{4\pi\tilde{\rho}_s}{G_s^2} \phi_s(\mathbf{r}). \quad (2.13)$$

The Coulomb potential inside the muffin-tin spheres may be easily obtained [2,80] by the standard Green's function method with the boundary conditions determined by Eq. (2.13).

For the exchange-correlation potential, the efficient complex fast Fourier transform (CFFT) technique is used in the star expansion in the interstitial region; in the muffin-tin region a least squares fit procedure is used to get a lattice harmonics expansion.

2.1.3 Charge Density

The charge density is constructed from the eigenvectors of the occupied states of the Kohn-Sham equations,

$$\rho(\mathbf{r}) = \sum_n \int |\psi_{n,\mathbf{k}}(\mathbf{r})|^2 d\mathbf{k}, \quad (2.14)$$

where the reciprocal space integration is over the first Brillouin zone. Taking into account the symmetry of the lattice, we need consider only the irreducible wedge of the Brillouin zone. Practically, k -point sampling is always used to approximate the

integration. The two commonly used methods are the tetrahedron method [81, 82] and the special k -point method [83–85].

In the tetrahedron method, the Brillouin zone is partitioned into tetrahedrons and the band energy and wavefunctions are calculated at the points on the vertices. Weight is assigned to each band at each k -point based on the volume of the tetrahedron below Fermi surface for the summation of charge density and total energy. In the special k -point method, the summations are performed at special k points with weights independent of band energy. These special points are set to optimize the convergence for smooth functions. For some cases where the bands intersect the Fermi surface, like in metals, artificial temperature broadening of the Fermi surface may be employed to facilitate the convergence (see Ref. [86, 87] and references therein). In this dissertation the special k -point method is used to sample the Brillouin zone integration.

The charge density constructed from k -point samplings in the irreducible BZ must be symmetrized with projection techniques using the lattice harmonics and 3-dimensional star functions in muffin-tin spheres and interstitial regions, respectively. In the process of achieving self-consistency, the input charge density for the next iteration is a mixture of the input and output charge densities of the previous iteration. Care should be taken to the choice of an appropriate mixing scheme to maximize the rate of convergence. [2]

2.1.4 Total Energy

The total energy of a system is one of the most fundamental quantities in LDA calculations. The importance of a scheme in which the total energy can be computed with accuracy, efficiency, and numerical stability, can be appreciated by considering the cancellation between very large kinetic and potential energy contributions. This problem could be more severe in the all-electron calculations for heavier atoms (like the transition metals and rare-earth elements) in which the chemically inert core electrons make the dominant contribution to the total energy.

Substituting the kinetic energy term with the use of Kohn-Sham equation, we can formulate the total energy per unit cell in the LDA as

$$\begin{aligned}
 E_{tot} = & \sum_{occ} \varepsilon_i - \frac{1}{2} \int \int \frac{\rho(\mathbf{r})\rho(\mathbf{r}')}{|\mathbf{r} - \mathbf{r}'|} d\mathbf{r}d\mathbf{r}' - \int \rho(\mathbf{r})\mu_{xc}(\mathbf{r})d\mathbf{r} \\
 & + \int \rho(\mathbf{r})\varepsilon_{xc}(\mathbf{r})d\mathbf{r} + \frac{1}{2} \sum'_{\alpha,\beta} \sum_{\mathbf{R}} \frac{Z_{\alpha}Z_{\beta}}{|\tau_{\alpha} - \tau_{\beta} + \mathbf{R}|}, \quad (2.15)
 \end{aligned}$$

where the summation for the eigenvalue of ε_i is performed for the occupied states; Z_{α} is the atomic number and the symbol of prime over Σ means α and β cannot be equal in the summation process; $\mu_{xc}(\mathbf{r})$ is the exchange-correlation potential in Kohn-Sham equation, given by

$$\mu_{xc}(\mathbf{r}) \equiv \frac{d}{d\rho(\mathbf{r})} \left[\rho(\mathbf{r})\varepsilon_{xc}(\rho(\mathbf{r})) \right]. \quad (2.16)$$

The total energy in Eq. (2.15) is further reformulated in the LAPW method to circumvent the Coulomb singularity at the nuclei [88]. With the use of lattice harmonics in muffin-tin spheres and star functions in the interstitial region, the form

in practical use is [76]:

$$\begin{aligned}
E_{tot} = \sum_{occ} \varepsilon_i & - \frac{1}{2} \sum_{\alpha} Z_{\alpha} \left[\frac{2(Z_{\alpha} - Q_{MT}^{\alpha})}{R_{\alpha}} + V_{MT}^{\alpha}(R_{\alpha}) \right] \\
& - \frac{1}{2} \int_I \rho(\mathbf{r}) \chi(\mathbf{r}) d\mathbf{r} - \frac{1}{2} \sum_{\alpha, \mu} \int_0^{R_{\alpha}} \chi_{\mu}(r_{\alpha}) \rho_{\mu}(r_{\alpha}) r_{\alpha}^2 dr_{\alpha} \\
& - \frac{1}{2} \sum_{\alpha} \int_0^{R_{\alpha}} \left[\frac{2Z_{\alpha} \sigma(r_{\alpha})}{r_{\alpha}} + \chi_{MT}(r_{\alpha}) \sigma(r_{\alpha}) \right] dr_{\alpha}, \quad (2.17)
\end{aligned}$$

where $\chi(\mathbf{r})$ is defined as

$$\chi(\mathbf{r}) = V_c + 2(\mu_{xc}(\mathbf{r})) - \varepsilon_{xc}(\mathbf{r}), \quad (2.18)$$

and V_c is the Coulomb potential only, Q_{MT}^{α} is the number of electrons inside the sphere α and $\sigma(r_{\alpha}) = 4\pi r^2 \rho(r_{\alpha})$. Note Rydberg atomic units are used in Eq. 2.17 and 2.18.

2.1.5 Pseudopotential

Pseudopotential approximation for the electron-ion interaction is now widely used in the modern electronic structure calculations. [3, 89] It is based on the observation that most physical properties of solids depend on the valence electrons to a much greater extent than on the core electrons. What the pseudopotential method does is to remove these core electrons and replace them and the strong ionic potential by a weaker pseudopotential that acts on the pseudo-wavefunctions rather than the true valence wavefunctions; this treatment paves the way for the large number of electronic structure calculations using the simple plane wave basis functions. Here are the conditions commonly imposed in the construction of the high quality atomic pseudopotential [90, 91]: (a) the pseudo-wavefunctions are nodeless for all r ; (b) beyond

a core radius r_c , the pseudopotential and the full potential are identical; (c) inside r_c the pseudopotential simulates with minimum error the electrostatic and scattering properties of the full potential at the eigenvalue energy, which is achieved by forcing the “pseudo” charge in the core region to converge identically to the real charge in the same region. Nonlocal pseudopotentials, which means a different potential for each angular momentum component of the wavefunction, are used to best describe the scattering properties of the core states. The quality of the pseudopotential is closely related to the choice of value r_c . A smaller r_c means that the true wavefunctions can be reproduced by the pseudo-wavefunctions closer to the nucleus and the pseudopotentials can be more transferable to a wider range of chemical environments. However, the pseudopotential generated with a smaller r_c displays sharper structures and hence becomes less suitable for the plane wave only based methods.

The LAPW method, which has no difficulty in handling the strong electron potential in the core region, conventionally involves the all-electron calculations. But incorporating pseudopotential in the LAPW method can eliminate the need to treat the chemically inert core states which contribute nothing to many physical properties. In 1979, Hamann [92] carried comparative investigations on bulk Si with LAPW method using the full potential and pseudopotentials. Yu, Singh and Krakauer [78] derived the atomic force formalism in LAPW method in both all-electron and pseudopotential schemes and achieved excellent agreement between the two schemes in practical calculations.

In the LAPW method, the nonlocal part of the pseudopotentials should be confined in the muffin-tin spheres to save extreme complexity in the evaluation of

Hamiltonian matrices. This requirement is satisfied by Kerker type pseudopotential [93] if the chosen core radii for any angular momentum l are all smaller than the muffin-tin radius of the corresponding atom. Kerker [93] proposed to construct the pseudopotential by directly modifying the atomic valence wavefunction instead of imposing the conditions on the pseudo-wavefunction via the potential. Two points are distinct compared with the other schemes, for example, the one proposed by Bachelet, Harmann and Schluter [91]. Outside the core region the nodeless radial pseudo-wavefunction is identical to the real wavefunction but inside it is represented by a well-behaved analytical function. Additionally, it requires both first and second derivatives of the radial pseudo-wavefunction to match onto the all-electron wavefunction at core radius r_c . The resulting pseudopotentials for different l thus match onto the all-electron potential minus the core screening at the respective core radii. Therefore the pseudopotential is local beyond the largest core radius for all angular momentum l . The pseudopotentials generated by this scheme are usually “hard” (i.e. strong) but this presents no difficulty for the LAPW method.

In order to employ the efficient Weinert scheme [80] (see the previous section of Potential) to treat the Coulomb potential in the LAPW formalism, the pseudopotential of atom α is separated into two parts: an ionic charge potential $-Z_{ion}^\alpha/r$, and the remaining terms given by part

$$\hat{v}_{ps}^\alpha(\mathbf{r}) = v_L^\alpha(r) + \hat{v}_{NL}^\alpha(\mathbf{r}) = v_L^\alpha(r) + \sum_{l=0}^{l_{max}} v_l^\alpha(r) \hat{P}_l, \quad (2.19)$$

where operator \hat{P}_l projects out the component of a wavefunction with angular momentum l ; the local part $v_L^\alpha(r)$ is the difference between the atomic pseudopotential for some chosen l and the ionic charge potential $-Z_{ion}^\alpha/r$; the nonlocal potentials

$v_l^\alpha(r)$ are obtained by subtracting the atomic pseudopotential for the chosen l from the atomic pseudopotential for all l up to l_{max} . The local part $v_L^\alpha(r)$ is short-ranged because at large r the difference between the atomic pseudopotential for any angular momentum l and the ionic charge potential $-Z_{ion}^\alpha/r$ diminishes. But it may extend beyond its own muffin-tin sphere. With the consideration of efficient representations in different regions, the local part $v_L^\alpha(r)$ is decomposed as [78],

$$v_L^\alpha(r) = \omega^\alpha(r) + \tilde{v}_\alpha(r), \quad (2.20)$$

where the two terms are defined as

$$\omega_\alpha(r) = \begin{cases} v_L^\alpha(r) - (A_\alpha + B_\alpha r^2), & r \leq R_\alpha \\ 0, & r \geq R_\alpha, \end{cases} \quad (2.21)$$

and

$$\tilde{v}_\alpha(r) = \begin{cases} A_\alpha + B_\alpha r^2, & r \leq R_\alpha \\ v_L^\alpha(r), & r \geq R_\alpha, \end{cases} \quad (2.22)$$

where the coefficients A_α and B_α are chosen such that $\tilde{v}_\alpha(r)$ and its derivative are continuous at the muffin-tin sphere surface $r = R_\alpha$. Since \tilde{v}_α is a smooth and slowly-varying function, the corresponding crystal counterpart $\tilde{V}(\mathbf{r})$,

$$\tilde{V}(\mathbf{r}) = \sum_\alpha \sum_{\mathbf{R}} \tilde{v}_\alpha(|\mathbf{r} - \tau_\alpha - \mathbf{R}|), \quad (2.23)$$

is easily expanded only with plane waves. Subsequently, it can be re-expressed into the usual LAPW representation.

Finally, the crystalline pseudopotential, the counterpart of $\hat{v}_{ps}^\alpha(r)$ in Eq. (2.19), is given by

$$\hat{V}_{ps}(\mathbf{r}) = \sum_\alpha \sum_{\mathbf{R}} \left[\omega_\alpha(|\mathbf{r} - \tau_\alpha - \mathbf{R}|) + \sum_l v_l^\alpha(|\mathbf{r} - \tau_\alpha - \mathbf{R}|) \hat{P}_l \right] + \tilde{V}(\mathbf{r}). \quad (2.24)$$

The new Hamiltonian in the Kohn-Sham equation becomes

$$H = \hat{T} + \hat{V}_{ps}(\mathbf{r}) + V_{eff}(\mathbf{r}) \quad (2.25)$$

where $V_{eff}(\mathbf{r})$ is

$$V_{eff}(\mathbf{r}) = - \sum_{\alpha} \sum_{\mathbf{R}} \frac{Z_{ion}^{\alpha}}{|\mathbf{r} - \tau_{\alpha} - \mathbf{R}|} + \int d\mathbf{r}' \frac{\rho(\mathbf{r}')}{|\mathbf{r} - \mathbf{r}'|} + \mu_{xc}(\mathbf{r}), \quad (2.26)$$

which differs from the effective potential in the all-electron formalism just by a replacing Z_{α} by Z_{ion}^{α} . In the pseudopotential formalism, u_l and \dot{u}_l that are used to construct the LAPW basis functions are now determined by the Hamiltonian

$$H_{MT}^{\alpha} = \hat{T} + \omega_{\alpha}(r) + \sum_{l'} v_l^{\alpha}(r) \hat{P}_{l'} + \tilde{V}^S(r) + V_{eff}^S(r), \quad (2.27)$$

where the superscript S denotes only the spherical part of the quantity is included.

2.1.6 Force

Force calculations are highly desirable for at least two reasons. Firstly, it is much more efficient to directly calculate the quantum-mechanical forces acting on the the atoms in determining the ground state structures of materials than to map out the energy surface via only total energy. When the system gets large and complex, the force calculation is enormously advantageous [2]. Secondly, force calculations greatly simplify the determination of vibration modes of materials and are indispensable in quantum-mechanical molecular-dynamics simulations [94]. Unfortunately, the use of position-dependent basis functions in the LAPW method complicates the force formalism, making such force calculation inaccessible until just a few years ago [78, 95–98]. Soler and William [95, 96] first derived force formula in

the LAPW method and did actual calculations for real materials. Yu, Singh and Krakauer [78] independently derived a different version, isolating the terms from the discontinuity of second derivatives of basis function on the muffin-tin surface, which were later shown [97] to be equivalent expressions for the force formula. Here the main points in the force formalism developed by Yu, Singh and Krakauer [78] for the LAPW method are briefly presented.

The quantum-mechanical force on an atom is given by the Hellmann-Feynman (HF) theorem [99,100]. Pulay [101] showed that there exist other terms known as incomplete basis set (IBS) corrections in practical density functional calculations with position-dependent basis functions. The IBS correction vanishes only when either i) the basis functions are position independent, or ii) the wavefunction is an exact solution to Kohn-Sham equation.

The force on atom α is expressed as

$$\begin{aligned}
\mathbf{F}^\alpha &= -\frac{\delta E}{\delta \tau_\alpha} \\
&= \mathbf{F}_{HF}^\alpha + \mathbf{F}_{IBS}^\alpha \\
&= Z_\alpha \frac{d}{d\tau_\alpha} \left[-\sum'_\beta \sum_{\mathbf{R}} \frac{Z_\beta}{|\tau_\alpha - \tau_\beta - \mathbf{R}|} + \int d\mathbf{r} \frac{\rho(\mathbf{r})}{|\tau_\alpha - \mathbf{r}|} \right] \\
&\quad - \frac{1}{\delta \tau_\alpha} \left[\sum_i n_i \delta \varepsilon_i - \int \rho(\mathbf{r}) \delta V_{eff}(\mathbf{r}) d\mathbf{r} \right], \tag{2.28}
\end{aligned}$$

where the quantum number (n, \mathbf{k}) is denoted as i for convenience, n_i is the occupation number for state i , and $V_{eff}(\mathbf{r})$ is the effective potential in Kohn-Sham equation, Eq. (1.1).

In the LAPW method, the IBS correction force comes from the core state and valence state contributions. The core states are fully relaxed in the radial direction

and the core correction to the HF force is due to the nonspherical crystal potential,

$$\begin{aligned}\mathbf{F}_{core}^\alpha &= -\frac{1}{\delta\tau_\alpha} \left[\sum_{\mathbf{i}} n_{\mathbf{i}} \delta\varepsilon_{\mathbf{i}} - \int \rho_c^\alpha(\mathbf{r}) \delta V_{eff}(\mathbf{r}) d\mathbf{r} \right] \\ &= \int \rho_c^\alpha(\mathbf{r}) \nabla V_{eff}(\mathbf{r}) d\mathbf{r}.\end{aligned}\quad (2.29)$$

Expressed in the form derived by Bendt and Zunger [102], the valence state contribution to the IBS force is given by

$$\begin{aligned}\mathbf{F}_{IBS}^\alpha &= -\frac{1}{\delta\tau_\alpha} \left[\sum_{\mathbf{i}} n_{\mathbf{i}} \delta\varepsilon_{\mathbf{i}} - \int \rho_v^\alpha(\mathbf{r}) \delta V_{eff}(\mathbf{r}) d\mathbf{r} \right] \\ &= -\sum_{\mathbf{i}} n_{\mathbf{i}} \left[\left\langle \frac{\delta\psi_{\mathbf{i}}}{\delta\tau_\alpha} \middle| (H - \varepsilon_{\mathbf{i}}) \middle| \psi_{\mathbf{i}} \right\rangle + \left\langle \psi_{\mathbf{i}} \middle| (H - \varepsilon_{\mathbf{i}}) \middle| \frac{\delta\psi_{\mathbf{i}}}{\delta\tau_\alpha} \right\rangle + \mathbf{D}_{\mathbf{i}}^\alpha \right],\end{aligned}\quad (2.30)$$

where $\mathbf{D}_{\mathbf{i}}^\alpha$ is the extra term due to the discontinuity of the second derivative of basis function at the muffin-tin surface [78]. $\mathbf{D}_{\mathbf{i}}^\alpha$ is evaluated as

$$\mathbf{D}_{\mathbf{i}}^\alpha = \oint \left[\left(\psi_{\mathbf{i}}^*(\mathbf{r}) \hat{T} \psi_{\mathbf{i}}(\mathbf{r}) \right)_{MT} - \left(\psi_{\mathbf{i}}^*(\mathbf{r}) \hat{T} \psi_{\mathbf{i}}(\mathbf{r}) \right)_I \right] d\mathbf{S}_\alpha.\quad (2.31)$$

where the integral is over the surface of the muffin-tin sphere; Suffixes *MT* and *I* mean that the kinetic energy is to be computed with representations of wavefunction in *MT* and interstitial regions, respectively. After several steps of derivation: representing wavefunction with LAPW basis functions, neglecting the small effect of the variation of the u_l and \dot{u}_l resulting from the change in the spherical potential as the muffin-tin center is moved [78], finally we have

$$\begin{aligned}\mathbf{F}_{IBS}^\alpha &= -\sum_{\mathbf{i}} n_{\mathbf{i}} \left[\mathbf{i} \sum_{\mathbf{G}, \mathbf{G}'} (\mathbf{G}' - \mathbf{G}) C_{\mathbf{i}}^*(\mathbf{G}) C_{\mathbf{i}}(\mathbf{G}') \left\langle \phi_{\mathbf{G}} \middle| H - \varepsilon_{\mathbf{i}} \middle| \phi_{\mathbf{G}'} \right\rangle_{MT} \right. \\ &\quad \left. - \left\langle \nabla \psi_{\mathbf{i}} \middle| (H - \varepsilon_{\mathbf{i}}) \middle| \psi_{\mathbf{i}} \right\rangle_{MT} - \left\langle \psi_{\mathbf{i}} \middle| (H - \varepsilon_{\mathbf{i}}) \middle| \nabla \psi_{\mathbf{i}} \right\rangle_{MT} + \mathbf{D}_{\mathbf{i}}^\alpha \right],\end{aligned}\quad (2.32)$$

where the suffix *MT* indicates the integrations are evaluated only in the muffin-tin sphere of atom α ; the index $(\mathbf{k} + \mathbf{G})$ of basis function ϕ is suppressed as \mathbf{G} for simplicity.

In the pseudopotential approach, the IBS correction to the HF force is separated into pseudopotential and nonpseudopotential contributions. Formulated in a similar fashion to Eq. (2.32), the total IBS force is

$$\begin{aligned}
\mathbf{F}_{IBS}^\alpha = & - \sum_i n_i \left[\mathbf{i} \sum_{\mathbf{G}, \mathbf{G}'} (\mathbf{G}' - \mathbf{G}) C_i^*(\mathbf{G}) C_i(\mathbf{G}') \left\langle \phi_{\mathbf{G}} \left| H - \varepsilon_i \right| \phi_{\mathbf{G}'} \right\rangle_{MT} \right. \\
& - \left\langle \nabla \psi_i \left| (H' - \varepsilon_i) \right| \psi_i \right\rangle_{MT} - \left\langle \psi_i \left| (H' - \varepsilon_i) \right| \nabla \psi_i \right\rangle_{MT} \\
& \left. + \mathbf{D}_i^\alpha + \left\langle \psi_i \left| \frac{\delta \tilde{V}}{\delta \tau_\alpha} \right| \psi_i \right\rangle \right], \tag{2.33}
\end{aligned}$$

where H and H' are as follows:

$$\begin{aligned}
H &= \hat{T} + V_{eff}(\mathbf{r}), \\
H' &= \hat{T} + V_{eff}(\mathbf{r}) + \tilde{V}(\mathbf{r}),
\end{aligned}$$

in which $\tilde{V}(\mathbf{r})$ and $V_{eff}(\mathbf{r})$ are specified in Eq. (2.23) and Eq. (2.24), respectively.

2.2 Linear Response Theory in the LAPW Method

The linear response density functional theory based on the Sternheimer method is powerful because it makes it possible to determine the electronic response to external perturbations of arbitrary wavelength (such as phonon perturbation), while keeping the numerical complexity of the calculation of the same order as for a self-consistent calculation for the unperturbed system. This theory significantly simplifies the direct determination of such quantities as Born effective charge tensor, phonon modes and frequencies at any arbitrary wavevector, dielectric tensor, piezoelectric properties and elastic constants, etc. However, its formalism in the LAPW

method [21] is much more complicated than that first developed by Baroni *et al.* [17] using the simple plane-wave basis set. The difficulty is again due to the position-dependence of the LAPW basis functions.

Let us introduce a phonon-like perturbation to the electronic system of a periodic crystal,

$$w_{i\alpha}(\mathbf{R}) = w_{i\alpha} e^{i\mathbf{q}\cdot\mathbf{R}}, \quad (2.34)$$

where $w_{i\alpha}(\mathbf{R})$ indicates the Cartesian α component of the displacement of atom i in the unit cell specified as \mathbf{R} . The first order change in the self-consistent field potential resulting from the perturbation is

$$V_{\text{SCF}}^{(1)}(\mathbf{r}) = - \sum_{\mathbf{R}, i} \frac{Z_i w_i(\mathbf{R}) \cdot (\mathbf{r} - \mathbf{R} - \boldsymbol{\tau}_i)}{|\mathbf{r} - \mathbf{R} - \boldsymbol{\tau}_i|^3} + \int \frac{\rho^{(1)}(\mathbf{r}')}{|\mathbf{r} - \mathbf{r}'|} d\mathbf{r}' + \rho^{(1)}(\mathbf{r}) \left[\frac{d\mu_{\text{xc}}}{d\rho} \right]_{\rho=\rho_0(\mathbf{r})}, \quad (2.35)$$

where $\rho_0(\mathbf{r})$ is the charge density of unperturbed system and the linear order change of charge density is

$$\rho^{(1)}(\mathbf{r}) = 2 \sum_{n, \mathbf{k}} \psi_{n\mathbf{k}}^*(\mathbf{r}) \psi_{n\mathbf{k}}^{(1)}(\mathbf{r}). \quad (2.36)$$

in the traveling-wave representation.

The linear order change of the wavefunction arises from the changes of the variational expansion coefficients and the basis functions,

$$\psi_{n\mathbf{k}}^{(1)}(\mathbf{r}) = \sum_{\mathbf{G}} \left[C_{n\mathbf{k}}^{(1)}(\mathbf{G}) \phi_{\mathbf{k}+\mathbf{q}+\mathbf{G}}(\mathbf{r}) + C_{n\mathbf{k}}(\mathbf{G}) \phi_{\mathbf{k}+\mathbf{G}}^{(1)}(\mathbf{r}) \right]. \quad (2.37)$$

Neglecting the relaxation of muffin-tin orbitals u_l and \dot{u}_l when the atoms are moved [78], we obtain the linear order change of basis function

$$\phi_{\mathbf{k}+\mathbf{G}}^{(1)}(\mathbf{r}) = \frac{\partial \phi_{\mathbf{k}+\mathbf{G}}}{\partial \mathbf{w}} \cdot \mathbf{w} = \left[i(\mathbf{k} + \mathbf{G}) - \nabla \right] \phi_{\mathbf{k}+\mathbf{G}}(\mathbf{r}) \cdot \mathbf{w}, \quad (2.38)$$

where \mathbf{w} is used to represent the atomic displacements in Eq. (2.34) without specifying the index of individual atoms in order to make expression concise. After careful and lengthy derivation [21], we have the following linear matrix equation to determine the linear order variational coefficients:

$$\begin{aligned}
& \sum_{\mathbf{G}'} \left\langle \phi_{\mathbf{k}+\mathbf{q}+\mathbf{G}} \left| (\varepsilon_{\mathbf{n}\mathbf{k}} - H) \right| \phi_{\mathbf{k}+\mathbf{q}+\mathbf{G}'} \right\rangle C_{\mathbf{n}\mathbf{k}}^{(1)}(\mathbf{G}') \\
&= \sum_{\mathbf{G}'} \left[\left\langle \phi_{\mathbf{k}+\mathbf{q}+\mathbf{G}} \left| V_{\text{SCF}}^{(1)} \right| \phi_{\mathbf{k}+\mathbf{G}'} \right\rangle + \left\langle \frac{\partial \phi_{\mathbf{k}+\mathbf{q}+\mathbf{G}}}{\partial \mathbf{w}} \cdot \mathbf{w}^* \left| (H - \varepsilon_{\mathbf{n}\mathbf{k}}) \right| \phi_{\mathbf{k}+\mathbf{G}'} \right\rangle_{\text{MT}} \right. \\
&+ \left. \left\langle \phi_{\mathbf{k}+\mathbf{q}+\mathbf{G}} \left| (H - \varepsilon_{\mathbf{n}\mathbf{k}}) \right| \frac{\partial \phi_{\mathbf{k}+\mathbf{G}'}}{\partial \mathbf{w}} \cdot \mathbf{w} \right\rangle_{\text{MT}} \right. \\
&+ \left. \delta \left\langle \phi_{\mathbf{k}+\mathbf{q}+\mathbf{G}} \left| \hat{T} \right| \phi_{\mathbf{k}+\mathbf{G}'} \right\rangle \right] C_{\mathbf{n}\mathbf{k}}(\mathbf{G}'), \tag{2.39}
\end{aligned}$$

where H and $\varepsilon_{\mathbf{n}\mathbf{k}}$ are the Hamiltonian and eigenvalues in the Kohn-Sham equation for the unperturbed system. The last term in the above equation represents the finite change in the kinetic energy owing to the discontinuity of the second order derivative of the LAPW basis functions at the muffin-tin boundary. It is evaluated as

$$\begin{aligned}
& \delta \left\langle \phi_{\mathbf{k}+\mathbf{q}+\mathbf{G}} \left| \hat{T} \right| \phi_{\mathbf{k}+\mathbf{G}'} \right\rangle \\
&= \sum_i \oint \left[\phi_{\mathbf{k}+\mathbf{q}+\mathbf{G}}^*(\mathbf{r}) \hat{T} \phi_{\mathbf{k}+\mathbf{G}'}(\mathbf{r}) \Big|_{\text{MT}} - \phi_{\mathbf{k}+\mathbf{q}+\mathbf{G}}^*(\mathbf{r}) \hat{T} \phi_{\mathbf{k}+\mathbf{G}'}(\mathbf{r}) \Big|_{\text{I}} \right] d\mathbf{S}_i \cdot \mathbf{w}_i, \tag{2.40}
\end{aligned}$$

where suffixes MT and I mean again that the kinetic energy is to be calculated with the representations of basis functions in muffin-tin and interstitial regions, respectively.

The basic idea in Sternheimer method is to solve Eq. (2.39) for the first order change of the one-electron wavefunction, $\psi_{\mathbf{n}\mathbf{k}}^{(1)}(\mathbf{r})$, directly, instead of using the slowly convergent summation of the conduction bands in the conventional perturbation theory expression. In practice, an iterative diagonalization technique is used to solve Eq.

(2.39), which involves only the occupied states of the unperturbed system. With Eq. (2.37), (2.38), and (2.39) as supplemental conditions, Eq. (2.35) and (2.36) must be solved iteratively to achieve self-consistency.

2.2.1 First-order Forces and Dynamical Matrix

First-order forces, or second-order total energy can be determined from the first-order charge density and orbitals [18]. This fact is used in the linear response density functional calculations to construct the dynamical matrix. The force-constants $C_{i\alpha,j\beta}(\mathbf{R} - \mathbf{R}')$ are defined as the second derivatives of the total energy of the solid system with respect to the atomic displacements, or equivalently, as the coefficients in the first-order forces acting on one atom due to the displacement of another from its equilibrium position:

$$E^{(2)} = \frac{1}{2} \sum_{\mathbf{R}, \mathbf{R}'} \sum_{i\alpha, j\beta} C_{i\alpha, j\beta}(\mathbf{R} - \mathbf{R}') w_{i\alpha}(\mathbf{R}) w_{j\beta}(\mathbf{R}'), \quad (2.41)$$

$$F_{i\alpha}^{(1)}(\mathbf{R}) = -\frac{\partial E^{(2)}}{\partial w_{i\alpha}(\mathbf{R})} = -\sum_{\mathbf{R}'} \sum_{j\beta} C_{i\alpha, j\beta}(\mathbf{R} - \mathbf{R}') w_{j\beta}(\mathbf{R}'). \quad (2.42)$$

One needs to calculate up to $3N_{at}$ (where N_{at} is the number of atoms in the primitive unit cell) periodic lattice distortions $w_{i\alpha}(\mathbf{R})$ that are defined in Eq. (2.34) to directly determine the $(3N_{at} \times 3N_{at})$ force constant matrix in reciprocal space $\tilde{C}_{i\alpha, j\beta}(\mathbf{q})$:

$$F_{i\alpha}^{(1)}(\mathbf{R}) = -\sum_{j\beta} \tilde{C}_{i\alpha, j\beta}(\mathbf{q}) w_{j\beta} e^{i\mathbf{q} \cdot \mathbf{R}}. \quad (2.43)$$

where

$$\tilde{C}_{i\alpha,j\beta}(\mathbf{q}) \equiv \sum_{\mathbf{R}} C_{i\alpha,j\beta}(\mathbf{q})(\mathbf{R}) e^{-i\mathbf{q}\cdot\mathbf{R}}. \quad (2.44)$$

The dynamical matrix is readily related to $\tilde{C}_{i\alpha,j\beta}(\mathbf{q})$ through a mass factor:

$$\tilde{D}_{i\alpha,j\beta}(\mathbf{q}) = \frac{\tilde{C}_{i\alpha,j\beta}(\mathbf{q})}{\sqrt{M_i M_j}}, \quad (2.45)$$

where M_i is the mass of the i th atom in the unit cell. The phonon frequencies and normal modes can be obtained by solving the standard secular equation:

$$\left| \tilde{D}_{i\alpha,j\beta}(\mathbf{q}) - \omega^2(\mathbf{q})\delta_{\alpha\beta}\delta_{ij} \right| = 0 \quad (2.46)$$

In practice, the symmetry of the dynamical matrix $\tilde{D}_{i\alpha,j\beta}(\mathbf{q})$ is used to reduce the number of phonon distortions that have to be calculated. A general symmetry operation that sends a crystal into itself is $\{\mathbf{S}|\mathbf{v}(S) + \mathbf{x}(m)\}$, where \mathbf{S} is a 3×3 real, orthogonal matrix representation of one of the proper or improper rotations of the point group of crystal, $\mathbf{v}(S)$ is fractional translation associated with S , and $\mathbf{x}(m)$ is a translation vector of the crystal. Under this operation, the position vector of the κ th atom in the l th unit cell, $\mathbf{x}(l\kappa)$, is sent into an equivalent site $\mathbf{x}(LK)$:

$$\left\{ \mathbf{S} \left| \mathbf{v}(S) + \mathbf{x}(m) \right. \right\} \mathbf{x}(l\kappa) = \mathbf{S}\mathbf{x}(l\kappa) + \mathbf{v}(S) + \mathbf{x}(m) = \mathbf{x}(LK). \quad (2.47)$$

The dynamical matrix transforms as [103]

$$\tilde{D}(\mathbf{S}\mathbf{q}) = \Gamma\left(\mathbf{q}; \left\{ \mathbf{S} \left| \mathbf{v}(S) + \mathbf{x}(m) \right. \right\}\right) \tilde{D}(\mathbf{q}) \Gamma^\dagger\left(\mathbf{q}; \left\{ \mathbf{S} \left| \mathbf{v}(S) + \mathbf{x}(m) \right. \right\}\right) \quad (2.48)$$

where the unitary matrix $\Gamma(\mathbf{q}; \{\mathbf{S}|\mathbf{v}(S) + \mathbf{x}(m)\})$ is defined as

$$\begin{aligned} & \Gamma_{\alpha\beta}\left(\kappa\kappa'|\mathbf{q}; \left\{ \mathbf{S} \left| \mathbf{v}(S) + \mathbf{x}(m) \right. \right\}\right) = S_{\alpha\beta}\delta\left(F_0^{-1}(\kappa; S), \kappa'\right) \\ & \times \exp\left(i\mathbf{q} \cdot \left[\left\{ \mathbf{S} \left| \mathbf{v}(S) + \mathbf{x}(m) \right. \right\}^{-1} \mathbf{x}(0\kappa) - \mathbf{x}(0\kappa') \right]\right). \end{aligned} \quad (2.49)$$

The notation $\kappa = F_0^{-1}(K; S)$ expresses the fact that index K uniquely labels the kind of atom κ that is sent into the K position by symmetry operation $\{\mathbf{S}|\mathbf{v}(S) + \mathbf{x}(m)\}$.

For the symmetry operations that send wavevector \mathbf{q} into itself or that differs from \mathbf{q} by only reciprocal lattice vectors, we have

$$\Gamma\left(\mathbf{q}; \left\{\mathbf{S}|\mathbf{v}(S) + \mathbf{x}(m)\right\}\right) \widetilde{D}(\mathbf{q}) \Gamma^{-1}\left(\mathbf{q}; \left\{\mathbf{S}|\mathbf{v}(S) + \mathbf{x}(m)\right\}\right) = \widetilde{D}(\mathbf{q}). \quad (2.50)$$

Eq. (2.50) is used to determine the form of $\widetilde{D}(\mathbf{q})$, that is, the independent, nonzero elements of this matrix. Then the necessary and appropriate phonon distortions are proposed for linear response calculations to determine $\widetilde{D}(\mathbf{q})$. Of course, This process is more helpful for the high symmetry wavevectors.

2.2.2 Dielectric Tensor and Born Effective Charge Tensor

Another important advantage of linear response method is that it also treats the infinitesimal macroscopic fields with ease. As mentioned in Chapter 1, the effect of macroscopic field cannot be taken into account in the supercell method directly because it is incompatible with the Born-von Karman periodic boundary condition. Usually one has to calculate for several finite wavevectors with large supercells and then extrapolate the results to zero \mathbf{q} . In the linear response method, the long wavelength limit can be taken analytically [17, 19, 20]. In practice, we choose an alternative scheme which is more straightforward, calculating the the macroscopic effects through a definite but very small wavevector. Our procedure is fundamentally different from the supercell method, since the wavevector \mathbf{q} can be as small as allowed by numerical considerations and no additional computational cost is involved for

smaller \mathbf{q} .

The dielectric tensor and Born effective charge tensors are obtained in the long-wavelength limit as

$$\hat{\mathbf{q}} \cdot \epsilon_\infty \cdot \hat{\mathbf{q}} = \lim_{\mathbf{q} \rightarrow 0} \left[1 + \frac{V_{ind}(\mathbf{q})}{V_{total}(\mathbf{q})} \right], \quad (2.51)$$

$$Z_{\alpha,\beta}^*(i) = Z_i + \Omega \left. \frac{\partial P_\alpha}{\partial \omega_{i\beta}} \right|_{\mathbf{E}=0}, \quad (2.52)$$

where V_{ind} is the induced potential when the macroscopic field is applied and Z_i is the ionic charge of the i th ion. In the calculation of the dielectric tensor, the external perturbation, which is the first term in Eq. (2.35) for the phonon calculation, is replaced by external field: $V_{ext}^{(1)}(\mathbf{r}) = iE_{ext}e^{i\mathbf{q}\cdot\mathbf{r}}/q$. In the determination of Born effective charge tensors, phonon-like perturbations of small wavevectors are used to calculate the macroscopic polarization, while the electric field is set to be zero:

$$\begin{aligned} \nabla \cdot \mathbf{P} &= -\rho^{(1)}(\mathbf{r}), \\ \nabla \cdot \left[\sum_{\mathbf{G}} \mathbf{P}((\mathbf{q} + \mathbf{G}))e^{i\mathbf{q}+\mathbf{G}\cdot\mathbf{r}} \right] &= -\sum_{\mathbf{G}} \rho^{(1)}(\mathbf{q} + \mathbf{G})e^{i(\mathbf{q}+\mathbf{G})\cdot\mathbf{r}}, \\ \mathbf{P} = \hat{\mathbf{q}} \cdot \mathbf{P}(0) &= \lim_{\mathbf{q} \rightarrow 0} \frac{i}{q} \rho^{(1)}(\mathbf{q}). \end{aligned} \quad (2.53)$$

Theoretically, Born effective charge tensors should satisfy the acoustic sum rule [104] which reflects the charge neutrality in materials:

$$\sum_i Z_{\alpha,\beta}^*(i) = 0. \quad (2.54)$$

However, in approximate calculations, the acoustic sum rule is not ideally satisfied. The magnitude of such deviation depends strongly on the mesh of \mathbf{k} -point sampling for

the Brillouin zone integration. A denser k-point mesh tends to reduce the deviation toward zero.

In the calculations for dielectric tensor and Born-effective charge tensor, we have chosen the small wavevector \mathbf{q} to be of order one hundredth of the reciprocal basis vectors. It is worth mentioning that the Born-effective charge tensor can also be determined by so-called Berry-phase calculations [105,106] to obtain a finite difference approximation to the derivative in Eq. (2.52).

2.2.3 LO Phonons at Zone Center and Phonon Dispersions in BZ

In polar semiconductors and insulators, the long-range Coulomb interaction contributes to the macroscopic field for longitudinal optical (LO) phonons, giving rise to the LO and TO (transverse optical modes) splitting at the Brillouin zone center. At finite wavevectors, \mathbf{q} , such contributions are automatically included in the linear response calculations. In the long wavelength limit $\mathbf{q} \rightarrow \mathbf{0}$, it is more convenient to separate the dynamical matrix into two terms [20,103,104]. One term is analytic in \mathbf{q} , corresponding to the response to a zero-center phonon with no macroscopic electric field, and this is just the dynamical matrix calculated for the TO modes. The other (nonanalytic) term is related to the Born effective charge tensor and the high-frequency dielectric tensor.

We have

$$\tilde{D}_{i\alpha,j\beta} = \tilde{D}_{i\alpha,j\beta}^{an} + \tilde{D}_{i\alpha,j\beta}^{non}, \quad (2.55)$$

where

$$\widetilde{D}_{i\alpha,j\beta}^{non} = \frac{4\pi e^2}{\Omega\sqrt{M_i M_j}} \frac{(\mathbf{q} \cdot \mathbf{Z}_i^*)_\alpha (\mathbf{q} \cdot \mathbf{Z}_j^*)_\beta}{\mathbf{q} \cdot \epsilon_\infty \cdot \mathbf{q}}. \quad (2.56)$$

Diagonalizing $\widetilde{D}_{i\alpha,j\beta}$ gives LO and TO phonon frequencies at the zone center. The LO phonon frequencies are direction-dependent for general cases and are isotropic only in crystals with high symmetry.

The phonon dispersions throughout the Brillouin zone can be obtained from the real space force constants. The procedure we usually choose is to calculate $\widetilde{D}_{i\alpha,j\beta}(\mathbf{q})$ on a uniform grid of \mathbf{q} points in the BZ. In polar semiconductors and insulators, the short-range real-space force constants are then obtained by Inverse Fourier Transform, after subtracting the long-range dipolar contributions. For isotropic effective charges, the dipole-dipole interaction between two atoms is

$$C_{i\alpha,j\beta}^{d-d}(\mathbf{R} - \mathbf{R}') = \frac{Z_i^* Z_j^*}{\epsilon_\infty} \left[\frac{\delta_{\alpha\beta}}{r^3} - \frac{3r_\alpha r_\beta}{r^5} \right], \quad (2.57)$$

where $\mathbf{r} = \mathbf{R}' - \mathbf{R} + \tau_j - \tau_i$. The dipole-dipole component of the force constants in reciprocal space $\widetilde{C}_{i\alpha,j\beta}^{d-d}(\mathbf{q})$ can be expressed analytically in terms of Born effective charges and dielectric constant via Ewald summation techniques. [20,107–109] Then we can have $\widetilde{C}_{i\alpha,j\beta}(\mathbf{q})$ at any wavevector \mathbf{q} by

$$\widetilde{C}_{i\alpha,j\beta}(\mathbf{q}) = \widetilde{C}_{i\alpha,j\beta}^{d-d}(\mathbf{q}) + \widetilde{C}_{i\alpha,j\beta}^{short-range}(\mathbf{q}), \quad (2.58)$$

where $\widetilde{C}_{i\alpha,j\beta}^{short-range}(\mathbf{q})$ is constructed from the short-range force constants through Fourier Transform. Formulas for the case of general Born-effective charge tensors have been given by Gonze *et al.* [27] recently.

Chapter 3

Lattice Dynamics of CuCl

3.1 Introduction

CuCl is an interesting material that displays many unusual properties and has received special attention in the past two decades. It has the zincblende structure at room temperature and below and is just on the covalent side of Phillips' critical ionicity [110], close to where the NaCl or CsCl structures are preferred over zincblende. Experiments observe a sharp drop of electrical resistance by a factor of 10^7 in CuCl at a pressure about 4 GPa [111, 112] and a diamagnetic susceptibility anomaly above 90 K in rapidly cooled samples [111]. Experiments also find a negative thermal expansion coefficient below 100 K [113] and irregular temperature and pressure dependence of the elastic properties [114]. Investigations from X-ray [115, 116] and neutron diffraction [117] data in CuCl, together with other Cu halides and AgI, suggest structural disorder [118]. The value for the cation mean-square vibrational amplitudes $\sqrt{\langle u^2 \rangle_{Cu}}$ in CuCl is reported [118] to be unusually high even when the

temperature is lowered to 5 K, while at elevated temperatures a superionic conducting phase [119, 120] is formed. CuCl is a strongly anharmonic material, which is clearly evidenced by neutron scattering [121]. When the temperature is raised to as low as room temperature, most phonon peaks disappear because of the strong anharmonic interaction [121]! In addition, the phonon spectra of CuCl shows unusual features such as a double-peak structure of the long wavelength optic modes (see Figure 3.1). The zincblende structure of CuCl contains two atoms in the primitive unit cell so that there is only one triply degenerate fundamental optic mode, which is both Raman and infrared active. This mode is split into a transverse optic (TO) and a longitudinal optic (LO) mode by the macroscopic electric field that accompanies the LO mode. However, experiments with inelastic neutron scattering, infrared absorption and reflection, Raman scattering, as well as polariton dispersion, have unequivocally observed extra zone center modes at low temperature [121–131]. Furthermore, neutron scattering measurements show that the splitting of the double-peak structure is strongly wavevector dependent and turns into a normal spectrum away from the zone center [126]. Despite years of intensive efforts to understand these phonon anomalies in CuCl (also in CuBr), their origin is still unresolved and two competing models have emerged.

Krauzman and his colleagues [123, 131] described the extra modes near the zone center as arising from anharmonic coupling between the $\text{TO}(\Gamma)$ phonon and two-phonon continuum. This anharmonic coupling is assumed so strong that it repels the TO mode and gives rise to another TO peak. The predictions of this model have been discussed by Kanellis *et al.* [132, 133]. By contrast, the off-center model

of Vardeny, Livescu and Brafman (see Ref. [128,134] and references therein) assumes the existence of four equivalent secondary minima for the Cu^+ cation lying along the $[1\ 1\ 1]$ directions in addition to its ideal lattice site. They assume that the tunneling rate between the central and the off-center sites is much lower than that among the displaced sites, yielding different sublattices that both have the same T_d symmetry, namely the ideal site and the tunneling off-center sites. The presence of cations at two different sites gives rise to the extra set of observed modes and the model can explain other vibrational anomalies observed by Raman scattering, infrared and phonon-polariton measurements. Kremer and Weyrich [135] investigated the problem with the local density functional approximation (LDA) total energy calculations. They calculated the total energy for a series of Cu sublattice displacements in $[1\ 1\ 1]$ directions, and failed to identify any secondary energy minima for the potential of cation Cu^+ . But, more recently, Wei, Zhang and Zunger [136] reinvestigated the problem and did find a secondary relative minimum along the $[1\ 1\ 1]$ directions outside the trigonal face for the Cu^+ cation in CuCl and CuBr , giving support to the off-center model. What they have done is to displace one Cu atom in $[1\ 1\ 1]$ direction but keep all the other atoms unmoved in a supercell which contains up to sixteen atoms, instead of moving the whole Cu sublattice together as Kremer and Weyrich did. Wei *et al.* also relaxed the other atoms in the supercell. They find that the secondary minimum becomes deeper as expected but still stays above the energy of the unperturbed zincblende structure. This double-well energy surface is reminiscent of that found in perovskite structure ferroelectrics and some high-temperature cuprate superconductors, except that there the displaced site corresponds to the global energy

minimum [137, 138]. It is thus of great interest to map out the Born-Oppenheimer surface of CuCl near the ideal zincblende structure. We have investigated the lattice dynamics of CuCl with first principles linear response calculations [43], calculating the Born effective charge, dielectric constant and phonon dispersions in the Brillouin zone. Comparisons with experiment and previous theoretical work are presented.

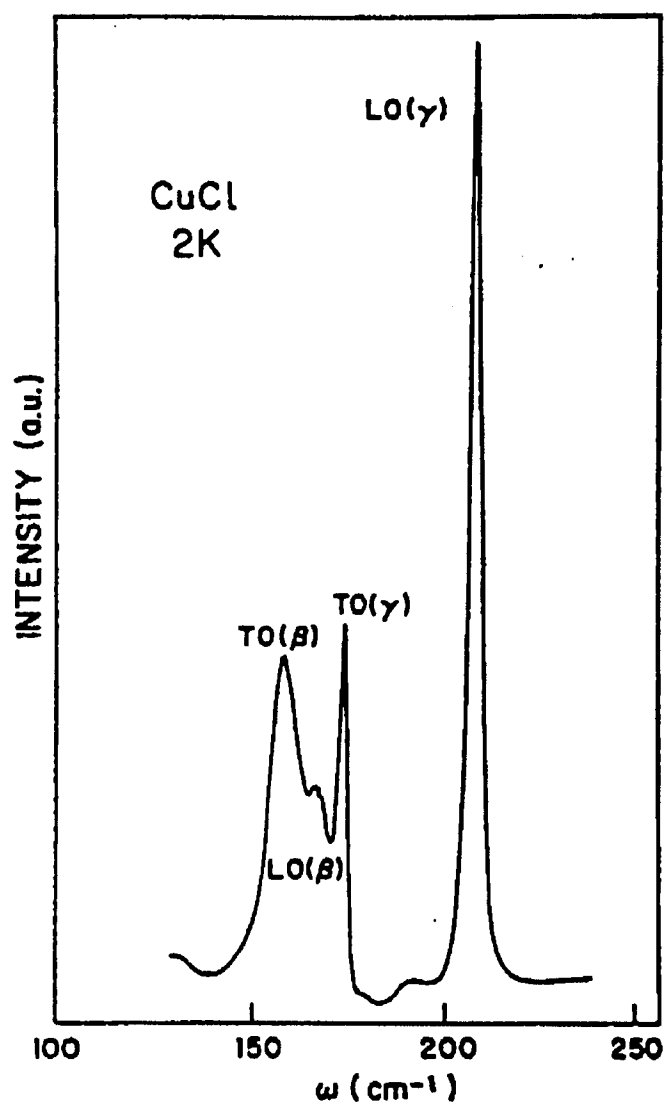


Figure 3.1: Raman spectrum of CuCl at 2 K (from Ref. [128]). The assignments of TO(β), LO(β), TO(γ), and LO(γ) are given by Ref. [128].

3.2 Computational Details

Linear response calculations are performed using the recently developed LAPW linear response method [21]. The use of LAPW basis functions greatly facilitates the treatment of localized valence wave functions such as those derived from the Cu $3d$ orbitals. In this method, the dynamical matrix is calculated at each \mathbf{q} point from the first-order forces, and the frequencies are obtained by standard matrix diagonalization. Kerker type [93] pseudopotentials are used to avoid dealing with core states. The resulting non-local d pseudopotential is very strong, but since the LAPW method employs a dual representation of the wave functions, charge density and potential, such very strong potentials are easily handled. A Hedin-Lunqvist form exchange-correlation potential [60] is used. The muffin-tin radii are 2.14 *a.u.*(atomic unit) for Cu and 2.09 *a.u.* for Cl. A (4 4 4) k -point mesh [83–85] is used for the Brillouin zone(BZ) integration, which yields 2 special k -points in the irreducible BZ wedge for the unperturbed lattice. Denser k -point meshes are used to calculate Born effective charges and dielectric constant. The plane wave kinetic energy cutoff is 16.5 Ry, yielding approximately 300 LAPW basis functions at each k -point and convergence of the calculated phonon frequencies to better than 0.05 THz.

At first we have performed conventional LDA total energy calculations to obtain some equilibrium state properties. Fitting the total energies to Murnaghan's equation [139],

$$E(V) = \frac{BV}{B'(B' - 1)} \left[B' \left(1 - \frac{V_0}{V} \right) + \left(\frac{V_0}{V} \right)^{B'} - 1 \right] + E(V_0), \quad (3.1)$$

where V_0 , B and B' are equilibrium volume, bulk modulus and bulk modulus pressure

derivative, respectively. We find: the theoretical lattice constant (corresponding to the volume V_0 above) is 5.33 Å, only slightly smaller than the experimental value 5.41 Å [140]; the bulk modulus is 0.62 Mbar, which is in good agreement with the experimental value of 0.654 Mbar [135] derived from inelastic neutron scattering at liquid helium temperature [121]; the calculated bulk modulus pressure derivative is 3.46 and no experimental data is available for comparison. To compare the calculated phonon frequencies with experimental data, all linear response calculations are performed at the experimental lattice constant. A small wavevector $\mathbf{q} = 0.01 (1, 1, 1) \frac{2\pi}{a}$ has been used in calculating the dielectric constant and Born effective charges.

As mentioned in Chapter 2, in order to reduce the number of displacements for which linear response calculations have to be performed in determining the dynamical matrix $\widetilde{D}(\mathbf{q})$, we have employed the symmetry group of crystal to find the independent, non-zero elements in $\widetilde{D}(\mathbf{q})$. For example, the dynamical matrix at the high symmetry points X, i.e. $\mathbf{q} = (\frac{1}{2}, 0, 0) \frac{2\pi}{a}$, and L, i.e. $\mathbf{q} = (\frac{1}{2}, \frac{1}{2}, \frac{1}{2}) \frac{2\pi}{a}$, have the form

$$\widetilde{D}(X) = \begin{pmatrix} \alpha_1 & 0 & 0 & 0 & \gamma & 0 \\ 0 & \alpha_1 & 0 & \gamma & 0 & 0 \\ 0 & 0 & \alpha_2 & 0 & 0 & 0 \\ 0 & \gamma & 0 & \beta_1 & 0 & 0 \\ \gamma & 0 & 0 & 0 & \beta_1 & 0 \\ 0 & 0 & 0 & 0 & 0 & \beta_2 \end{pmatrix},$$

$$\tilde{D}(L) = \begin{pmatrix} \alpha_1 & \alpha_2 & \alpha_2 & \gamma_1 & \gamma_2 & \gamma_2 \\ \alpha_2 & \alpha_1 & \alpha_2 & \gamma_2 & \gamma_1 & \gamma_2 \\ \alpha_2 & \alpha_2 & \alpha_1 & \gamma_2 & \gamma_2 & \gamma_1 \\ \gamma_1 & \gamma_2 & \gamma_2 & \beta_1 & \beta_2 & \beta_2 \\ \gamma_2 & \gamma_1 & \gamma_2 & \beta_2 & \beta_1 & \beta_2 \\ \gamma_2 & \gamma_2 & \gamma_1 & \beta_2 & \beta_2 & \beta_1 \end{pmatrix},$$

where all elements are real numbers. Calculation of one configuration is enough to find each element in $\tilde{D}(X)$: we have chosen the displacement vector as $(1, 0, 1, 1, 0, 1)a$, which corresponds to displacing both Cu and Cl by $(1, 0, 1)a$. For $\tilde{D}(L)$, we have used two configurations, with displacement vectors as $(1, 0, 0, 0, 0, 0)a$ and $(0, 0, 0, 1, 0, 0)a$ respectively.

3.3 Frozen Phonon Calculations at Γ -point

It is well-known that the phonon frequencies can be determined by the frozen phonon method. To check the linear response approach, we performed total energy and forces calculations for frozen optic-phonon configurations at the Γ -point in CuCl and then compared with the corresponding linear response results. In ideal structure, Cu and Cl are located at the origin $a(0\ 0\ 0)$ and $0.25a(1\ 1\ 1)$, respectively, where a is the lattice constant. Two distorted configurations have been chosen: keep Cu still but move Cl to $0.24a(1\ 1\ 1)$ and $0.26a(1\ 1\ 1)$. The results from frozen phonon calculations are presented in Table 3.1. As expected, the forces acting on Cu and Cl sum to be zero.

Because the crystal does not have inversion symmetry, the same magnitude of

Table 3.1: Results from frozen-phonon calculations at Γ -point in CuCl.

Location of Cl	$\Delta E(\text{mRy})$	$F_{Cu}(\text{mRy}/a.u.)$	$F_{Cl}(\text{mRy}/a.u.)$
0.24 a (1 1 1)	0.9650	- 6.963 (1 1 1)	6.963 (1 1 1)
0.26 a (1 1 1)	0.6061	3.439 (1 1 1)	- 3.439 (1 1 1)

displacements in opposite directions give rather different energy changes and forces. This implies that anharmonic terms are making appreciable contributions to the energy differences even when the displacements appear to be small compared to lattice constant. The following simple equations indicate how to find the phonon frequency from total energy or forces when the cubic term of the displacement is kept in the energy difference expression:

$$\Delta E = \frac{1}{2}\mu\omega^2 u^2 + bu^3, \quad (3.2)$$

$$F = -\mu\omega^2 u - 3bu^2, \quad (3.3)$$

where u is the atomic displacement, μ the reduced mass of Cu and Cl atoms, ω the angular frequency, and b a coefficient. Exploiting the fact that the two displacements have the same magnitude and opposite signs, we have :

$$\omega = \sqrt{\frac{\Delta E_1 + \Delta E_2}{\mu u^2}},$$

$$\omega = \sqrt{\frac{|F_1| + |F_2|}{\mu|u|}}.$$

Table 3.2: Phonon frequencies from frozen-phonon and linear response calculations at Γ -point in CuCl.

$f_{\Delta E}$ (THz)	f_F (THz)	f_{LR} (THz)
5.12	5.16	5.05

Table 3.2 lists the obtained phonon frequencies from total energy, forces and linear response calculations, showing agreement of the 1% level. As shown in Table 3.2, the frequencies from independent total energy and forces calculations are larger than the frequency obtained from the linear response calculations by about 1-2%. We attribute the small discrepancy to higher order anharmonic terms. If we use smaller displacements or include higher order anharmonic terms in Eq. (3.2) and Eq. (3.3), the agreement will be improved.

3.4 Phonons at Γ -point, Z^* and ϵ_∞

Since CuCl is a polar semiconductor, the long-range Coulomb interaction contributes to the macroscopic electric field for LO phonons. In the cubic zincblende structure the relationship between the angular frequencies of the TO and LO modes at the Γ point simplifies to:

$$\omega_{LO}^2 = \omega_{TO}^2 + \omega_p^2, \quad (3.4)$$

where

$$\omega_p = \sqrt{\frac{4\pi e^2 Z^{*2}}{\epsilon_\infty \mu v}} \quad (3.5)$$

is defined in terms of the volume of the primitive cell v , the reduced mass μ of the Cu and Cl atoms, the Born effective charge Z^* , and the high-frequency dielectric constant ϵ_∞ . Three separate linear response calculations [21] determine ω_{TO} , ϵ_∞ and Z^* .

Table 3.3 summarizes our calculated results for Born effective charges and the high-frequency dielectric constant for three different k -point samplings in the irreducible BZ together with the values extracted from experimental measurements as discussed below [134,141]. The LDA cluster calculation of Press and Ellis [142] is also given.

Table 3.3: Calculated Born effective charges and dielectric constant of CuCl.

No. of k -points	ϵ_∞	$Z^*(\text{Cu})$	$Z^*(\text{Cl})$
This Calculation			
2	4.75	0.16	-1.26
10	4.65	1.28	-1.11
28	4.65	0.94	-1.11
Press and Ellis ^A	—	1.30	
Experiment	3.61 ^B	[1.13 _{TO(γ)} , 0.93 _{TO(β)}] ^C	

^A Ref. [142].

^B Ref. [141].

^C Extracted estimates from Ref. [134] and see the discussion in text.

The Born effective charges must obey the acoustic sum rule, which in the case

of CuCl requires the values of $Z^*(\text{Cu})$ and $Z^*(\text{Cl})$ to be equal in magnitude but of opposite sign. As mentioned in Chapter 2, inadequate k -point sampling can result in violations of this rule. As seen in Table 3.3, $Z^*(\text{Cl})$ is converged, but $Z^*(\text{Cu})$ is still not converged at the largest 28 special k -point set that was used. However, based on the acoustic sum rule, we may expect $Z^*(\text{Cu})$ to be 1.11 when it is converged. Using Eq. (3.4) and Eq. (3.5), we took $Z^*(\text{Cl})$ to determine the theoretical frequency of the longitudinal optic mode at Γ given in Table 3.4. The LDA is known to systematically overestimate ϵ_∞ in general [19, 20], and the calculated ϵ_∞ is about 30% too large, consistent with this tendency. Press and Ellis [142] calculated from first principles the piezoelectric properties of copper halides with a localized basis set and an embedded-molecular cluster method. They estimated the Born effective charge in CuCl to be 1.30, but the dielectric constant was not available in their report.

In conventional semiconductors, the experimental effective charges for zincblende diatomic crystals are readily determined from Eq. (3.4) and Eq. (3.5) using the measured values of ϵ_∞ and ω_L and ω_T at the Γ point. The anomalous features of the phonon spectrum of CuCl at the Γ point, however, complicates the analysis here, because four optic modes are observed (see Fig. 3.1). In decreasing frequency, they are [134] $\text{LO}(\gamma)$, $\text{TO}(\gamma)$, $\text{LO}(\beta)$ and $\text{TO}(\beta)$, and their values are given in Table 3.4. The additional $\mathbf{q} = 0$ modes are labeled by Vardeny and Brafman and Livescu [128, 134] as $\beta - \text{TO}(\beta)$ and $\text{LO}(\beta)$, and arise in their model from the off-center cation sublattice. By contrast, Hennion *et al.* [126] invoke the mechanism of strong anharmonic coupling between $\text{TO}(\Gamma)$ mode and a two-phonon continuum to explain the inelastic neutron scattering data of the TO phonons in CuCl at 5 K. They

resolved the anomalous line-shape into two frequencies of 5.11 THz and 4.83 THz. A direct comparison with the anomalous modes at Γ is not possible, since our calculations assume the validity of the harmonic approximation and are performed for distortions about the ideal structure. Table 3.4 indicates that the calculated $\text{TO}(\Gamma)$ frequency falls between the two experimental TO peaks. The theoretical LO frequency is in good agreement with the highest frequency mode in the spectrum at Γ , which lies well above the troublesome frequency range (4.2~5.4 THz) and is identified [121–134] as a normal LO mode. The $\text{LO}(\beta)$ mode is very weak, lying between the two strong TO lines. It is thus unclear how to extract experimental values of Z^* . Without adopting any particular model of the anomalous modes, we estimate “experimental” values Z^* using the experimental frequencies [134] of the zone center optical modes given in Table 3.4 that are determined [134] by a combination of polariton dispersion measurements and fitting to the infrared reflectivity at 2 K. These frequencies are nearly identical to the values measured by Raman scattering at liquid helium temperature [124, 125]. We extract two estimates of the experimental effective charges using the highest frequency mode $\text{LO}(\gamma)$ together with i) the $\text{TO}(\gamma)$ and ii) the $\text{TO}(\beta)$ modes and these are so labeled in Table 3.3. The calculated $Z^*(\text{Cl})$ is close to the extracted experimental effective charge determined by the γ branch modes ($\text{LO}(\gamma)$ and $\text{TO}(\gamma)$). In the off-center model, the γ branch modes arise from Cu ions at the ideal structure sites [134], and the frequency of this mode might be expected to be similar to our calculated value based on the ideal structure.

3.5 Phonon Dispersions

The calculated phonon frequencies along symmetry lines, $\Delta[\xi 0 0]$, $\Sigma[\xi \xi 0]$ and $\Lambda[\xi \xi \xi]$, are shown in Figure 3.2, together with the inelastic neutron scattering experimental data obtained at 4.2 K by Prevot *et al.* [121]. None of the calculated modes are unstable (imaginary frequencies), which shows that the zincblende structure is stable near the Born-Oppenheimer surface and is at least a local energy minimum. Table 3.4 gives the numerical values at high symmetry points. Typical experimental accuracy is about 0.1 THz.

From Figure 3.2 and Table 3.4, we see that the majority of the calculated frequencies fall within the limits of experimental errors. The calculated top two optical phonon dispersion branches in Σ direction have the same symmetry properties. They cannot crossover each other, though they appear to do so in Figure 3.2 visually due to the use of large scale. The minimum distance between these two branches in calculations is indeed small (~ 0.014 THz).

In the past two decades, complete phonon dispersion curves of CuCl have been calculated only with empirical models (see Ref. [143] and references therein). Prevot *et al.* [121] used a shell model to fit the helium-temperature phonon spectra with 14 parameters. Kanellis *et al.* [143] investigated the dynamical properties of copper halides with four different shell models. Patel *et al.* [144] reproduced the phonon dispersion curves with a rigid-ion model using 11 optimized set of force constant parameters. Chatterjee *et al.* [145] tried a unified study of lattice mechanical properties of copper halide crystals with a general expression for the total energy including the dipolar and quadrupolar terms. Together with other studies using various polarizable

models, all these works aim to fitting experimental data, which results in limited predictive power.

Kremer and Weyrich [135, 146] reported full-potential LMTO calculations of TO(Γ) and X-point phonon frequencies of CuCl and other semiconductors. For CuCl, the frequency of TO(Γ) they determined is 4.68 THz, 7% smaller than ours, and their frequencies of X-point are in greater disagreement with experiment. The present calculation is the first self-consistent LDA linear response calculation of the complete phonon dispersions for a semiconductor in which the effects of localized d electrons are fully considered. The agreement between the calculated and the experimental frequencies of optic phonons is generally better than that of the low lying acoustic phonons near the X point, where the calculated frequencies appear to be systematically too high. Giannozzi *et al.* [20] found that using more k -points improved the agreement in the acoustic region for Si and GaAs. We performed calculations for the X-point phonons using 10 k -points. The disagreement is a bit worse in this case with the frequencies of LO(X), TO(X) and LA(X) increasing by 0.02~0.03 THz, and TA(X) by \sim 0.1 THz compared to the 2 k -points calculation.

Carabatos *et al.* [147] reported earlier neutron scattering measurements of phonon spectra at room temperature which differ significantly from the results in Figure 3.2. They find that the optic branches cross each other in the Δ and Λ directions and that the highest acoustic branch disperses higher up, close to the optic modes in Σ direction. These discrepancies are probably due to a combination of sample quality [121] and the fact that the measurements were performed at room temperature. Our calculations are in agreement with the finding of Prevot *et al.* [121]

that there is no crossing of the optic branches in Δ and Λ directions and that there is a large gap between the highest acoustic branch and optic branches in the Σ direction.

Besides the anomalous modes at Γ , the agreement between theory and experiment elsewhere in the Brillouin zone is as good as in less problematic materials such as GaAs. Our theoretical LDA linear response calculations performed for the ideal zincblende structure have not addressed, of course, the source of these observed anomalies. Despite the anomalous properties of CuCl and the presence of large anharmonic interactions, its low-temperature phonon dispersion is accurately predicted by LDA calculations. A similar conclusion was reached in the high- T_c superconductors La_2CuO_4 [148] and $\text{YBa}_2\text{Cu}_3\text{O}_7$ [149, 150] where LDA calculated frequencies are generally in good agreement with experiment despite perhaps even greater anharmonicity.

Table 3.4: Calculated and experimental phonon frequencies for CuCl in THz.

	Calculation (2 k -points)	Experiment	
TO(Γ)	5.05	4.83 ^A 5.11 ^A	4.65 (β) ^B 5.22 (γ) ^B
LO(Γ)	6.21	6.20 \pm 0.16 ^C	5.00 (β) ^B 6.24 (γ) ^B
TA(X)	1.37	1.16 \pm 0.12 ^C	
LA(X)	3.78	3.69 \pm 0.20 ^C	
TO(X)	6.58	6.55 \pm 0.12 ^C	
LO(X)	7.16	7.00 \pm 0.12 ^C	
TA(L)	1.05	1.00 \pm 0.12 ^C	
LA(L)	3.47	3.40 \pm 0.14 ^C	
TO(L)	5.78	5.70 \pm 0.10 ^C	
LO(L)	7.47	7.34 \pm 0.16 ^C	
$q=[\frac{1}{4}00]\frac{2\pi}{a}$			
TA	0.80	0.74 ^D	
LA	1.66	1.8 ^D	
TO	5.32	5.21 ^D	
LO	6.38	6.43 ^D	
$q=[\frac{1}{4}\frac{1}{4}0]\frac{2\pi}{a}$			
	0.64	0.66 ^D	
	1.10	1.05 ^D	
	2.29	2.22 ^D	
	5.24	5.21 ^D	
	5.54	5.47 ^D	
	6.56	6.64 ^D	

^A Frequencies resolved from neutron scattering data at 5 K by Ref. [126].

^B From Ref. [134].

^C Inelastic neutron scattering measurements at 4.2 K from Ref. [121].

^D Interpolated from Ref. [121].

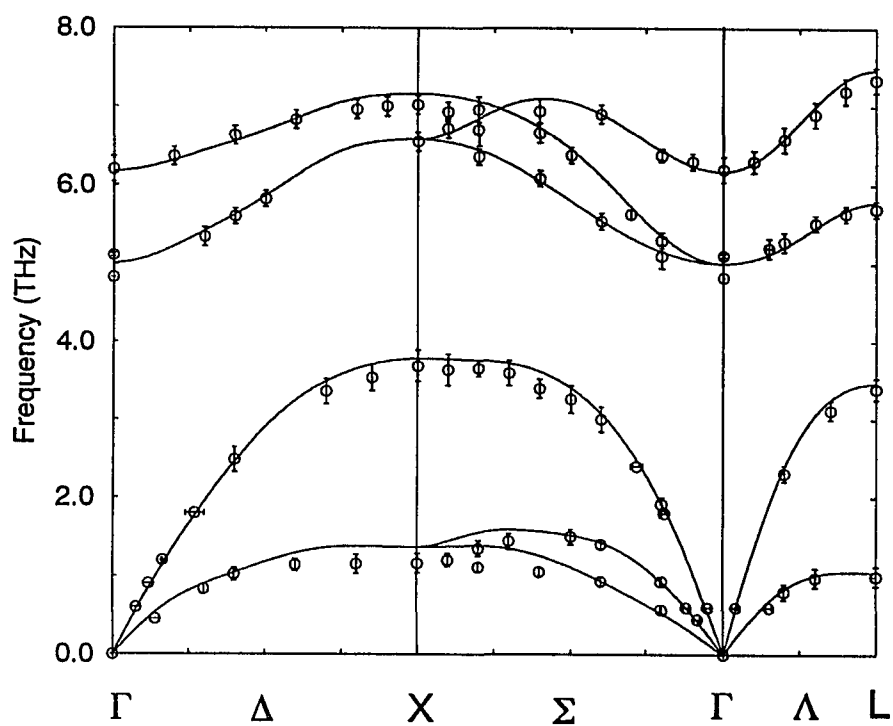


Figure 3.2: Phonon dispersion curves of CuCl. The solid line is given by the theoretical calculations. Open circles are neutron scattering measurements at 4.2 K (Ref. [121]).

Chapter 4

Lattice Dynamics of SiC Under Pressure

4.1 Introduction

Recently, Liu and Vohra [151] presented intriguing evidence regarding the pressure dependence of the Born effective charge in $6H$ -SiC. These authors found that the effective charge increased initially with increasing pressure, reaching a maximum at about 0.4 Mbar (40 GPa). Further increasing the pressure, however, resulted in a decrease in the magnitude of the effective charge. Because of its great potential in electronic device applications, especially in harsh environments such as high temperature, corrosive atmosphere and irradiation etc., it is important to accurately characterize the properties of this unusual material. SiC is observed now to crystallize in more than two hundred polytypes, corresponding to different stacking sequences of Si-C bilayers in the cubic $[1\ 1\ 1]$ direction. [152] Polytypes with cubic, hexagonal and

rhombohedral unit cells are usually designated $3C$, nH and nR respectively, where n is the number of layers, with the $3C$ structure corresponding to the zincblende structure. For instance, viewed along the cubic $[1\ 1\ 1]$ direction, the stacking sequences of Si-C layers are ABC for $3C$ -SiC, AB for $2H$ -SiC and $ABCACB$ for $6H$ -SiC. The repeat distances in the stacking direction can be as large as $1200\ \text{\AA}$ [153]. The stacking fault energy in these polytypes is quite small. The underlying mechanism responsible for so many polytypes and such long repeat unit cell is still an active subject under intensive research. One prevailing and conventional view [154] is that such long range crystallographic order does not originate from a long range force, but is induced by the presence of spiral steps due to dislocations in the growth nucleus. Several growth mechanisms have been proposed recently for the origin of polytypes [155–157]. However Winkler *et al.* [158] proposed the polytypism may be stabilized by the phonon contribution to the free energy. Cheng *et al.* [159–161] demonstrated the long-ranged interatomic interactions arising from phonons tend to stabilize the polytypes as equilibrium structures. It is evident that an accurate understanding of lattice dynamical properties of SiC is useful for a correct explanation of its various interesting properties including mechanical, thermal, and structural ones.

The different polytypes have very similar properties, since differences in local atomic coordination first appear in the second neighbor shell. The experimental equation of state for different polytypes are very similar. [162,163] Phonon dispersion along the stacking direction are considered universal for different prototypes and this universality has been used to map out the phonon dispersion in this direction from Raman scattering measurements. [141,164] The crystal structures of polytypes have

been determined by minimizing the LDA total energy and the internal parameters are found actually very close to values of ideal structures. [35, 165–167] Indeed, a recent self-consistent study of *3C*, *2H* and *4H* SiC by Karch *et al.* [35] found remarkably small differences in the calculated phonon frequencies along the stacking direction. We report here self-consistent linear response calculations of the volume dependence of the Born effective charge, dielectric constant and lattice dynamics of cubic SiC. In view of the great similarity of the various polytypes, our computations were carried out only for *3C*-SiC. We find that the Born effective charge increases nearly linearly as the volume decreases. This is in sharp contrast with the above-mentioned turn-over behavior reported recently for *6H*-SiC. The likely reason for this discrepancy will be discussed in light of the calculated results.

4.2 Computational Details

The calculations were performed using the LAPW linear response method which facilitates the treatment of localized valence states, as are found in first-row elements such as carbon. We employ a hard Kerker [93] type pseudopotential to dispense with the need to treat the chemically inert localized inner core orbitals. The muffin-tin radii for Si and C are 1.79 a.u. and 1.50 a.u. respectively. Table 4.1 presents the test results regarding the convergence to the kinetic energy cutoff (KE) and special k -point set sampling for BZ integration in the frozen phonon calculations at zone center Γ point. We also checked the dependence of phonon frequencies on the choices of different exchange-correlation functional forms such as Wigner interpolation formula [56] and Hedin and Lundqvist formula [60]. Note all data in Table 4.1 were

obtained at experimental lattice constant. The procedure of frozen phonon calculations has been discussed in the previous Chapter on CuCl. The notation $f_{\Delta E}$ denotes the phonon frequencies calculated from energy difference between the distorted structure and the ideal zincblende cubic structure, while f_F denotes calculated frequencies from the forces acting on atoms under distortions. As expected, the values of $f_{\Delta E}$ and f_F are essentially the same numerically in each case of Table 4.1. Table 4.1 shows $KE = 28.5$ Ry gives well converged results, since the difference from $KE = 36.0$ Ry is negligible. The use of (4 4 4) k -point set already achieved phonon frequency convergence better than half percent, however, we chose a larger (8 8 8) k -point set for the linear response calculations of phonon modes with phonon wavevectors on a uniform (4 4 4) mesh. Table 4.1 also indicates that phonon frequencies calculated with different exchange-correlation functional forms display little differences. Wigner interpolation formula was used for the following calculations unless otherwise stated.

Table 4.1: Test frozen-phonon calculations of frequencies of TO(Γ) mode of 3C-SiC. KE is the kinetic energy cutoff.

	$f_{\Delta E}$ (THz)	f_F (THz)
(4 4 4) k -point set KE= 28.5 Ry XC-Wigner	23.356	23.397
(4 4 4) k -point set KE= 36.0 Ry XC-Wigner	23.360	23.399
(4 4 4) k -point set KE= 28.5 Ry XC-HL	23.262	23.304
(8 8 8) k -point set KE= 28.5 Ry XC-Wigner	23.258	23.300
(12 12 12) k -point set KE= 28.5 Ry XC-Wigner	23.220	23.227

4.3 Ground State Properties

LAPW total energy calculations were performed to determine the theoretical lattice constant a_0 , bulk modulus B_0 and bulk modulus pressure derivative B'_0 for 3C-SiC by fitting Murnaghan's equation [139]. Earlier experimental and theoretical studies suggest that the volume-pressure relations for different polytypes are similar, due to the rigidity of the nearest-neighbor coordination. For instance, the equation-of-state data for the two polytypes 3C-SiC and 6H-SiC have been found to be essentially the same up to the transition pressure of 3C-SiC. [163] Theoretical calculations [35] also give very small difference in the bulk modulus (less than 1%) between the 3C, 2H and 4H polytypes. The calculated pressure derivative of the bulk modulus for these polytypes are different by only 7% [35].

Our results for 3C-SiC are presented in Table 4.2 and compared with other calculations and experiment for 3C and other polytypes. Our results agree well with that of other calculations given in the table. Slight differences may be due to the use of different forms of the exchange-correlation potential. There is nearly perfect agreement between the present calculations and those of Chang and Cohen [168], both using the Wigner exchange-correlation potential. Karch *et al.* [35] used the Ceperly and Alder exchange-correlation formula [57, 58] as parametrized by Perdew and Zunger. [59] Lambrecht *et al.* [169] used an LMTO basis set and the von Barth-Hedin parametrization of the exchange-correlation energy. [61] As also seen in other systems [77], the Wigner form tends to yield slightly larger equilibrium lattice constants than other forms, and as expected the bulk modulus is accordingly slightly smaller.

A significant number of high-pressure experiments have been carried out on various polytypes of SiC. The experiments generally showed that there is little difference between the equation of states for different polytypes. Unfortunately, there are large discrepancies between the results of different experimental groups for the bulk modulus and its pressure derivative. Most experiments give bulk modulus and its pressure derivative around 2.25 Mbar and 4.0 respectively. However, Yoshida *et al.* [163] recently reported quite large bulk modulus B_0 (2.60 ± 0.09 Mar) and quite small bulk modulus pressure derivative B'_0 (2.9 ± 0.3) compared to other groups' results. They ascribed this discrepancy to the higher pressure range (up to 0.95 Mbar) they applied to the materials. Analysis of our calculated results does not bear out this explanation. Using our calculated total-energy at various volumes, we can fit to the Murnaghan equation of state [139] for pressures up to about 0.8 Mbar. We find only small differences (on the order of 1% in both B_0 and B'_0) compared to fitting a smaller pressure range. The explanation is also inconsistent with the experiments of Aleksandrov *et al.* [174] and Goncharov *et al.* [162], which were carried out to 0.425 Mbar and 0.45 Mbar respectively, but obtained a smaller bulk modulus as compared with that of Strösser *et al.* [175], which went up to only 0.25 Mbar. Based on the results of all existing well-converged theoretical calculations, it seems reasonable to suggest that the lower range of the experimental bulk modulus is more likely to be correct.

We have also determined the volume dependence of the total energy for rocksalt structure SiC. Figure 4.1 shows the total energy curves vs. variations of volume for both zincblende phase and rocksalt phase, in which the common tangent line of the

two curves indicates the phase transition. Figure 4.1 shows the zincblende structure is stable at ambient pressure and the difference in cohesive energy per primitive unit cell between two phases is about 107 mRy. The dependence of Gibbs free energy for two phases on pressure is plotted in Figure 4.2. The crossover point of Gibbs energy curves for two phases gives the theoretical transition pressure. Table 4.3 compares the transition parameters in the present calculations and other reports as well as experiment.

Our calculations indicate that SiC transforms from zincblende phase to rocksalt phase at around 0.65 Mbar, the volume of zincblende phase at transition is about 82% of its equilibrium volume at ambient pressure, and the volume reduction accompanied by the transition is around 20%. These results are in good agreement with other LDA calculations and the percentage of volume reduction around transition pressure is close to experiment. However, the transition pressure and the volume of 3C phase before transition differ considerably from the experimental data. When comparing the theoretical predictions of transition pressure and volume with the experiment, one should bear in mind that the experimental transition pressures obtained in diamond-anvil are for the forward transition (from zincblende phase to rocksalt phase), where an excess pressure beyond the equilibrium value appears and is included in measurements [163, 178], while the theoretical predictions are made for thermodynamic equilibrium. Unfortunately, Yoshida *et al.* [163] did not give an estimate of magnitude of the excess pressure in their measurements.

Table 4.2: Equilibrium state properties of 3C-SiC. The equilibrium lattice constant, bulk modulus and its pressure derivative are represented by a_0 , B_0 , and B'_0 , respectively.

	a (Å)	B_0 (Mbar)	B'_0	Pressure range (Mbar)
Chang <i>et al.</i> ^a	4.361	2.12	3.7	
Lambrecht <i>et al.</i> ^b	4.315	2.23	3.8	
Karch <i>et al.</i> ^c	4.345	2.22	3.88	
Present	4.360	2.10	3.71	
Experiment 3C	4.360 ^d			
		2.24 ^e		
		2.234 ^f		
		2.25 ^g		
		2.27 ± 0.03 ^h	4.1 ± 0.10 ^h	0.425
		2.48 ± 0.09 ⁱ	3.7 ± 0.3 ⁱ	0.25
6H,15R		2.24 ± 0.03 ^j	4.3 ± 0.3 ^j	0.45
3C,6H		2.60 ± 0.09 ^k	2.9 ± 0.3 ^k	0.95

^a Ref. [168].

^b Ref. [169].

^c Ref. [35].

^d Ref. [170].

^e Yean *et al.* [171].

^f Schreiber *et al.* [172].

^g R. D. Carnahan [173].

^h Aleksandrov *et al.* [174].

ⁱ Strosser *et al.* [175].

^j Goncharov *et al.* [162].

^k Yoshida *et al.* [163].

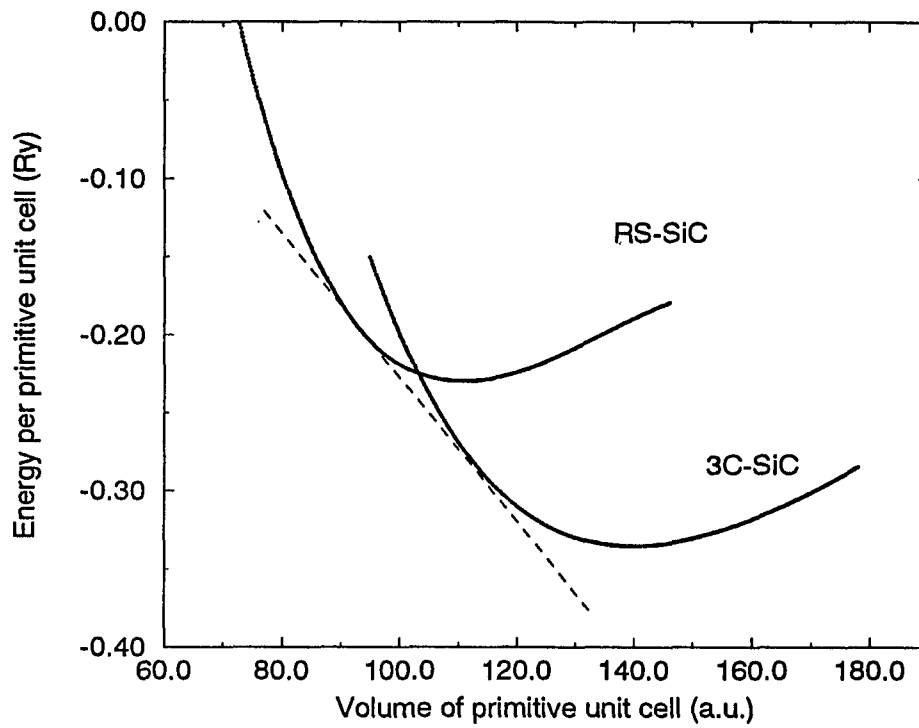


Figure 4.1: Calculated total energy vs. variations of volume per primitive unit cell for zincblende and rocksalt phases. Note the energy values have been shifted by a constant. The dashed line is the common tangent line of the two curves, which indicates the phase transition. For rocksalt SiC, the lattice constant, bulk modulus and its pressure derivative are determined to be 4.04 Å, 2.21 Mbar and 4.41, respectively.

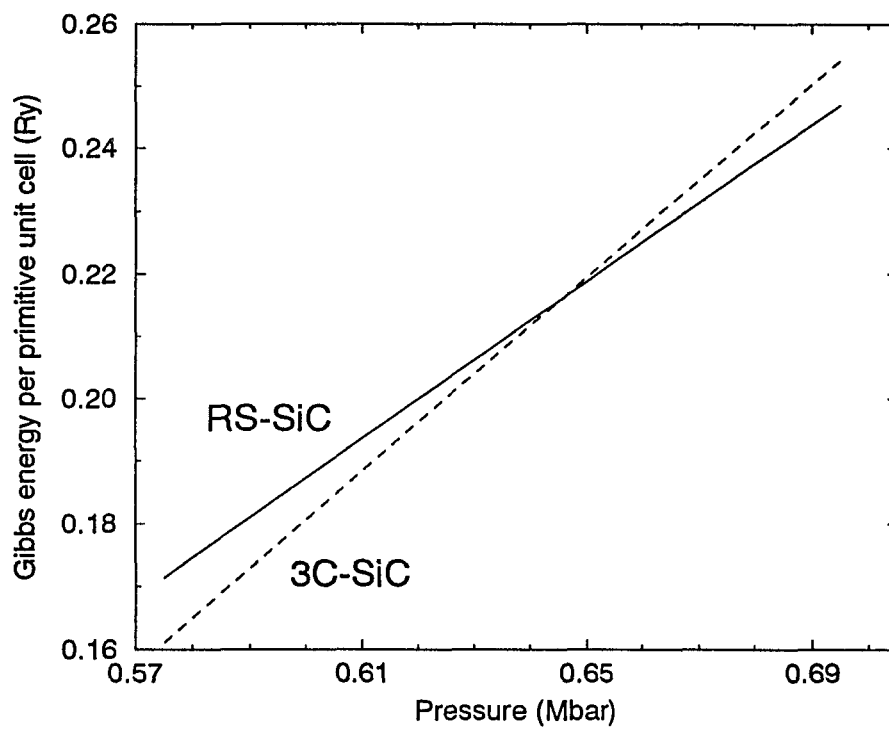


Figure 4.2: Calculated Gibbs free energy under pressure for zincblende and rocksalt phases. The solid line is for rocksalt SiC and the dashed line for zincblende SiC. Note the energy values have been shifted by a constant. The crossover of two curves gives phase transition pressure.

Table 4.3: Transitional parameters from zincblende structure to rocksalt structure for SiC. V_t is the volume of zincblende (3C) phase at transition, and V_0 is the volume at ambient pressure. $\Delta V/V_0$ denotes the percentage of volume reduction when the transition occurs.

	Pressure (Mbar)	V_t/V_0	$\Delta V/V_0$ (%)
Calculations			
Present	0.65	0.817	20.2
Chang <i>et al.</i> ^a	0.66	0.81	18.5
Cheong <i>et al.</i> ^b	0.60	0.825	
Christensen <i>et al.</i> ^c	0.59	0.84 ^d	19 ^d
Experiment ^e	1.00	0.757	20.3

^a Ref. [168]

^b Ref. [176]

^c Ref. [177]

^d Quoted from Ref. [163], in which the authors derived these numbers from Fig.12 of Ref. [177]

^e Yoshida *et al.* [163]

4.4 Z^* , ϵ_∞ , Phonon Dispersions and Elastic Constants

The Born effective charges Z^* and ϵ_∞ are calculated at small \mathbf{q} wavevector $0.01(1\ 1\ 1)\frac{2\pi}{a}$, where a is lattice constant. Table 4.4 presents our results at experimental equilibrium volume. The Born effective charges $Z^*(\text{Si})$ and $Z^*(\text{C})$ have converged better than one percent when 28 special k -point set in irreducible BZ, which correspond to (12 12 12) uniform k -point mesh, is used to sample the BZ integration. Theoretically, $Z^*(\text{Si})$ and $Z^*(\text{C})$ have the same magnitude and opposite signs, which is required by the acoustic sum rule. The slight violation to this rule here arises from the finite k -point sampling. However, good results can be obtained with few k points by taking the average of the magnitudes of $Z^*(\text{Si})$ and $Z^*(\text{C})$. [20] The averaging is also helpful to reduce the effect of a small but finite wavevector. We have used a slightly larger wavevector $\mathbf{q}=0.02(1\ 1\ 1)\frac{2\pi}{a}$ to check the behavior of this effect and observed that the splitting between the magnitudes of $Z^*(\text{Si})$ and $Z^*(\text{C})$ increases slightly as \mathbf{q} deviates further from zero, i.e. $Z^*(\text{Si})$ becomes larger while $Z^*(\text{C})$ becomes more negative. Of course, the effect from the use of small wavevector can be reduced by simply choosing a smaller wavevector in computation. Table 4.4 shows our calculations give Born effective charge in excellent agreement with experiment but the static dielectric constant ϵ_∞ is about 7% too large. Our results are consistent with the linear response calculations by Karch *et al.* with plane wave basis set [35].

Table 4.5 compares our calculated phonon frequencies with those of Karch *et al.* [35] and with experiment. Our calculated frequencies are systematically about a

Table 4.4: Calculated Born effective charges Z^* and ϵ_∞ at the equilibrium state of 3C-SiC.

	$Z^*(\text{Si})$	$Z^*(\text{C})$	$\frac{ Z^*(\text{Si}) + Z^*(\text{C}) }{2}$	ϵ_∞
Present				
2 k -point set	2.428	-3.392	2.910	9.426
10 k -point set	2.701	-2.716	2.708	7.137
28 k -point set	2.709	-2.693	2.701	7.005
Karch <i>et al.</i> ^a			2.72	6.97
Experiment			2.697 ^b	6.52 ^c

^a Ref. [35].

^b Ref. [179].

^c Ref. [170].

couple of percent smaller than those of Ref. [35]. This is perhaps due in part to the difference in the equilibrium volume used in the two calculations. They used a smaller LDA equilibrium volume which is expected to yield stiffer vibrational frequencies.

The phonon dispersions in three high symmetry directions, $\Delta[\xi 0 0]$, $\Sigma[\xi \xi 0]$ and $\Lambda[\xi \xi \xi]$, are plotted in Figure 4.3. For points along the $\Lambda[\xi \xi \xi]$ direction, we obtained the dynamical matrices by i) the long-ranged Coulomb interaction that can be taken into account analytically with Ewald technique [107, 108], and ii) the short-ranged real space force constants obtained from dynamical matrices of (4 4 4) phonon wavevector mesh. But in $\Delta[\xi 0 0]$ and $\Sigma[\xi \xi 0]$ directions, we have calculated the dynamical matrices at additional points, which correspond to (8 8 8) face center cubic (fcc) mesh, and used the one-dimensional interplanar force constants techniques. [181] The (8 8 8) mesh turns out to improve the dispersion in the acoustic region.

Table 4.5: Theoretical and experimental phonon frequencies (cm^{-1}) in 3C-SiC.

Modes	Present	Karch <i>et al.</i> ^a	Experiment ^b
TO(Γ)	774	783	796
LO(Γ)	945	956	972
TA(X)	361	366	373
LA(X)	622	629	640
TO(X)	741	755	761
LO(X)	807	829	829
TA(L)	257	261	266
LA(L)	601	610	610
TO(L)	747	766	766
LO(L)	817	838	838

^a Karch *et al.* Ref. [35].

^b Ref. [164,180].

No neutron scattering data for zincblende SiC is available because it is difficult to grow 3C-SiC single crystal to a size big enough for such measurement. The filled squares in Figure 4.3 are experimental phonon frequency data from Raman scattering measurement. The experimental data on the BZ boundary (X and L) are obtained from second-order Raman scattering [180]. Others are first-order Raman data from hexagonal and rhombohedral polytypes, which have been unfolded into larger 3C-SiC Brillouin zone. [164] The excellent agreement between theory and experiment shows that the different stacking sequences have little influence on the vibrational properties. As mentioned, the calculated phonon frequencies of Karch *et al.* [35] on 2H- and 4H-SiC directly support this conclusion. As shown in Figure 4.3 the transverse acoustic phonon dispersion near the BZ boundary of SiC does not show the flatness that

appears in CuCl and other typical tetrahedral semiconductors. The strong chemical bond between Si and C leads to unusually high optical phonon frequencies as well as high acoustic phonon frequencies near boundary. Compared with GaAs, which is a typical semiconductor with the same structure, the phonon frequencies of TO(Γ) and LO(Γ) in SiC are about 2 or 3 times higher. This is consistent with the macroscopic properties of SiC such as outstanding mechanical hardness and extreme stability under high temperature. The LAPW theoretical LO-TO splitting at zone center is 171 cm^{-1} , which is much larger than that in GaAs (22 cm^{-1}) [20]. There are several reasons for this: i) the Born effective charge in SiC is 30% bigger than that in GaAs ($Z^*=2.07$ [20]), ii) the static dielectric constant of SiC is only 60% of GaAs ($\epsilon_\infty=10.9$ [20]), iii) the volume of unit cell of SiC is only 46% of GaAs ($a=5.65 \text{ \AA}$) [20], and, most importantly, iv) the reduced mass of Si and C is merely 8.4131 a.u. , much smaller than the reduced mass of Ga and As, 36.113 a.u.

As by-products, the elastic constants can be extracted from the calculated acoustic phonon dispersions. For cubic structure, the elastic constants C_{44} and C_{11} are simply related to the velocities of the transverse and longitudinal plane waves in $[1\ 0\ 0]$ direction as follows [182]:

$$v_T[100] = \sqrt{\frac{C_{44}}{\rho}}, \quad (4.1)$$

$$v_L[100] = \sqrt{\frac{C_{11}}{\rho}}, \quad (4.2)$$

where ρ is the density of mass of SiC. The velocities of $v_T[100]$ and $v_L[100]$ can be obtained from the slopes of acoustic transverse and longitudinal phonon dispersions

at zone center in $[1\ 0\ 0]$ direction, since

$$v_j[100] = \frac{\partial \omega_j}{\partial k} \quad (4.3)$$

where ω_j is the angular frequency of j -th branch phonon and k is the magnitude of the corresponding wavevector. Similarly, the elastic constant C_{12} can be obtained from the relationship [182]

$$v_{T_1}[110] = \sqrt{\frac{C_{11} - C_{12}}{2\rho}}, \quad (4.4)$$

where v_{T_1} is the velocity of the transverse wave with atomic displacement along $[1\ -1\ 0]$, which corresponds to the lowest acoustic branch in Σ direction, i.e. $[1\ 1\ 0]$. When these elastic constants are already available, the bulk modulus B_0 is accessible by [183]

$$B_0 = \frac{C_{11} + 2C_{12}}{3}. \quad (4.5)$$

The transverse sound velocity shows directional dependence in $3C$ -SiC, demonstrating that it is not an isotropic material. The fact that the interatomic forces in $3C$ -SiC are highly noncentral suggests the elastic constants do not satisfy the Cauchy relation (i.e. $C_{12} = C_{44}$).

Table 4.6 presents the elastic constants and the bulk modulus extracted from the above procedure by us and calculated by other groups with various methods. Our results agree with experiment within a few percent and are systematically slightly smaller than the calculations by Karch *et al.* [35] due again in part to the use of slightly different lattice constants. The bulk modulus B_0 found from elastic constants is consistent with our result from total energy calculations in previous section.

Table 4.6: Elastic constants and bulk modulus (in units of Mbar) of 3C-SiC.

	C_{44}	C_{11}	C_{12}	B
Present	2.41	3.84	1.32	2.16
Karch <i>et al.</i> ^a	2.53	3.90	1.34	2.19
Lambrecht <i>et al.</i> ^b	2.87	4.20	1.26	2.24
Expt. ^c	2.56	3.90	1.42	2.25

^a Karch *et al.* Ref. [35].

^b Lambrecht *et al.* Ref. [169]

^c The experimental data are derived by Lambrecht *et al.* [169] from the sound velocities of Feldman *et al.* [164].

Owing to the lack of sufficient experimental data to fit, the phonon dispersions given by empirical models achieved limited success. [184–186] Cheng *et al.* incorporated the results from LDA density functional calculations, i.e. the phonon frequencies and eigenvectors at X and L points, into a shell-model in fitting the available measured phonon frequencies. [54] Using the shell-model force constants of Cheng *et al.* [54], Windl *et al.* found the dispersion curves along the main symmetry directions are fairly reproduced, but the overtone density of states differ significantly from that of the full *ab initio* calculations and the model fails to describe the second-order scattering. However, the *ab initio* calculations are demonstrated to agree well with the experimental scattering intensities. [187]

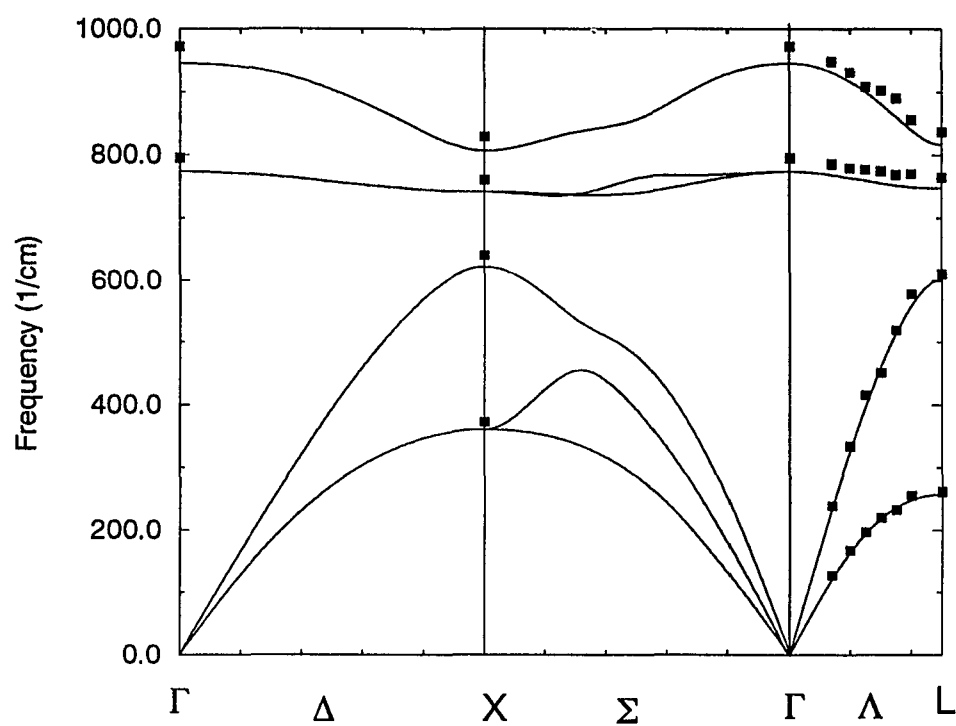


Figure 4.3: Phonon dispersion curves of 3C-SiC. Calculated phonon frequencies of 3C-SiC at experimental lattice constant (solid lines). The filled square symbols are experimental data (see text).

4.5 Properties Under Pressure

We now turn to the pressure or volume dependence of the calculated properties.

Grüneisen's parameter, which is defined as

$$\gamma = -\frac{V}{\omega} \frac{\partial \omega}{\partial V}, \quad (4.6)$$

is a quantity to describe the dependence of phonon mode frequency on pressure. Table 4.7 presents calculated Grüneisen's parameters at the Γ , X and L points in the BZ. Our calculations also appear to be in good agreement with Karch *et al.* [35] as presented in their Fig. 9. In the text of that paper, they give the numerical value of one Grüneisen's parameter, $\gamma_{TA}(X) = 0.13$, which is in very good agreement with our value of 0.12. The experimental results of Olego *et al.* [179,180] and of Aleksandrov *et al.* [174] are presented for comparison. In the former work, the Grüneisen's parameters were calculated from their experimental volume dependence using a bulk modulus of 3.219 Mbar (the average of Si and diamond C [179]). This value is likely to be too large, as discussed above. The experimental data from Olego *et al.* given in Table 4.7 are converted from their results, assuming our theoretical bulk modulus. While a generally good agreement is seen between our calculations and experiment, a significant discrepancy exists for the LA mode at the L -point. The experiment of Olego *et al.* gave a negative value, in contrast with our theoretical prediction and that of Karch *et al.*

Interested by the negative Grüneisen's parameter of TA(L) mode at ambient pressure, we calculated the phonon spectra of L point at a smaller lattice constant 4.16 Å, which corresponds to pressure around 0.38 Mbar. The frequencies for TA, LA, TO and LO modes are 249, 675, 890, and 959 cm⁻¹, respectively. Compared to

Table 4.7: Grüneisen's parameters of phonon modes in 3C-SiC.

	Present	Other Cal.	Expt.	
TO(Γ)	1.07	1.03 ^c	1.02 ^a	1.102 ^b
LO(Γ)	1.02		1.01 ^a	1.091 ^b
TA(X)	0.12	0.13 ^d		
LA(X)	0.82			
TO(X)	1.46		1.30 ^a	
LO(X)	1.16			
TA(L)	-0.13		-0.28 ^a	
LA(L)	0.90	0.94 ^d	-0.11 ^a	
TO(L)	1.31		1.24 ^a	
LO(L)	1.15		1.30 ^a	

^a Converted from the experimental data of Olego *et al.* [179,180] using our theoretical equation of state.

^b Aleksandrov *et al.* [174].

^c Cheong *et al.* [176].

^d Estimated from Fig. 9 of Karch *et al.* [35]

the equilibrium volume case, the magnitude of the decrease of TA(L) mode frequency is just 8 cm⁻¹, which is too small to support the speculation by Goncharov *et al.* [162] that the softening of TA mode could associate with a structural instability.

Table 4.8 presents our calculated volume dependence of Born effective charge Z^* , dielectric constant ϵ_∞ , frequencies of LO and TO modes and LO-TO splitting at Γ point in 3C-SiC. The frequencies ω_{LO} are obtained from the calculated ω_{TO} , ϵ_∞ , Z^* , and the volume of the primitive unit cell v , using Eq. (3.5). ω_{LO} can also be obtained directly from linear response calculations for the full dynamical matrix at a small wavevector, just as what we have done at usual phonon wavevectors. Two

Table 4.8: The calculated Born effective charge Z^* , dielectric constant ϵ_∞ , and LO-TO splitting in 3C-SiC under pressure. The lattice parameter a is in atomic unit (*a.u.*) and frequencies ω are in cm^{-1} .

a	Z^*	ϵ_∞	ω_{TO}	ω_{LO}	$\omega_{LO} - \omega_{TO}$
8.339	2.676	7.111	744	910	166
8.239	2.701	7.005	775	945	171
8.157	2.721	6.927	800	975	175
8.069	2.744	6.852	831	1010	179
8.000	2.761	6.800	855	1038	183
7.864	2.793	6.707	905	1094	189
7.610	2.850	6.575	1015	1214	199

methods have been tested to give results in good agreement as expected.

Table 4.9 compares the fitted equations of zone center phonon frequencies of SiC under pressure in quadratic form, $\omega = c_0 + c_1P + c_2P^2$. The calculated pressure as a function of volume was determined by fitting the volume dependence of the total energy to the Murnaghan equation of state [188]. As mentioned above, our frequencies c_0 at ambient pressure are a few percent smaller than experiment. For the low pressure range ($P \sim 0.25$ Mbar, i.e. 25 GPa) fitting, our first order pressure term coefficients c_1 are close to the experiment, while the second order coefficients exhibit some difference. Note the experimental c_2 have larger relative uncertainty and the second order terms c_2P^2 give only small contributions to ω . When we fit to higher pressure range (up to $P \sim 0.95$ Mbar, i.e. 95 GPa), the coefficients c_1 change up to 10%, while c_2 changes drastically. Table 4.9 also presents the corresponding fitting equations for 6H-SiC up to 0.95 Mbar given by Liu and Vohra [151]. The coefficients c_1 in their quadratic fits appear different from our results for 3C-SiC by

up to 25%, but c_2 are pretty close. The specific analysis of fitting quality of ω_{TO} and ω_{LO} is unavailable in Ref. [151]. Nevertheless, Fig. 2 in Ref. [151] indicates data for LO-TO splitting are scattered around with uncertainty up to 8 cm^{-1} , or 4%. We will return to this crucial point below.

Fig. 4.4 compares the pressure dependence of our results for 3C-SiC with the results of Liu and Vohra [151] for 6H-SiC. The calculated Born effective charge is seen to monotonically increase with increasing pressure, and there is no evidence of a relative maximum as is in the results of Ref. [151]. There are several possible sources for the apparently large discrepancy between theory and experiment in Figure 4.4. Experimentally, the pressure dependence of the Born effective charge was obtained from the measured LO-TO splitting via Eq. (3.5). The LO-TO splitting is the quantity that is directly measured. In order to extract the pressure dependence of the effective charge from the measured LO-TO splitting, two additional pieces of information were required: i) an estimate of the volume dependence of ϵ_∞ , and ii) the use of an equation of state to derive the volume from the measured pressure. By contrast, in the theoretical calculations, the volume dependence of Z^* , ϵ_∞ , and ω_{TO} are determined *independently*.

The volume dependence of ϵ_∞ has apparently never been measured for SiC. Liu and Vohra followed Olego *et al.* [179] in using the following expression,

$$\frac{\partial \ln \epsilon_\infty}{\partial \ln V} = r, \quad (4.7)$$

with $r = 0.6$ for this range of pressures, citing earlier work on both Si and C that report this dependence. We summarize the available data of volume dependence of ϵ_∞ of Si and diamond C in Table 4.10. Some data are converted from their pressure

Table 4.9: Fitted equations of ω_{TO} and ω_{LO} for SiC under pressure. Frequencies are in cm^{-1} and pressure P in GPa. The digits in the brackets denote the tolerance in experimental fits. Note: ^aRef. [176], ^b Ref. [179], ^cRef. [151].

	ω_{TO}	ω_{LO}
3C-SiC Fitted up to ~ 25 GPa Present	$774.2+4.08 P - 0.0177 P^2$	$946.5+4.88 P - 0.051 P^2$
Cheong <i>et al.</i> ^a Expt. ^b	$766.4+4.13 P - 0.0234 P^2$ $796.2(3)+3.88(8)P -0.022(4) P^2$	— $972.7(3)+4.75(9)P-0.025(4) P^2$
3C-SiC Fitted up to ~ 95 GPa Present	$774.1+3.92 P-0.0114 P^2$	$944.3+4.37 P -0.0127 P^2$
6H-SiC Fitted up to ~ 95 GPa Expt. ^c	$789.2+3.11P -0.009 P^2$	$970.1+3.83 P-0.013 P^2$

dependence using

$$\frac{\partial \ln \epsilon_{\infty}}{\partial \ln V} = -B_0 \frac{\partial \ln \epsilon_{\infty}}{\partial P}, \quad (4.8)$$

where the bulk modulus B_0 is 0.99 Mbar for Si and 4.52 for diamond C [170]. There is considerable spread in the experimental data in Table 4.10. Goni *et al.* [189] have reviewed the volume dependence of the refractive index of Ge and GaAs. Their Table II shows large differences between various measurements of the volume derivative of ϵ_{∞} in Eq. (4.7). Thus, the use of the scaling relation, Eq. (4.7), and the particular value $r = 0.6$ must be regarded as a weak link in the experimental analysis of the volume dependence of the Born effective charge in SiC. Furthermore, our calculations indicate that this scaling relation is not a particularly good fit to the actual volume dependence. This is indicated in Fig.4.5, which compares several choices of scaling relation, Eq. (4.7), with the calculated volume dependence of ϵ_{∞} . Actually the value of r in Eq. (4.7) is volume-dependent. We extracted r at low pressure from the calculated $\epsilon_{\infty}(V)$ curve and found it to be 0.39. As shown in Figure 4.5, $r = 0.39$ gives the best fit at low pressure (or small volume compression), but the fit gets worse when the pressure goes higher.

Finally, Liu and Vohra used the Birch-Murnaghan equation of state, using values of the bulk modulus, $B = 2.60$ Mbar, and its pressure derivative, $B' = 2.9$, given by Yoshida *et al.* [163]. Their bulk modulus is 10 - 20 % larger than other measured values, and their pressure derivative is about 20 - 35% smaller.

The LO-TO splitting measured by Liu and Vohra [151] for 6H-SiC changes 15% when pressure is applied from zero to 0.95 Mbar. But the change in Born effective charge Z^* is only 1.5 %, one order of magnitude smaller in the same pressure range.

Table 4.10: Volume dependence of the dielectric constant, $r = \partial \ln \epsilon_\infty / \partial \ln V$, of Si and diamond C from literature and the present work.

	Si	C (diamond)
Expt.	$0.28 \pm 12\%a$	$0.48 \pm 8\%e,f$
	$0.23 \pm 5\%b$	
	$0.6 \pm 67\%c$	$0.6g$
	$0.4 \pm 25\%c$	
LDA Cal.		
Levine <i>et al.</i> ^d	0.41	
Present	0.42	0.27

^aRef. [190].

^b Ref. [191, 192].

^cRef. [193].

^dRef. [194].

^eRef. [195].

^f Ref. [196].

^g Quoted by Olego *et al.* [179] ($B_0=5.77$ Mbar was used).

Thus, the LO-TO splitting is greatly dominated by the pressure dependence of ϵ_∞ and volume. This is equivalent to stating that the saturation phenomenon of the Born effective charge reported by Ref. [151], in which the change of Z^* is actually in the same order as the uncertainty of experimental phonon frequencies, can be easily overwhelmed by the errors in the estimate of parameters ϵ_∞ and volume under pressure.

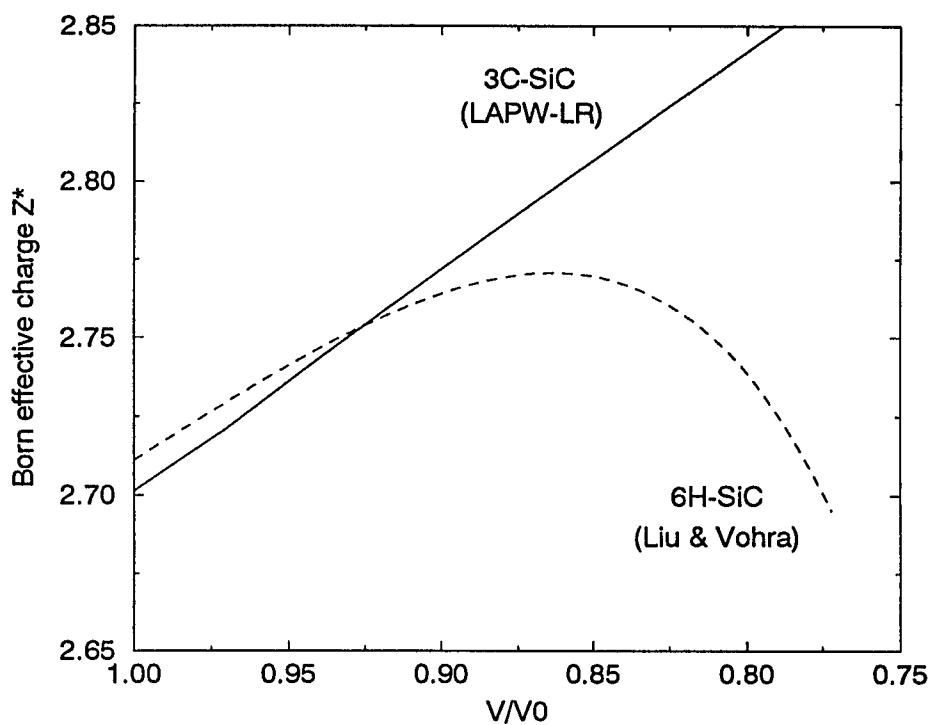


Figure 4.4: The volume dependence of Born effective charge calculated for 3C-SiC (solid line). The dashed line is the Born effective charge reported by Liu and Vohra [151] for 6H-SiC. Note V_0 is the volume at ambient pressure.

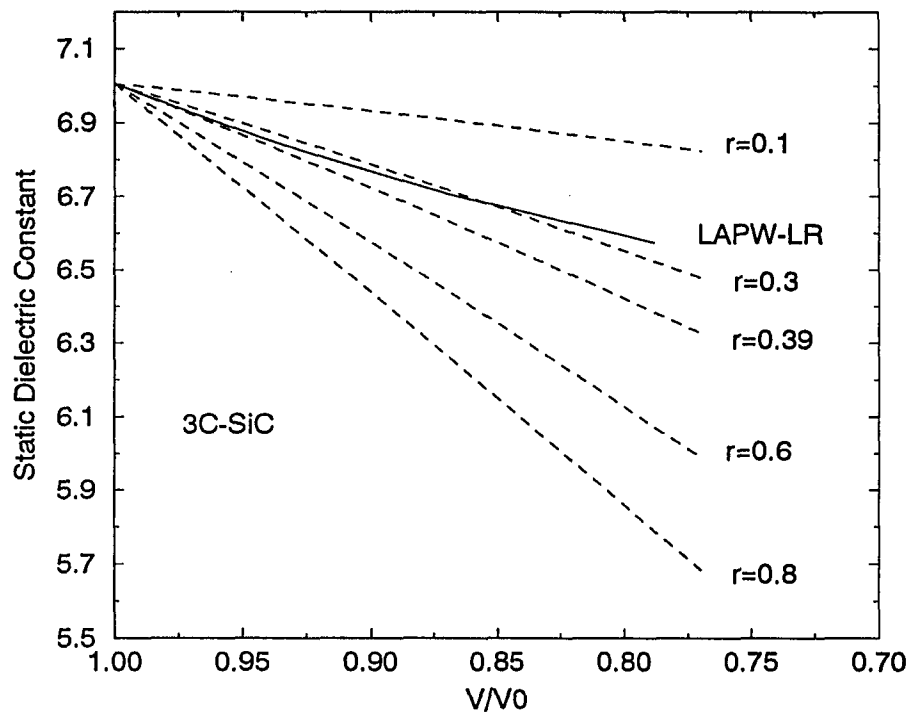


Figure 4.5: Solid line is the calculated dielectric constant $\epsilon_{\infty}(V)$ of 3C-SiC. Dashed lines are the extrapolations with various choices of r in Eq. (4.7). Note V_0 is the volume at ambient pressure.

4.6 Summary

In this Chapter, we have calculated the ground state properties of 3C-SiC. The lattice constant, bulk modulus and pressure derivative of bulk modulus of 3C-SiC agree well with experiment and other groups' LDA calculations. The transition pressure from zincblende phase to rocksalt phase is determined to be 0.65 Mbar, which is close to other theoretical results but lower than the reported experimental value (1.00 Mbar). The discrepancy is due in part to the fact that the experimental transition pressure obtained by diamond-anvil technique is for the forward transition (from zincblende phase to rocksalt phase), which needs an excess pressure [163, 178] beyond the equilibrium value. The cohesive energy per primitive unit cell of zincblende phase is greater than that of rocksalt phase by 107 mRy. The calculated Born effective charge Z^* is in excellent agreement with experiment, but the dielectric constant is 7% too big. The phonon dispersions and the elastic constants agree with available experiment data, demonstrating that different stacking sequences in silicon carbides have little influence on the vibrational properties. The experimental Grüneisen's parameters are well reproduced, and predictions are given for those experimentally unavailable. In 3C-SiC, we find that i) the dielectric constant ϵ_∞ decreases with increasing pressure, and ii) the Born effective charge increases monotonically with pressure, without any evidence of a relative maximum as reported in 6H-SiC by Liu and Vohra [151]. After analyzing the input data in extracting the experimental Born effective charges Z^* of 6H-SiC in Ref. [151], we suggest that the saturation phenomenon of Z^* reported by Ref. [151] is due to approximation in the assumed dependence of dielectric constant ϵ_∞ on pressure, the use of a special set of experimental

data of B_0 and B'_0 , and the uncertainty in measured phonon frequencies, especially at high pressure.

Chapter 5

Lattice Dynamics of KNbO_3

5.1 Introduction

There exist a great number of experimental and theoretical studies on the interesting properties of ferroelectrics, motivated by both curiosity to understand the mechanism underlying the ferroelectric phase transitions and by their importance in a wide range of applications. [197] Among the ferroelectrics, the perovskite oxides ABO_3 , where A and B are metal atoms, present a special opportunity for scientific study owing to their simple crystal structure. The unit cell of perfect perovskite structure ABO_3 with cubic symmetry is shown in Figure 5.1, with the B atom residing at the center of cube, the A atom at corner and three oxygen atoms at the face centers. KNbO_3 , an extensively-studied prototypical material in this family of compounds, can exemplify their common phase transition behavior. It has four phases and undergoes three successive phase transitions [198] when the temperature is decreased: at 701 K, it transforms from a paraelectric cubic phase to a ferroelectric tetragonal phase with

the macroscopic polarization along $[1\ 0\ 0]$; at 488 K, it transforms to an orthorhombic phase with the polarization along a cube edge direction $[1\ 1\ 0]$; and at 210 K, it changes to be a rhombohedral structure with the polarization along a cube diagonal direction $[1\ 1\ 1]$. On heating the phase transition series are reversed and the critical temperatures become 265 K, 493 K and 704K, respectively.

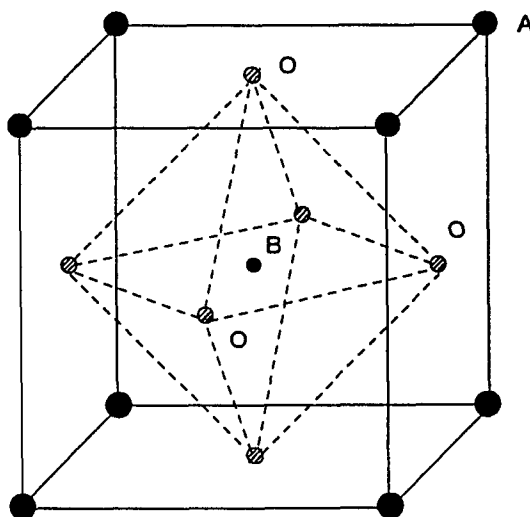


Figure 5.1: The structure of cubic perovskite compounds ABO_3 . Atoms of A, B, and O are represented by the large solid circle, small solid circle, and shaded circles, respectively.

Two models have been proposed to describe the mechanism in the ferroelectric transitions. In the eight-site model, there exist potential minima for Nb atoms along

eight equivalent cube diagonals. When temperature is changed, Nb atoms ordering on these sites results in the distinctive phases: in the paraelectric cubic phase, Nb atoms are fully disordered among these eight sites without any preference; in the tetragonal phase, four out of eight sites are preferentially occupied by Nb atoms, yielding a net polarization along $[1\ 0\ 0]$ direction; in the orthorhombic phase, Nb atoms occupy only two adjacent sites, yielding a net polarization along $[1\ 1\ 0]$ direction; in the rhombohedral phase, the structure becomes completely ordered. In this order-disorder picture, precursor short range order exists with atomic distortions already present above transition temperature T_c although there is no long range order. However, in the alternative soft-mode model, a displacive picture is proposed to explain the phase transitions by the freezing out, one by one, of three soft transverse optical phonon modes as the temperature is lowered. A soft phonon mode condenses at transition temperature T_c , with the magnitude of the atomic distortions increasing below T_c . Experimental evidences in favor of order-disorder [199,200] and displacive [201,202] transition character have been reported, leaving the controversial debate still open. It is quite possible, however, that the correct understanding of the real ferroelectric transitions should involve a combination of pictures provided by these two models.

The complications in both experimental and theoretical studies in the investigations of the nature of ferroelectric transitions arise from two related aspects: the atomic displacements and the energy differences involved in the transitions are very small. Both transition and macroscopic polarization exhibit strong sensitivity to chemical compositions, defects, electrical boundary conditions, details of domain structure, and stresses, etc. This sensitivity stems from the fact that the ferro-

electricity results from a delicate balance between the long-range electro-static ionic interactions, which favor a ferroelectric state, and short-range repulsions which favor a cubic phase. Nevertheless, considerable insight has been gained recently into the microscopic mechanism for the ferroelectric instability in the perovskite ferroelectrics such as BaTiO_3 and KNbO_3 from first principles calculations based on the local density functional theory. [41,42,138,203–210] Cohen and Krakauer [203] first performed a series of total energy calculations on BaTiO_3 using LAPW method and showed that the cubic phase is unstable with respect to zone-center distortions, in agreement with the fact that experiments have observed ferroelectric transition in this material. Cohen [138] highlighted that the hybridizations between oxygen $2p$ and transition metal titanium $3d$ electrons is an important feature for driving the ferroelectric instability in BaTiO_3 and PbTiO_3 . King-Smith and Vanderbilt [209] carried out systematic calculations of total energy surface for zone-center distortions for eight perovskite oxides. Postnikov *et al.* [206–208] investigated the ground state structure of KNbO_3 and calculated the transverse optic phonon modes at the zone center for cubic, tetragonal and orthorhombic structures. With the use of an effective Hamiltonian constructed from first principles calculations, Zhong, Vanderbilt and Rabe [211] obtained for BaTiO_3 the phase sequence, transition temperatures, latent heats, and spontaneous polarizations which are in good agreement with experiments. Using the powerful linear response density functional method, Yu, Krakauer and Wang [41,42] obtained a complete mapping in the Brillouin zone of the structural instability for cubic KNbO_3 , which reveals a pronounced planar character. In real space, these correspond to chains along the $\langle 1\ 0\ 0 \rangle$ directions of Nb atoms coherently displaced

along the chain direction. The shortest length of the chains is estimated to be about five lattice constant, $5a \sim 20 \text{ \AA}$, in agreement with experimental observation [212]. However, the investigations have also raised a caution about the validity of the local density approximation (LDA). Singh and Boyer [204] find the ferroelectric instabilities in KNbO_3 are quite sensitive to volume, suggesting that the typical tendency of LDA to underestimate the volume can lead to large differences in the energy surface for ferroelectric distortions.

In this chapter, the ground state structure of KNbO_3 is first determined by minimizing the forces acting on the relaxed atoms. Then we calculate Born effective charge tensors and dielectric tensors for both cubic and rhombohedral structures, demonstrating the sensitive dependence of polarizability on the atomic displacements involved in the perovskite ferroelectric transitions. Finally, we present the calculations of the zone-center phonon modes also for cubic and rhombohedral structures. Special attention is paid to the convergence problem in the LDA calculations through the whole chapter.

5.2 Methods

We perform all total energy, forces, and linear response calculations with the LAPW basis set coupled with Kerker type pseudopotentials [93]. Two window partitioning is used to obtain the variational wavefunctions. A set of energy parameters E_l is chosen for each window to calculate the states in it as accurately as possible. For KNbO_3 , the shallow semicore orbitals $\text{K}(3s)$ and $\text{Nb}(4s,4p)$ are treated as valence states, and are included in the lower window while the other bands are treated in

Table 5.1: Correspondence of uniform k -point meshes to the number of special k -points in irreducible Brillouin zone (IBZ).

uniform mesh	Number of special k -points for cubic structure	Number of special k -points for rhombohedral structure
(4 4 4)	4	10
(6 6 6)	10	20
(8 8 8)	20	35

the upper window. The Wigner interpolation formula [56] is used for the exchange-correlation potential, and uniform k -point meshes [83–85] are used to sample the Brillouin zone integration. Table 5.1 lists the number of special k -points in the irreducible BZ wedges for cubic and rhombohedral structures corresponding to the uniform k -point meshes used in our calculations.

The convergence on the k -point sets and number of LAPW basis functions will be discussed later in the subsequent sections.

The lattice constant of the equilibrium state determined from total energy calculations is 4.000 Å, slightly smaller than the experimental value 4.016 Å. [198] The bulk modulus is found to be 192 GPa, consistent with the previous result 195 GPa reported by Singh and Boyer [204] using a local orbital extension LAPW method [213]. The bulk modulus pressure derivative is 3.1.

All calculations below are performed at the experimental lattice constant.

5.3 Ground State Structure

The first thing we want to do is to determine the ground state structure at low temperature for KNbO_3 from LDA calculations. The problem is essentially equivalent to finding the geometry of the system with the lowest energy. One can carry out the total energy calculations for a large number of geometric configurations and map out the energy surface with some interpolation procedure, then identify the lowest energy structure as the ground state structure. Another strategy is to access the ground state by minimizing the forces on all atoms. We can calculate the forces on atoms in one configuration and then displace them in the forces' directions, finally yielding a configuration with forces on all atoms essentially zero. Since the force information reduces greatly the number of configurations that have to be calculated, the second approach is much more efficient in practice.

We treat the Bravais lattice of KNbO_3 as cubic when the temperature is lowered below the last transition, i.e. the temperature range for the existence of rhombohedral structure. This approximation is based on the observation of experiment that the angles of rhombohedral unit cell $\alpha = \beta = \gamma$ differ from 90° by merely $11'$ [214]. This treatment is also supported from LDA calculations performed by Cohen and Krakauer [203] who find the effect of rhombohedral strain on the total energy is negligibly small in BaTiO_3 , a material which has similar structures and transition series to KNbO_3 , and the strain angle is $13'$ there.

We relax the atomic positions subject to rhombohedral structure symmetry

C_{3v} , with three independent parameters Δ_K , Δ_{Nb} and Δ_O to be determined,

$$\begin{aligned}
 K &: \left(\frac{1}{2} + \Delta_K \quad \frac{1}{2} + \Delta_K \quad \frac{1}{2} + \Delta_K \right) \\
 Nb &: \left(\Delta_{Nb} \quad \Delta_{Nb} \quad \Delta_{Nb} \right) \\
 O_1 &: \left(\frac{1}{2} + \Delta_O \quad 0 \quad 0 \right) \\
 O_2 &: \left(0 \quad \frac{1}{2} + \Delta_O \quad 0 \right) \\
 O_3 &: \left(0 \quad 0 \quad \frac{1}{2} + \Delta_O \right)
 \end{aligned}$$

where coordinates are in units of lattice constant and the positions of O_2 and O_3 are related to O_1 by symmetry.

The muffin-tin radii are chosen to be 2.50 *a.u.*, 1.92 *a.u.* and 1.58 *a.u.* for K, Nb and O, respectively. The kinetic energy cutoff is 22.5 Ry., which generates about 810 LAPW basis functions and energy difference converges to better than 5%. However the results show strong sensitivity to the k -point sampling for BZ integration. Table 5.2, 5.3 and 5.4 present the total energy and forces calculations for different configurations with three sets of k -point meshes and the corresponding ground state structures are underlined. The forces on O_2 and O_3 can be readily obtained from the forces on O_1 by symmetry consideration, for instance, $F_y(O_2) = F_z(O_3) = F_x(O_1)$.

Atomic positions can also be expressed with reference to Nb without any loss of generality. The new coordinates for each atom become as follows (in unit of lattice constant):

$$\begin{aligned}
 K &: \left(\frac{1}{2} + \delta_K \quad \frac{1}{2} + \delta_K \quad \frac{1}{2} + \delta_K \right) \\
 Nb &: \left(0 \quad 0 \quad 0 \right) \\
 O_1 &: \left(\frac{1}{2} + \delta_I \quad \delta_{II} \quad \delta_{II} \right) \\
 O_2 &: \left(\delta_{II} \quad \frac{1}{2} + \delta_I \quad \delta_{II} \right) \\
 O_3 &: \left(\delta_{II} \quad \delta_{II} \quad \frac{1}{2} + \delta_I \right)
 \end{aligned}$$

Table 5.2: Total energy and forces for various configurations of KNbO_3 in determining its ground state structure using (4 4 4) k-point mesh. For simplicity, the total energy is shifted by a constant. All coordinates are in units of lattice constant.

Δ_K	Δ_{Nb}	Δ_O	E	F_K	F_{Nb}	$F_x(O_1)$	$F_y(O_1)$ or $F_z(O_1)$
$a(1\ 1\ 1)$	$a(1\ 1\ 1)$	$a(1\ 1\ 1)$	(mRy)	($1\ 1\ 1$) ($mRy/a.u.$)	($1\ 1\ 1$) ($mRy/a.u.$)	($mRy/a.u.$)	($mRy/a.u.$)
0.000	0.000	0.000	-8.097	0.00	0.00	0.00	0.00
0.000	0.007	0.000	-8.130				
0.000	0.015	0.000	-8.071				
0.000	0.020	0.000	-7.749				
0.000	0.025	0.000	-6.970				
0.016	0.025	-0.001	-8.474	-0.28	-3.04	0.28	1.38
0.016	0.015	-0.001	-8.406	-3.67	4.93	-2.74	0.64
0.015	0.020	0.000	-8.681	-1.34	1.86	-4.09	1.67
0.015	0.020	-0.001	-8.717	-1.52	1.42	-2.11	0.92
0.015	0.020	-0.002	-8.709	-1.53	1.25	-0.29	0.18
0.013	0.0214	-0.002	-8.704	-0.08	-0.68	0.02	0.20
0.015	0.0214	-0.002	-8.684	-1.01	0.01	0.22	0.30
0.014	0.0214	-0.002	-8.700	-0.46	-0.34	0.13	0.27
<u>0.013</u>	<u>0.0209</u>	<u>-0.002</u>	<u>-8.726</u>	<u>-0.13</u>	<u>-0.24</u>	<u>-0.13</u>	<u>0.14</u>

Table 5.3: Total energy and forces for various configurations of KNbO₃ in determining its ground state structure using (6 6 6) k-point mesh. The total energy is shifted by a constant. All coordinates are in units of lattice constant. The experimental structure determined by Hewat [214] is also used as one set of input data and is denoted with superscript ^a.

Δ_K	Δ_{Nb}	Δ_O	E	F_K	F_{Nb}	$F_x(O_1)$	$F_y(O_1)$ or $F_z(O_1)$
$a(1\ 1\ 1)$	$a(1\ 1\ 1)$	$a(1\ 1\ 1)$	(mRy)	(1 1 1) (mRy/a.u.)	(1 1 1) (mRy/a.u.)	(mRy/a _B)	(mRy/a.u.)
0.000	0.000	0.000	-6.196	0.00	0.00	0.00	0.00
0.000	0.025	0.000	-6.519	8.49	-5.59	-4.24	0.63
0.010	0.025	0.000	-7.854	3.12	-1.34	-3.19	0.55
-0.010	0.025	0.000	-3.953	13.31	-8.35	-5.24	-0.16
0.015	0.025	0.000	-8.067	0.23	0.53	-2.73	0.81
0.015	0.025	-0.005	-7.454	0.19	-3.88	9.43	-2.85
0.015	0.025	-0.002	-7.993	0.16	-0.13	2.11	-0.66
0.015	0.025	-0.001	-8.057	0.38	-0.33	-0.42	0.06
<u>0.016</u>	<u>0.025</u>	<u>-0.001</u>	<u>-8.060</u>	<u>0.16</u>	<u>0.03</u>	<u>-0.33</u>	<u>0.11</u>
Expt. ^a	Expt. ^a	Expt. ^a	-6.928	-0.76	10.78	-11.23	0.76

Table 5.4: Total energy and forces for various configurations of KNbO_3 in determining its ground state structure using $(8\ 8\ 8)$ k-point mesh. The total energy is shifted by a constant. All coordinates are in units of lattice constant.

Δ_K	Δ_{Nb}	Δ_O	E	F_K (1 1 1)	F_{Nb} (1 1 1)	$F_x(O_1)$	$F_y(O_1)$ or $F_z(O_1)$
$a(1\ 1\ 1)$	$a(1\ 1\ 1)$	$a(1\ 1\ 1)$	(mRy)	(mRy/a.u.)	(mRy/a.u.)	(mRy/a.u.)	(mRy/a.u.)
0.000	0.000	0.000	-6.087	0.00	0.00	0.00	0.00
0.000	0.025	0.000	-6.537	8.56	-4.69	-4.13	0.04
<u>0.015</u>	<u>0.025</u>	<u>-0.001</u>	<u>-8.076</u>	<u>0.39</u>	<u>-0.17</u>	<u>-0.38</u>	<u>-0.03</u>

where δ_K , δ_I and δ_{II} are three independent parameters. Table 5.5 summarizes and compares the information of ground state structures from calculations and experiment. Previous LDA calculations with LMTO method as well as rigid oxygen cage approximation [206] are also included.

Table 5.5: Ground state structures determined by calculations and experiment for KNbO_3 .

k -point mesh	δ_K	δ_I	δ_{II}	$E_g - E_c(mRy)$
(4 4 4)	0.008	0.023	0.021	-0.63
(6 6 6)	0.009	0.026	0.025	-1.86
(8 8 8)	0.010	0.026	0.025	-1.99
LMTO ^A	$\sim 0.018^B$ $\sim 0.026^C$	$\sim 0.018^B$ $\sim 0.027^C$	$\sim 0.018^B$ $\sim 0.027^C$	$\sim -1.0^B$ $\sim -3.0^C$
Expt. ^D	0.0130 ± 81	0.0333 ± 15	0.0301 ± 9	

^A Ref. [206].

^B Calculations at lattice constant $a=3.93 \text{ \AA}$ in Ref. [206]

^C Calculations at lattice constant $a=4.00 \text{ \AA}$, the extrapolated experimental value for $T = 0 \text{ K}$, see Ref. [206].

^D Measurements are done at $T= 230 \text{ K}$ on the rhombohedral phase, see Ref. [214].

Remarks are given to features in these four tables:

i) Cubic symmetry phase of KNbO_3 is unstable against the zone-center distortions since its energy is higher than that of some rhombohedral structure configurations. This point is clearly demonstrated in the calculations with all three set k -point meshes and agree with experiment.

ii) The ground state structures are obtained by minimizing the forces on all

atoms. The largest residual force component is smaller than ~ 0.4 mRy/*a.u.*, i.e. 0.01 eV/Å, which is regarded as essentially zero. Within the accuracy (~ 0.01 mRy) of total energy calculations, the ground state structures determined from forces also have lowest energy in all configurations. This displays that two methods are equivalent in practice as they are in principle.

iii) Table.5.5 indicates a larger *k*-point set is desirable to study the ferroelectric properties such as well depth. The energy difference between the cubic ideal structure and the ground state, $(E_c - E_g)$, depends strongly on the size of *k*-point set. Use of (6 6 6) set increases $|E_c - E_g|$ by 200% compared with (4 4 4) set. However, use of an (8 8 8) set changes the energy difference $(E_c - E_g)$ by just 7% compared with (6 6 6) set, suggesting (6 6 6) set would be good enough in many calculations. This point is immediately confirmed by another comparison: the ground state structures determined with (6 6 6) and (8 8 8) sets exhibit little difference. Both (6 6 6) and (8 8 8) sets show that, as only Nb atom moves in the unit cell along the [1 1 1] direction, it experiences a pronounced double well potential, which favors ferroelectric transition. While (4 4 4) set gives a rather shallow and short-ranged double well potential such that the energy is already higher than cubic phase by ~ 1.1 mRy when Nb is moved to $(0.025\ 0.025\ 0.025)a$.

iv) Relaxation energy plays a great role in the the determination of well depth. For example with the use of (8 8 8) *k*-point set, moving Nb from origin to $(0.025\ 0.025\ 0.025)a$ while keeping other atoms fixed, the total energy of the system indeed decreases, but the energy gain is just 0.45 mRy; however, when K and oxygen atoms are relaxed, the energy gain becomes 1.99 mRy.

v) Table.5.5 presents the rhombohedral structure of KNbO_3 determined by Hewat with neutron diffraction measurements on powdered crystal, using the profile refinement technique to analyze the data. The distortion of the oxygen octahedron, i.e. the difference of values between δ_I and δ_{II} in Table.5.5, is observed by experiment. Our calculations qualitatively reproduced this small distortion of oxygen octahedron with correct order of sequence but underestimated the absolute values. The atomic positions in rhombohedral symmetry structure determined by us agree well with experiment if taking into account the uncertainties due to LDA approximations, sensitive dependence of ferroelectric properties on volume, as well as experimental error limit. Recently, Postnikov *et al.* [206] conducted LDA total energy calculations on KNbO_3 to determine its ground state structure with linear muffin-tin orbital (LMTO) basis set. In order to reduce the computational burden, they introduced rigid oxygen cage approximation to freeze one independent parameter in three, assuming $\delta_I = \delta_{II}$. One distinct feature in their results is that K moves about the same amount as the oxygen cage, implying that K and O atoms move rigidly. However, in contrast to their results, our calculations demonstrate the displacement of K is much smaller than that of O, which is supported by experimental measurements as shown in Table.5.5. So we suggest that the commonly cited [106, 199, 200] assumption that the ferroelectric transition in cubic perovskites essentially involves only the displacement of Nb (or, generally, of B atom in ABO_3 structure) with respect to the rigid lattice of all other atoms might be oversimplified.

5.4 Z^* and ϵ_∞ for Both Cubic and Rhombohedral Structures

Since they determine the strength of long-range Coulomb interactions in materials, Born effective charges Z^* are basic quantities in the studies of lattice dynamics. However, calculations from first principles of these charges in perovskite ferroelectrics became available only quite recently. [41, 42, 106, 215, 216] Here we present studies on the Z^* and ϵ_∞ for both cubic and rhombohedral structures. A (6 6 6) k -point set has been used to assure accuracy.

In cubic symmetry structure, K and Nb have same site symmetry. Since three directions \hat{x} , \hat{y} and \hat{z} are equivalent, Born effective charge tensors $Z^*(K)$ and $Z^*(Nb)$ are isotropic. However, for oxygen O, two directions are inequivalent: one is along Nb-O bond direction and another one is perpendicular to this bond, which are denoted as \parallel and \perp respectively. Therefore $Z^*(O)$ is diagonal but with two distinctive values $Z^*(O)_\parallel$ and $Z^*(O)_\perp$. In the calculations for rhombohedral phase, we have used the theoretically determined ground state structure shown in Table 5.3. Due to the low symmetry of the rhombohedral structure, the Born effective charge tensors no longer have a simple diagonal form. For both cubic and rhombohedral symmetry, the three oxygen atoms are equivalent and their Born effective charge tensors can be related by symmetry. We list all calculated Z^* as follows.

For cubic symmetry structure:

$$Z^*(K) = \begin{pmatrix} 1.117 & 0 & 0 \\ 0 & 1.117 & 0 \\ 0 & 0 & 1.117 \end{pmatrix}$$

$$Z^*(Nb) = \begin{pmatrix} 9.668 & 0 & 0 \\ 0 & 9.668 & 0 \\ 0 & 0 & 9.668 \end{pmatrix}$$

$$Z^*(O_1) = \begin{pmatrix} -7.277 & 0 & 0 \\ 0 & -1.738 & 0 \\ 0 & 0 & -1.738 \end{pmatrix}$$

$$Z^*(O_2) = \begin{pmatrix} -1.738 & 0 & 0 \\ 0 & -7.277 & 0 \\ 0 & 0 & -1.738 \end{pmatrix}$$

$$Z^*(O_3) = \begin{pmatrix} -1.738 & 0 & 0 \\ 0 & -1.738 & 0 \\ 0 & 0 & -7.277 \end{pmatrix}$$

For rhombohedral symmetry structure,

$$Z^*(K) = \begin{pmatrix} 1.145 & -0.006 & -0.006 \\ -0.006 & 1.145 & -0.006 \\ -0.006 & -0.006 & 1.145 \end{pmatrix}$$

$$Z^*(Nb) = \begin{pmatrix} 8.162 & -0.345 & -0.345 \\ -0.345 & 8.165 & -0.345 \\ -0.345 & -0.345 & 8.165 \end{pmatrix}$$

$$Z^*(O_1) = \begin{pmatrix} -6.265 & 0.142 & 0.142 \\ 0.239 & -1.554 & -0.005 \\ 0.239 & -0.005 & -1.554 \end{pmatrix}$$

$$Z^*(O_2) = \begin{pmatrix} -1.554 & 0.239 & -0.005 \\ 0.142 & -6.265 & 0.142 \\ -0.005 & 0.239 & -1.554 \end{pmatrix}$$

$$Z^*(O_3) = \begin{pmatrix} -1.554 & -0.005 & 0.239 \\ -0.005 & -1.554 & 0.239 \\ 0.142 & 0.142 & -6.265 \end{pmatrix}$$

The eigenvalues of the Born effective charge tensors are summarized in Table 5.6, in which other calculations for cubic and tetragonal symmetry structures are also included for comparison.

In the rhombohedral symmetry structure, the degeneracy of eigenvalues of Born effective charge tensors has been lifted due to its low symmetry. For K and Nb, three eigenvectors of the Born effective charge tensors are perpendicular to each other, the [1 1 1] direction being an obvious principal axis with corresponding eigenvalues in KNbO₃ of 1.13 and 7.47 respectively. The other two eigenvectors have degenerate eigenvalues and can be chosen as [1 -1 0] and [1 0 -1] with uncertainty of a free phase

Table 5.6: Comparison of eigenvalues of Born effective charge tensors from linear response (LR) and Berry Phase (BP) calculations for KNbO_3 .

	Cubic	Cubic	Cubic	Tetragonal	Rhomboh.	Rhomboh.
	Present (6 6 6)	Present (4 4 4)	PW-BP ^a (4 4 20)	LAPW-BP ^b	Present (6 6 6)	Present (4 4 4)
K	1.12	1.12	1.14	0.82	1.16 1.16 1.13	1.10 1.10 1.17
Nb	9.67	9.31	9.23	9.13	8.51 8.51 7.47	8.92 8.92 8.00
$O_1 \parallel$	-7.28	-6.84	-7.01	-6.58	-6.28	-6.36
$O_1 \perp$	-1.74	-1.64	-1.68	-1.68	-1.54 -1.55	-1.54 -1.57

^aZhong *et al.* [215].

^bResta *et al.* [106].

factor. For oxygen atom O_1 , the three eigenvectors of the Born effective charge tensors are no longer perpendicular to each other since the tensor is not symmetric. It is easy to identify that $[0\ 1\ -1]$ direction remains an eigenvector whose eigenvalue is -1.55. But the other two eigenvectors cannot be determined by geometry, instead they depend on the details of interactions in the material. Nevertheless, for convenience in the explanation, we still use $Z^*(O)_{\parallel}$ and $Z^*(O)_{\perp}$ to denote the eigenvalues although the corresponding eigenvectors are already slightly deviated from their original directions in cubic symmetry structure due to small atomic displacements involved in the transitions.

All calculations show surprisingly large Born effective charges $Z^*(\text{Nb})$ and $Z^*(\text{O})_{\parallel}$. These values are by far larger than their corresponding nominal ionic charges +5 and -2, revealing that a large dynamic contribution is superimposed to the static charges and a large amount of dynamic charge transfer occurs along the Nb-O bond as the length of the bond is varied. Actually, the anomalously large Born effective charges are a common feature in at least the perovskite ferroelectrics ABO_3 , stemming from the covalent nature of the strong B-O bond (bond of Nb $4d$ and O $2p$ in KNbO_3). These unusually large Born effective charges give rise to strong long-range ionic interactions, which favor the ferroelectric instability and make it sensitive to the size and formulation of domains as well as electric boundary conditions. The large Born effective charges lead to large LO-TO splitting in perovskites in the sense the soft TO mode is closely related to the hardest LO modes [215].

Table 5.6 indicates that Born effective charges, especially $Z^*(\text{Nb})$ and $Z^*(\text{O})_{\parallel}$, are quite sensitive to the structural details. The atomic displacements involved in the transformation from cubic to rhombohedral structures are rather small, typically a couple of percent of lattice constant. However, the values of $Z^*(\text{Nb})$ and $Z^*(\text{O})_{\parallel}$ change up to 20%; if subtracting the static charges associated with ions, the percentage change of the pure dynamic charge part can be as large as 50 %. This can be understood if we remember the anomalously large Born effective charges of $Z^*(\text{Nb})$ and $Z^*(\text{O})_{\parallel}$ result mainly from the large orbital hybridizations of Nb $4d$ and O $2p$, which has been elegantly demonstrated by Posternak, Resta, and Baldereschi [217]. It is reasonable to expect that these charges depend sensitively on the environmental conditions such as Nb-O bond length and site symmetry of atoms in crystal that

subject to change in phase transitions. Recently Ghosez *et al.* [216] reported their calculations of Born effective tensors for four phases of BaTiO₃ and observed that the effective charges show little sensitivity to the isotropic volume changes but rather strong dependence on the atomic positions.

We have checked the convergence of Born effective charges to the size of k -point set for Brillouin zone integration. A (6 6 6) set reduces the violation of the acoustic sum rule to be smaller than that of (4 4 4) set by an order of magnitude. Specifically, with the use of (6 6 6) k -point set, we have

$$\sum_i Z_i^* = \begin{pmatrix} -0.032 & 0 & 0 \\ 0 & -0.032 & 0 \\ 0 & 0 & -0.032 \end{pmatrix}$$

for cubic symmetry structure and

$$\sum_i Z_i^* = \begin{pmatrix} -0.066 & 0.025 & 0.025 \\ 0.025 & -0.066 & 0.025 \\ 0.025 & 0.025 & -0.066 \end{pmatrix}$$

for rhombohedral symmetry structure. This level of satisfaction to the acoustic sum rule is comparable to simple semiconductors.

We observe about 5% difference of the calculated Born effective charges for both cubic and rhombohedral structures when we chose (6 6 6) instead of (4 4 4) k -point sets. We also used (4 4 4) k -point set to check the convergence of Born effective charges of cubic symmetry structure to the kinetic energy cutoff, i.e. the number of LAPW basis functions. The results with the kinetic energy cutoff 22.5 Ry differ from those with 18.0 Ry less than 0.5%. So when we calculated the Born

effective charges for cubic structure, we used the kinetic energy cutoff 22.5 Ry; when we calculated for rhombohedral structure, the kinetic energy cutoff 18.0 Ry was used to save computational burden because many more k -points appeared in the irreducible Brillouin zone wedge.

Table 5.6 also presents the Born effective charges calculated for tetragonal and cubic symmetry structures by other groups using Berry phase techniques [106,215]. Besides K, which is very ionic and plays a minor role in ferroelectric transition, all other Born effective charges they obtained are relatively smaller than our results with (6 6 6) k -point set. Their calculations appear to be closer to our smaller k -point set (4 4 4) mesh. In Berry phase calculations, the Born effective charges are extracted from the finite polarization differences between perfect and distorted structures. In principle, finite difference polarization calculations for two structures give the same results as the linear response method in the sense that the nonlinearity of polarization is suppressed to vanishing when distortions approach zero. Zhong *et al.* [215] used a (4 4 20) k -point mesh and distortions with amplitudes of typically 0.2% of the lattice constants in their calculations. They also investigated the Born effective charges of tetragonal phase of KNbO_3 but found only 2% of change compared with cubic case. Resta *et al.* [106] however directly used the experimental tetragonal structure as distortions compared to cubic phase. Our calculations indicate the Born effective charges vary considerably when the atomic positions change only about 2% of lattice constant, suggesting rather small distortions should be used to ensure the accuracy of Born effective charges in Berry phase calculations.

The calculated dielectric tensors also display dependence on atomic positions.

For the cubic symmetry case,

$$\epsilon_{\infty} = \begin{pmatrix} 6.63 & 0 & 0 \\ 0 & 6.63 & 0 \\ 0 & 0 & 6.63 \end{pmatrix}.$$

For rhombohedral structure,

$$\epsilon_{\infty} = \begin{pmatrix} 5.79 & -0.15 & -0.15 \\ -0.15 & 5.79 & -0.15 \\ -0.15 & -0.15 & 5.79 \end{pmatrix},$$

with eigenvalues 5.64, 5.64, and 5.49. The extracted experimental value is 4.69 [215].

5.5 Phonon Modes at Γ -point of Cubic Structure

Table 5.7 gives the phonon spectrum at Γ point for cubic structure KNbO_3 . Note the eigenvectors of dynamical matrix are the mass weighed displacements, i.e. $u_j = \sqrt{m_j} v_j$, where u_j are the components of eigenvectors and v_j are the actual atomic displacements, and m_j are the atomic mass related to the components.

The TO mode frequencies are calculated with use of (6 6 6) k -point set. In the construction of dynamical matrix for LO modes, we used our calculated results of Born effective charges for cubic phase and the corresponding experimental dielectric constant. The frozen phonon calculations of Singh and Boyer with LAPW method [204], Zhong, King-Smith, and Vanderbilt with plane wave coupled with ultrasoft pseudopotentials [215], and Postnikov *et al.* with LMTO method [207] are also included in Table 5.7 as well as experimental data. All these calculations find

Table 5.7: Comparison of calculated Γ -point phonon frequencies (cm^{-1}) in cubic KNbO_3 with experiment.

Present	LAPW ^a	PW ^b	LMTO ^c	Experiment ^d
TO modes:				
197 <i>i</i>	115 <i>i</i>	143 <i>i</i>	203 <i>i</i>	soft
170	168	188	193	198
473	483	506	483	521
243	266		234	280 ^e
LO modes:				
167		183		190
403		407		418
888		899		826

^aSingh *et al.* [204].

^bZhong *et al.* [215].

^cPostnikov *et al.* [207].

^dFontana *et al.* [198].

^e Measured in the tetragonal phase, $T = 585$ K.

unstable TO modes at Γ with similar imaginary frequencies corresponding to the observed soft mode.

The transverse phonon modes are listed in Table 5.8.

We find that the eigenvectors are rather insensitive to the k -point set choice. The phonon patterns obtained with (6 6 6) k -point set show little difference from those with (4 4 4) set. The phonon frequencies of TO modes experience little change either except for the low lying soft modes which become more unstable by about 50*i* when (6 6 6) set is used, consistent with the observation that the double well is deeper with use of (6 6 6) k -point set than use of (4 4 4) set in the ground state structure

Table 5.8: Eigenvectors of calculated TO(Γ) phonon modes in cubic KNbO₃.

Modes	freq.(cm ⁻¹)	K	Nb	O ₁	O ₂	O ₃
TO_1	197i	0.01	-0.59	0.55	0.42	0.42
TO_2	170	0.88	-0.37	-0.18	-0.15	-0.18
TO_3	473	0.02	-0.08	0.46	0.46	-0.76
TO_4	243	0.00	0.00	0	1	-1

calculations. Here are the basic features of the eigenvectors: for soft modes TO_1 , Nb vibrates against three oxygen atoms with K essentially unmoved; for TO_2 modes, K vibrates against all of the other atoms; for TO_3 modes, one O atom vibrates against the other two O atoms, accompanied by rather small amplitude oscillations of Nb with the former and K with the latter ones; for TO_4 modes, K and Nb are exactly at rest, the oscillations involve only three O atoms. For instance, viewed along \hat{x} direction as shown in Table 5.8, O₂ and O₃ in TO_4 mode move with the same amplitudes but in opposite directions while O₁ has no displacement component along \hat{x} direction. The eigenvectors we obtained also agree very well with previous LAPW calculations by Singh and Boyer [204], but differ much from those reported by Postnikov *et al.* [207] with LMTO method. One of the sharp differences is that we predict the K is almost unmoved in soft mode vibrations. On the contrary, Postnikov *et al.* [207] predict it to move with the same order of magnitude as Nb. It is worth mentioning that in as early as 1981, Fontana *et al.* carried out lattice dynamical calculations with an empirical shell model; their phonon eigenvectors have the same feature as that we obtained here, for example, K is essentially still in the soft modes. [198,218]

The reason why LDA calculations with LAPW and LMTO schemes result in

such discrepancy needs to be investigated further.

5.6 Phonon Modes at Γ -point of Rhombohedral Structure

Table 5.9 and 5.10 present calculated phonon frequencies for the zone center optical modes with (4 4 4) k -point set. The most notable feature is that, as expected, there are no unstable modes in the rhombohedral phase. In fact none of the modes is especially soft either. This confirms the previous assumption of C_{3v} symmetry in determining the theoretical ground structure by minimizing the forces and total energy in the sense that we would have found unstable modes if the ground structure had lower symmetry than C_{3v} . We used the calculated dielectric tensor but rescaled by the experimental data (4.69) in obtaining the frequencies of LO modes.

The agreement with experimental phonon frequencies is quite good. In the rhombohedral phase, the frequency of the longitudinal optic modes depends on the direction along which they are measured, and we are uncertain about assigning directions to some of the measured longitudinal frequencies. For comparison, however, we display calculated longitudinal frequencies for wavevector for \mathbf{q} along two directions. The highest frequencies of LO mode vary as much as about 30 cm^{-1} when the measuring direction changes. We would expect that the phonon spectrum at Γ point shift somewhat if a (6 6 6) k -point set were used and the largest change of frequencies would be associated with TO_1 modes which are most closely related to the soft modes in cubic structure. But the basic feature that every mode is stable will not be affected

Table 5.9: Rhombohedral KNbO_3 zone center phonon frequencies (cm^{-1}) for optical modes. $\text{TO}_i(i=1,4)$ labels are from experiment as shown.

Symmetry of Calculated Modes ^a	Present	Experiment ^{b,c}	Experimental Symmetry Label ^b
E	178	220	TO ₁
A ₁	195	265	
E	171	198	TO ₂
A ₁	175	198	
E	262	301	TO ₄
A ₂	251	301	
E	501	536	TO ₃
A ₁	540	602	

^a Ref. [219].

^b Ref. [198].

^c Ref. [220].

at all.

The eigenvectors of TO modes at Γ point are summarized in Table 5.11. Since the crystal symmetry is low, the phonon modes have a more complex form than those in cubic structure. The eigenmodes of the 178 cm^{-1} E and the 195 cm^{-1} A₁ phonons in Table 5.11 correspond most closely to the unstable modes in the cubic structure.

Table 5.10: Rhombohedral KNbO_3 zone center longitudinal optical phonon frequencies(cm^{-1}). $\text{LO}_i(i=1,4)$ labels are from experiment as shown.

Present <1 1 1>	Present <1 -1 0>	Experiment ^{b,c}	Experimental Symmetry Label ^b
175	171	198	LO_2
262	262	301	LO_4
409	402	423	LO_1
819	847	837	LO_3

^b Ref. [198].

^c Ref. [220].

Table 5.11: Eigenvectors of calculated transverse phonon modes at Γ -point in rhombohedral structure of KNbO_3 .

Modes (cm^{-1})	K	Nb	O ₁	O ₂	O ₃
E 178	(0.07,-0.07,0.00)	(-0.45,0.43,0.01)	(0.29,-0.34,-0.03)	(0.35,-0.28,0.01)	(0.33,-0.32,-0.01)
	(-0.04,-0.04,0.08)	(0.24,0.27,-0.51)	(-0.16,-0.18,0.38)	(-0.17,-0.17,0.38)	(-0.20,-0.22,0.33)
A ₁ 195	(0.02,0.02,0.02)	(0.32,0.32,0.32)	(-0.22,-0.30,-0.30)	(-0.30,-0.22,-0.30)	(-0.30,-0.30,-0.22)
E 171	(-0.35,-0.37,0.72)	(0.12,0.13,-0.25)	(0.08,0.10,-0.18)	(0.10,0.08,-0.18)	(0.08,0.08,-0.15)
	(-0.63,-0.62,0.01)	(0.22,-0.22,-0.00)	(0.13,-0.15,0.01)	(0.15,-0.13,-0.01)	(0.16,-0.16,0.00)
A ₁ 175	(-0.51,-0.51,-0.51)	(0.23,0.23,0.23)	(0.07,0.08,0.08)	(0.08,0.07,0.08)	(0.08,0.08,0.07)
E 262	(0.01,0.01,-0.01)	(-0.01,-0.01,0.02)	(0.01,0.47,-0.05)	(0.52,0.02,0.05)	(-0.52,-0.47,-0.02)
	(0.01,-0.01,0.00)	(-0.02,0.02,0.00)	(0.03,0.33,0.57)	(-0.24,-0.02,-0.57)	(0.24,-0.33,0.00)
A ₂ 251	(0.00,0.00,0.00)	(0.00,0.00,0.00)	(0.00,-0.41,0.41)	(0.41,0.00,-0.41)	(-0.41,0.41,0.00)
E 501	(-0.01,0.01,0.00)	(-0.02,0.02,0.00)	(0.63,0.24,0.02)	(-0.27,-0.56,0.05)	(-0.29,0.26,-0.07)
	(0.01,0.01,-0.01)	(0.01,0.01,-0.02)	(-0.28,0.20,-0.31)	(0.14,-0.41,-0.30)	(0.11,0.17,0.69)
A ₁ 540	(0.01,0.01,0.01)	(0.03,0.03,0.03)	(-0.50,0.20,0.20)	(0.20,-0.50,0.20)	(0.20,0.20,-0.50)

5.7 Summary

We have determined the ground state structure of KNbO_3 by minimizing the forces acting on the relaxed atoms. The calculated ground state structure has rhombohedral symmetry and the numerical values of atomic positions are in good agreement with experiment. We calculated the Born effective charge tensors for both cubic and rhombohedral structures, obtaining unusually large Born effective charges $Z^*(\text{Nb})$ and $Z_{\parallel}^*(\text{O})$ that originate from the strong covalent interactions between orbitals of Nb $4d$ and O $2p$. The Born effective charges also exhibit great sensitivity to the structural details in the sense that the charges such as $Z^*(\text{Nb})$ and $Z_{\parallel}^*(\text{O})$ change up to 20 % when the atomic displacements involved in the rhombohedral structure are only a couple of percent of the lattice constant. This can be understood by considering that the atomic displacements in the rhombohedral structure change both the length of Nb-O bond and the local environments which are crucial to the anomalously large dynamical charges of Nb and O in KNbO_3 . The dielectric tensors for cubic and rhombohedral structures are also calculated, revealing up to 20% reduction of eigenvalues of the tensors from cubic to rhombohedral structures. These studies indicate that the polarizability of the perovskites has a strong dependence on the small atomic displacements which are accompanied by the changes of site symmetry in the phase transitions.

Finally, we calculated the phonon modes at Γ point in both cubic and rhombohedral structures. The phonon frequencies agree well with experiment. Eigenvectors of the phonon modes in cubic structure agree with previous LDA calculations by Singh and Boyer [204] and shell model calculations by Fontana *et al.* [218], but differ

much from the results reported by Postnikov *et al.* [207]. All phonon frequencies calculated for rhombohedral structure are stable as expected. The eigenvectors of transverse optic phonons at Γ point are also given. Since the crystal symmetry is low, the LO frequencies show strong dependence on the direction of wavevector \mathbf{q} . Because KNbO_3 is a prototype member in the family of perovskite ferroelectrics, it can be expected that many of the features found in KNbO_3 apply to other materials such as BaTiO_3 etc.

Chapter 6

Conclusion

First principles local density approximation (LDA) calculations using the linear response method are much more efficient than the traditional supercell or dielectric matrix techniques for determining phonon spectra and dielectric constants. In this thesis, we have calculated lattice dynamical properties of materials with this powerful approach using the linearized augmented plane wave (LAPW) basis, which facilitates such calculations for systems containing transition metal and other atoms with localized orbitals. We have accurately obtained the complete phonon dispersions in the Brillouin zone, force constants in real space, dielectric constants, Born effective charges, and elastic constants. Extensive calculations were carried out for the important semiconductors CuCl, SiC and the typical ferroelectric KNbO_3 , greatly advancing our understanding, at the microscopic level, of the physics underlying many of their unusual properties. The theoretical results were compared with available experimental data, and predictions were given for those experimentally unavailable. The success of these calculations leads us to speculate optimistically that they will

be extended to complex systems in material science in the near future with dramatic progress in computational capacity and methods.

Bibliography

- [1] R. O. Jones and O. Gunnarsson, *Review of Modern Physics* **61**, 689 (1989).
- [2] D. J. Singh, *Planewaves, Pseudopotentials and the LAPW Method* (Kluwer Academic Publishers, Massachusetts, 1994).
- [3] W. E. Pickett, *Comp. Phys. Rep.* **9**, 115 (1989).
- [4] P. Hohenberg and W. Kohn, *Phys. Rev.* **136**, B864 (1964).
- [5] W. Kohn and L. J. Sham, *Phys. Rev.* **140**, A1133 (1965).
- [6] see for example K. Kunc, *Electronic Structure, Dynamics and Quantum Structural Properties of Condensed Matter* (ed. by J. T. Devreese and P. Van Camp, Plenum, New York, p.227, 1985).
- [7] K. Kunc and R. M. Martin, *Phys. Rev. Lett.* **48**, 406 (1982).
- [8] S. Wei and M. Y. Chou, *Phys. Rev. Lett.* **69**, 2799 (1992).
- [9] S. Wei and M. Y. Chou, *Phys. Rev. B* **50**, 2221 (1994).
- [10] W. Frank, C. Elsasser, and M. Fahnle, *Phys. Rev. Lett.* **74**, 1791 (1995).

- [11] R. Resta and K. Kunc, *Phys. Rev. B* **34**, 7146 (1986).
- [12] J. B. Mckitterick, *Phys. Rev. B* **28**, 7384 (1983).
- [13] A. Baldereschi and R. Resta, *Ab initio Calculations of Phonon Spectra* (ed. by J. T. Devreese and P. Van Camp, Plenum, New York, p.1, 1981).
- [14] S. Baroni and R. Resta, *Phys. Rev. B* **33**, 7017 (1986).
- [15] R. M. Sternheimer, *Phy. Rev.* **96**, 951 (1954).
- [16] G. D. Mahan, *Phys. Rev. A* **22**, 1780 (1980).
- [17] S. Baroni, P. Giannozzi, and A. Testa, *Phys. Rev. Lett.* **58**, 1861 (1987).
- [18] X. Gonze and J.-P. Vigneron, *Phys. Rev. B* **39**, 13120 (1989).
- [19] S. de Gironcoli, S. Baroni, and R. Resta, *Phys. Rev. Lett.* **62**, 2853 (1989).
- [20] P. Giannozzi, S. Gironcoli, P. Pavone, and S. Baroni, *Phys. Rev. B* **43**, 7231 (1991).
- [21] R. Yu and H. Krakauer, *Phys. Rev. B* **49**, 4467 (1994).
- [22] A. D. Corso, S. Baroni, and R. Resta, *Phys. Rev. B* **47**, 3588 (1993).
- [23] F. Ancilotto *et al.*, *Phys. Rev. B* **43**, 8930 (1991).
- [24] M. B. Nardelli and S. Baroni, *Phys. Rev. Lett.* **69**, 1069 (1992).
- [25] J. Fritsch, P. Pavone, and U. Schröder, *Phys. Rev. Lett.* **71**, 4195 (1993).
- [26] X. Gonze, D. C. Allan, and M. P. Teter, *Phys. Rev. Lett.* **68**, 3603 (1992).

- [27] X. Gonze, J.-C. Charlier, D. C. Allan, and M. P. Teter, *Phys. Rev. B* **50**, 13035 (1994).
- [28] S. de Gironcoli, *Phys. Rev. B* **46**, 2412 (1992).
- [29] C. Lee, P. Ghosec, and X. Gonze, *Phys. Rev. B* **50**, 13379 (1994).
- [30] C. Lee and X. Gonze, *Phys. Rev. Lett.* **72**, 1686 (1994).
- [31] A. Quong and B. M. Klein, *Phys. Rev. B* **46**, 10734 (1992).
- [32] A. Quong, *Phys. Rev. B* **49**, 3226 (1994).
- [33] A. Fleszar and X. Gonze, *Phys. Rev. Lett.* **64**, 2961 (1990).
- [34] O. Schütt *et al.*, *Phys. Rev. B* **50**, 3746 (1994).
- [35] K. Karch *et al.*, *Phys. Rev. B* **50**, 17054 (1994).
- [36] O. K. Andersen, *Phys. Rev. B* **12**, 3060 (1975).
- [37] E. Wimmer *et al.*, *Phys. Rev. B* **24**, 864 (1981).
- [38] S.-H. Wei and H. Krakauer, *Phys. Rev. Lett.* **55**, 1200 (1985).
- [39] S. Y. Savrasov, *Phys. Rev. Lett.* **69**, 2819 (1992).
- [40] S. Y. Savrasov, D. Y. Savrasov, and O. K. Anderson, *Phys. Rev. Lett.* **72**, 372 (1994).
- [41] R. Yu and H. Krakauer, *Phys. Rev. Lett.* **74**, 4067 (1995).
- [42] R. Yu, C.-Z. Wang, and H. Krakauer, *Ferroelectrics* **164**, 161 (1995).

- [43] C.-Z. Wang, R. Yu, and H. Krakauer, *Phys. Rev. Lett.* **72**, 368 (1994).
- [44] C.-Z. Wang, R. Yu, and H. Krakauer, to be published .
- [45] C.-Z. Wang, R. Yu, and H. Krakauer, to be published .
- [46] H. Krakauer, R. Yu, , and C.-Z. Wang, *Ferroelectrics* **151**, 39 (1993).
- [47] H. Krakauer, R. Yu, and C.-Z. Wang, *Inter. J. of Quantum Chemistry* (1995).
- [48] H. Krakauer, R. Yu, , and C.-Z. Wang, *J. Phys. Chem. Solids* (1995).
- [49] for example see the review by W.E. Pickett, H. Krakauer, R. E. Cohen, and D. J. Singh, *Science* **255**, 246 (1992).
- [50] J. G. Bednorz and K. A. Muller, *Z. Phys. B* **64**, 189 (1986).
- [51] H. Krakauer, W. E. Pickett, and R. E. Cohen, *Phys. Rev. B* **47**, 1002 (1993).
- [52] D. S. J. Kulda, P. Pavone, and Y. Ishii, *Phys. Rev. B* **50**, 13347 (1994).
- [53] K. Kunc and R. M. Martin, *Phys. Rev. B* **24**, 2311 (1981).
- [54] C. Cheng, K. Kunc, and V. Heine, *Phys. Rev. B* **39**, 5892 (1989).
- [55] O. Gunnarsson and B. I. Lundqvist, *Phys. Rev. B* **13**, 4274 (1976).
- [56] E. Wigner, *Phys. Rev.* **46**, 1002 (1934).
- [57] D. M. Ceperley, *Phys. Rev. B* **18**, 3126 (1978).
- [58] D. M. Ceperley and B. I. Alder, *Phys. Rev. Lett.* **45**, 566 (1980).

- [59] J. P. Perdew and A. Zunger, Phys. Rev. B **23**, 5048 (1981).
- [60] L. Hedin and B. I. Lundqvist, J. Phys. C **4**, 2064 (1971).
- [61] U. von Barth and L. Hedin, J. Phys. C **5**, 1629 (1972).
- [62] S. H. Vosko, L. Wilk, and M. Nusair, Can. J. Phys. **58**, 1200 (1980).
- [63] S. H. Vosko and L. Wilk, Phys. Rev. B **22**, 3812 (1980).
- [64] L. J. Sham and W. Kohn, Phys. Rev. **145**, B561 (1966).
- [65] for instance see review by W. E. Pickett, Rev. Modern Phys. **61**, 433 (1989).
- [66] S. Lundqvist and N. H. March, *Theory of the Inhomogeneous Electron Gas* (Plenum, New York, 1983).
- [67] F. Hund, Z. Phys. **33**, 345 (1925).
- [68] J. Perdew *et al.*, Phys. Rev. B **46**, 6671 (1992).
- [69] O. Gunnarsson, M. Jonson, and B. I. Lundqvist, Phys. Rev. B **20**, 3136 (1979).
- [70] A. Svane and O. Gunnarsson, Phys. Rev. B **37**, 9919 (1988).
- [71] A. Svane, Phys. Rev. Lett. **68**, 1900 (1992).
- [72] D. C. Langreth and M. J. Mehl, Phys. Rev. Lett. **47**, 446 (1981).
- [73] D. C. Langreth and M. J. Mehl, Phys. Rev. B **28**, 1809 (1983).
- [74] J. C. Slater, Phys. Rev. **51**, 846 (1937).

- [75] J. C. Slater, *Advances in Quantum Chemistry* **1**, 35 (1964).
- [76] S.-H. Wei, Ph.D. thesis, The College of William & Mary, 1985.
- [77] Z. W. Lu, Ph.D. thesis, The College of William & Mary, 1989.
- [78] R. Yu, D. Singh, and H. Krakauer, *Phys. Rev. B* **43**, 6411 (1991).
- [79] D. D. Koelling and B. N. Harmon, *J. Phys. C* **10**, 3107 (1977).
- [80] M. Weinert, *J. Math. Phys.* **22**, 2433 (1981).
- [81] O. Jepsen and O. K. Andersen, *Solid State Commun.* **9**, 1763 (1971).
- [82] J. Rath and A. J. Freeman, *Phys. Rev. B* **11**, 2109 (1975).
- [83] D. J. Chadi and M. L. Cohen, *Phys. Rev. B* **8**, 5747 (1973).
- [84] H. J. Monkhorst and J. D. Pack, *Phys. Rev. B* **13**, 5188 (1976).
- [85] H. J. Monkhorst and J. D. Pack, *Phys. Rev. B* **16**, 1748 (1977).
- [86] M. Methfessel and A. T. Paxton, *Phys. Rev. B* **40**, 3616 (1989).
- [87] M. J. Gillan, *J. Phys. Condens. Matter* **1**, 689 (1989).
- [88] M. Weinert, E. Wimmer, and A. J. Freeman, *Phys. Rev. B* **26**, 4571 (1982).
- [89] M. C. Payne *et al.*, *Rev. Modern Phys.* **64**, 1045 (1992).
- [90] D. R. Hamann, M. Schluter, and C. Chiang, *Phys. Rev. Lett.* **43**, 1494 (1979).
- [91] G. B. Bachelet, D. R. Hamann, and M. Schluter, *Phys. Rev. B* **26**, 4199 (1982).

- [92] D. R. Hamann, *Phys. Rev. Lett.* **42**, 662 (1979).
- [93] G. P. Kerker, *J. Phys. C* **13**, L189 (1980).
- [94] R. Car and M. Parrinello, *Phys. Rev. Lett.* **55**, 2471 (1985).
- [95] J. M. Soler and A. R. William, *Phys. Rev. B* **40**, 1560 (1989).
- [96] J. M. Soler and A. R. William, *Phys. Rev. B* **42**, 9728 (1990).
- [97] J. M. Soler and A. R. William, *Phys. Rev. B* **47**, 6784 (1993).
- [98] S. Goedecker and K. Maschke, *Phys. Rev. B* **45**, 1597 (1992).
- [99] H. Hellmann, *Einführung in die Quantenchemie* (Deuieke, Leipzig, p.285, 1937).
- [100] R. P. Feynman, *Phys. Rev.* **56**, 340 (1939).
- [101] P. Pulay, *Mol. Phys.* **17**, 197 (1969).
- [102] P. Bendt and A. Zunger, *Phys. Rev. Lett.* **50**, 1684 (1983).
- [103] A. A. Maradudin, E. W. Montroll, G. H. Weiss, and I. P. Ipatova, *Solid State Physics* (Academic, New York, 1971), Vol. suppl. 3.
- [104] R. Pick, M. H. Cohen, and R. M. Martin, *Phys. Rev. B* **1**, 910 (1970).
- [105] R. D. King-Smith and D. Vanderbilt, *Phys. Rev. B* **47**, 1651 (1993).
- [106] R. Resta, M. Posternak, and A. Baldereschi, *Phys. Rev. Lett.* **70**, 1010 (1993).
- [107] P. P. . Ewald, *Ann. d. Phys.* **54**, 519 (1917).

- [108] P. P. . Ewald, *Ann. d. Phys.* **64**, 253 (1921).
- [109] M. Born and K. Huang, *Dynamical Theory of Crystal Lattice* (Oxford University Press, London and New York, p.248, 1954).
- [110] J. C. Phillips, *Rev. Mod. Phys.* **42**, 317 (1970).
- [111] C. W. Chu *et al.*, *Phys. Rev. B* **18**, 2116 (1978).
- [112] G. C. Vezzoli and J. Bera, *Phys. Rev. B* **23**, 3022 (1981).
- [113] T. H. K. Barron, J. A. Birch, and G. K. White, *J. Phys. C* **10**, 1617 (1977).
- [114] R. C. Hanson, K. Helliwell, and C. Schwab, *Phys. Rev. B* **9**, 2649 (1974).
- [115] S. Miyake and S. Hoshino, *Rev. Mod. Phys.* **30**, 172 (1958).
- [116] V. Valdova and J. Jecny, *Phys. Status Solidi A* **45**, 269 (1978).
- [117] M. S. S. Hoshino and J. Harada, *Acta Cryst. A* **30**, 655 (1974).
- [118] J. Schreurs, M. H. Mueller, and L. H. Schwartz, *Acta Cryst. A* **32**, 618 (1976).
- [119] J. B. Boyce and B. A. Huberman, *Phys. Rep.* **51**, 189 (1979).
- [120] J. B. Boyce, T. M. Hayes, , and J. C. M. Jr., *Phys. Rev. B* **23**, 2876 (1981).
- [121] B. Prevot, B. Hennion, and B. Dorner, *J. Phys. C* **10**, 3999 (1977).
- [122] I. P. Kaminow and E. H. Turner, *Phys. Rev. B* **5**, 1564 (1972).
- [123] M. Krauzman *et al.*, *Phys. Rev. Lett.* **33**, 528 (1974).

- [124] J. E. Potts, R. C. Hanson, C. T. Walker, and C. Schwab, *Phys. Rev. B* **9**, 2711 (1974).
- [125] G. Livescu, Z. Vardeny, and Brafman, *Phys. Rev. B* **24**, 1952 (1981).
- [126] B. Hennion, B. Prevot, M. K. R. M. Pick, and B. Dorner, *J. Phys. C* **12**, 1609 (1979).
- [127] Z. Vardeny and O. Brafman, *Phys. Rev. B* **21**, 2585 (1980).
- [128] Z. Vardeny and O. Brafman, *Phys. Rev. B* **19**, 3276 (1979).
- [129] M. Ikezawa, *J. Phys. Soc. Jpn.* **35**, 309 (1973).
- [130] T. Nanba, K. Hachisu, and M. Ikezawa, *J. Phys. Soc. Jpn.* **50**, 1579 (1981).
- [131] M. L. Shand *et al.*, *Phys. Rev. B* **14**, 4637 (1976).
- [132] G. Kanellis, W. Kress, and H. Bilz, *Phys. Rev. Lett.* **56**, 938 (1986).
- [133] G. Kanellis, W. Kress, and H. Bilz, *Phys. Rev. B* **33**, 8733 (1986).
- [134] G. Livescu and O. Brafman, *Phys. Rev. B* **34**, 4255 (1986).
- [135] J. W. Kremer and K. H. Weyrich, *Phys. Rev. B* **40**, 9900 (1989).
- [136] S.-H. Wei, S. B. Zhang, and A. Zunger, *Phys. Rev. Lett.* **70**, 1639 (1993).
- [137] W. E. Pickett, R. E. Cohen, and H. Krakauer, *Phys. Rev. Lett.* **67**, 228 (1991).
- [138] R. E. Cohen, *Nature* **358**, 136 (1992).
- [139] F. D. Murnaghan, *Proc. Natn. Acad. Sci.* **30**, 244 (1944).

- [140] R. W. G. Wyckoff, *Crystal Structures* (Wiley, New York, vol. 1, p.110, 1963).
- [141] A. Feldman and D. Horowitz, *J. Opt. Soc. Am.* **59**, 1406 (1969).
- [142] M. R. Press and D. E. Ellis, *Phys. Rev. B* **38**, 3102 (1988).
- [143] G. Kanellis, W. Kress, and H. Bilz, *Phys. Rev. B* **33**, 8724 (1986).
- [144] C. Patel and W. F. Sherman, *Physica B* **165** and **166**, 923 (1990).
- [145] S. Chatterjee, S. Ghosh, and A. N. Basu, *Phys. Rev. B* **28**, 3534 (1983).
- [146] J. W. Kremer and K. H. Weyrich, *Ferroelectrics* **104**, 403 (1990).
- [147] C. Carabatos *et al.*, *Phys. Rev. Lett.* **26**, 770 (1971).
- [148] R. E. Cohen, W. E. Pickett, and H. Krakauer, *Phys. Rev. Lett.* **62**, 831 (1989).
- [149] R. E. Cohen, W. E. Pickett, and H. Krakauer, *Phys. Rev. Lett.* **64**, 2575 (1990).
- [150] C. O. Rodriguez *et al.*, *Phys. Rev. B* **42**, 2692 (1990).
- [151] J. Liu and Y. K. Vohra, *Phys. Rev. Lett.* **72**, 4105 (1994).
- [152] A. R. Verma and P. Krishna, *Polymorphism and Polytypism in Crystals* (Wiley, New York, 1966).
- [153] G. C. Trigunayat and G. K. Chada, *Phys. Status Solidi A* **4**, 9 (1971).
- [154] C. Kittel, *Introduction to Solid State Physics* (John Wiley & Sons, Inc., sixth edition, p.28, 1976).
- [155] F. C. Frank, *Phil. Mag. A* **56**, 263 (1987).

- [156] D. Pandey, *Phase Transition* **16-17**, 247 (1989).
- [157] P. Pirouz, *Proc. Int. Symp. on Structure and Properties of Dislocations in Semiconductors* (ed S. G. Roberts and R. M. Wilshaw, Bristol: Institute of Physics, 1989).
- [158] B. Winkler, M. T. Dove, E. K. H. Salje, and B. Palosz, *J. Phys. Condens. Matter* **3**, 539 (1991).
- [159] C. Cheng, V. Heine, and R. J. Needs, *Europhys. Lett.* **12**, 69 (1990).
- [160] C. Cheng, V. Heine, and I. L. Jones, *J. Phys. Condens. Matter* **2**, 5907 (1990).
- [161] C. Cheng, V. Heine, and R. J. Needs, *J. Phys. Condens. Matter* **2**, 5115 (1990).
- [162] A. F. Goncharov, E. V. Yokovenko, and S. M. Stishov, *JEPT Lett.* **52**, 491 (1990).
- [163] M. Yoshida *et al.*, *Phys. Rev. B* **48**, 10587 (1993).
- [164] D. W. Feldman, J. H. P. Jr., W. J. Choyke, and L. Patrick, *Phys. Rev.* **173**, 787 (1968).
- [165] C. Lasota, private communication .
- [166] P. Käckell, B. Wenzien, and F. Bechstedt, *Phys. Rev. B* **50**, 10761 (1994).
- [167] P. J. H. Denteneer and W. van Haeringen, *Phys. Rev. B* **33**, 2831 (1986).
- [168] K. J. Chang and M. L. Cohen, *Phys. Rev. B* **35**, 8196 (1987).

- [169] W. R. L. Lambrecht, B. Segall, M. Methfessel, and M. van Schilfgaarde, *Phys. Rev. B* **44**, 3685 (1991).
- [170] ed. by O. Madelung and Landolt-Bornstein, *Physics of Group-IV and III-V Compounds* (Springer-Verlag, vol. 17, part a, Berlin, 1982).
- [171] D. H. Yean and J. R. Riter, *J. Phys. Chem. Solids* **32**, 653 (1971).
- [172] E. Scheiber and N. Soga, *J. Amer. Ceram. Soc.* **49**, 342 (1966).
- [173] R. D. Carnahan, *J. Amer. Ceram. Soc.* **51**, 223 (1968).
- [174] J. V. Aleksandrov, A. F. Goncharov, S. M. Stishov, and E. V. Yokovenko, *JEPT Lett.* **50**, 127 (1989).
- [175] K. Strösser, M. Cardona, and W. J. Choyke, *Solid State Commun.* **63**, 113 (1987).
- [176] B. H. Cheong, K. J. Chang, and M. L. Cohen, *Phys. Rev. B* **44**, 1053 (1991).
- [177] N. E. Christensen, S. Satopathy, and Z. Pawlowska, *Phys. Rev. B* **35**, 1032 (1987).
- [178] M. Ueno, A. Onodera, O. Shimomura, and K. Takemura, *Phys. Rev. B* **45**, 10123 (1992).
- [179] D. Olego, M. Cardona, and P. Vogl, *Phys. Rev. B* **25**, 3878 (1982).
- [180] D. Olego and M. Cardona, *Phys. Rev. B* **25**, 1151 (1982).
- [181] for example see G. P. Srivastava and K. Kunc, *J. Phys. C* **21**, 5087 (1988).

- [182] G. P. Srivastava, *The Physics of Phonons* (Adam Hilger, Bristol, Philadelphia and New York, 1990).
- [183] W. Cochran, *The Dynamics of Atoms in Crystal* (Crane, Russak& Company, Inc., New York, New York, 1973).
- [184] D. H. Lee and J. D. Joannopoulos, *Phys. Rev. Lett.* **48**, 1846 (1982).
- [185] C. Patel *et al.*, *J. Phys. Condens. Matter* **4**, 753 (1992).
- [186] M. Hofmann, A. Zywietz, K. Karch, and F. Bechstedt, *Phys. Rev. B* **50**, 13401 (1994).
- [187] W. Windl *et al.*, *Phys. Rev. B* **49**, 8764 (1994).
- [188] F. Birch, *J. Geophys. Res.* **83**, 1257 (1978).
- [189] A. R. Goni, K. Sysssen, and M. Cardona, *Phys. Rev. B* **41**, 10104 (1990).
- [190] R. Vetter, *Phys. Status Solidi A* **8**, 443 (1971).
- [191] D. K. Biegelsen, *Phys. Rev. Lett.* **32**, 1196 (1974).
- [192] D. K. Biegelsen, *Phys. Rev. B* **12**, 2427 (1975).
- [193] M. Cardona, W. Paul, and H. Brooks, *J. Phys. Chem. Solids* **8**, 204 (1959).
- [194] Z. Levine and D. C. Allan, *Phys. Rev. B* **43**, 4187 (1991).
- [195] D. F. Gibbs and G. J. Hill, *Phil. Mag.* **9**, 367 (1964).
- [196] J. A. V. Vechten, *Phys. Rev.* **182**, 891 (1969).

- [197] M. E. Lines and A. M. Glass, *Principles and Applications of ferroelectrics and Related Materials* (Alrendom, Oxford, 1977).
- [198] M. D. Fontana, G. Metrat, J. L. Servoin, and F. Gervais, *J. Phys. C* **16**, 483 (1984).
- [199] R. Comes, M. Lambert, and A. Guinier, *Solid St. Commun.* **6**, 715 (1968).
- [200] T. P. Dougherty *et al.*, *Science* **258**, 770 (1992).
- [201] A. C. Nunes, J. D. Axe, and G. Shirane, *Ferroelectrics* **2**, 291 (1971).
- [202] G. A. Samara, *Ferroelectrics* **73**, 145 (1987).
- [203] R. Cohen and H. Krakauer, *Phys. Rev. B* **42**, 6416 (1990).
- [204] D. J. Singh and L. L. Boyer, *Ferroelectrics* **136**, 95 (1992).
- [205] R. D. King-Smith and D. Vanderbilt, *Ferroelectrics* **136**, 85 (1992).
- [206] A. V. Postnikov and M. M. T. Neumann G. Borstel, *Phys. Rev. B* **48**, 5910 (1993).
- [207] A. V. Postnikov, T. neumann, and G. Borstel, *Phys. Rev. B* **50**, 758 (1994).
- [208] A. V. Postnikov and G. Borstel, *Phys. Rev. B* **50**, 16403 (1994).
- [209] R. D. King-Smith and D. Vanderbilt, *Phys. Rev. B* **49**, 5828 (1994).
- [210] W. Zhong, D. Vanderbilt, and K. Rabe, *Phys. Rev. Lett* **73**, 1861 (1994).
- [211] W. Zhong, D. Vanderbilt, and K. Rabe, preprint (1995).

- [212] H. D. Chen, private communication .
- [213] D. J. Singh, Phys. Rev. B **44**, 7451 (1992).
- [214] A. W. Hewat, J. Phys. C **6**, 2559 (1973).
- [215] W. Zhong, R. D. King-Smith, and D. Vanderbilt, Phys. Rev. Lett. **72**, 3618 (1994).
- [216] P. Ghosez, X. Gonze, P. Lambin, and J.-P. Michenaud, Phys. Rev. B **51**, 6765 (1995).
- [217] M. Posternak, R. Resta, and A. Baldereschi, Phys. Rev. B **50**, 8911 (1994).
- [218] M. D. Fontana, G. E. Kugel, and C. Carabatos, J. Physique **42**, C6 (1981).
- [219] J. F. Cornwell, *Group Theory in Physics* (Academic Press, Inc., London, p.338, 1984).
- [220] G. E. Kugel, M. D. Fontana, J. Vamvakas, and C. Carabatos, *Raman Spectroscopy, Linear and Non-Linear* (ed. J. Lascombe and P. V. Huong, Wiley-Heyden, New York, p.457, 1982).

Vita

Cheng-Zhang Wang

Born in Li County of Hunan Province, China, on April 17, 1966. Earned a B.S. degree in Physics in July of 1988 from Beijing University (Peking University). Then continued graduate studies there and received a M.A. degree in July of 1991. Subsequently received a M.S. degree in June of 1993 and completed requirements for Ph.D. in physics at the College of William and Mary in Virginia, June of 1995. He started working as a post-doctoral research associate with Professor Henry Krakauer at the College of William and Mary in June of 1995.